

A LIQUEFIED GAS THRUSTER FOR A MICRO SATELLITE

by

Adriaan Jacobus Joubert

Thesis presented in partial fulfilment of the requirements for the degree
Master of Science in Engineering at the University of Stellenbosch

Promoter: R T Dobson



March 2007

Department of Mechanical and Mechatronic Engineering
University of Stellenbosch

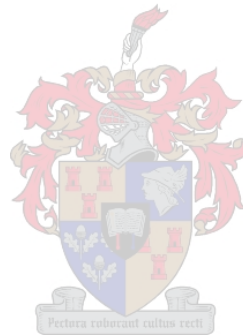
Declaration

I, Adriaan Jacobus Joubert, the undersigned, hereby declare that the work contained in this thesis is my own original work and has not previously, in its entirety or in part, been submitted at any university for a degree.

.....

Signature of candidate

..... day of February 2007



Acknowledgements

The following people are thanked for their contributions toward this project, without which the completion of this project would not have been possible:

Robert Dobson – promoter

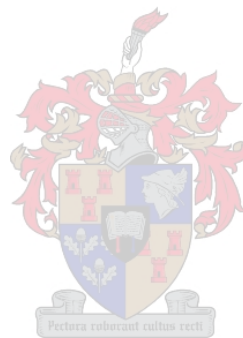
For always having an open door and being available. Always being helpful and not minding sitting around for hours to work things through.

Cobus Zietsman – laboratory technician

For all your help and practical assistance with the experimental set-up.

Ferdie Zietsman – laboratory technician

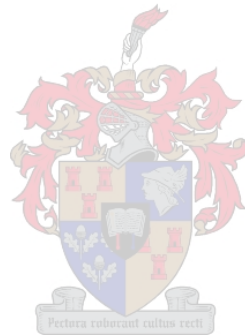
For helping me with those nozzles, even at the most inconvenient of times.



Dedication

All glory to God for His endless supply of love and grace.

This thesis is also dedicated to my parents, for their support and love. Without them I would not have had these opportunities.



Summary

The focus of this project was to investigate the working of a liquefied gas micro satellite thruster. An introduction is given in which the significance of the project in relation to the literature is stated. The objectives of the project are also stated. In the literature survey the historical development and design specifications of some relevant thruster systems is discussed. An experimental model was designed and built to test the working of a thruster system. Attention is also given to the measurement and calibration techniques used to obtain experimental data. A computer program was written to simulate the thruster system.

The experimental set-up was designed so that an accumulator could be charged with liquid butane from a storage tank. The accumulator was charged with 13 ml of liquid butane, which was heated and then exhausted through a nozzle. Copper mesh was placed in the accumulator to improve the heat transfer to the butane vapour before it was exhausted through the nozzle. A cantilever beam was used to measure the thrust of the system. The system was tested under atmospheric conditions of 100 000 Pa as well as under vacuum conditions of 20 Pa. Two nozzles were also tested: nozzle-1 with a throat diameter of 1 mm and an exit diameter of 5 mm and nozzle-2 with a throat diameter of 1 mm and an exit diameter of 1.6 mm.

A computer program was written to simulate the flow of the butane vapour through the nozzle, as well as the complex two-phase behaviour of the butane in the accumulator. Traditional gas dynamic theory was used to model the flow through the nozzle. The transient behaviour of the system was modelled to predict the rate of liquid to vapour mass transfer in the accumulator. Additionally, the computer program was developed to simulate the system with copper mesh placed in the accumulator.

From the experimental results it was shown that the addition of copper mesh in the accumulator improved the total thrust achieved with a 13 ml charge of liquid butane by more than 50 %. Under atmospheric conditions shockwaves were present in both of the two nozzles tested. Nozzle-2 showed an increase of 91 % in the total thrust achieved over a 5 second burst compared to the total thrust achieved using nozzle-1.

With no copper mesh in the accumulator and using nozzle-1 a peak thrust of 39 mN was achieved under atmospheric conditions while under vacuum conditions a peak thrust of 495 mN was achieved. This resulted in a total thrust of 0.365 Ns under atmospheric conditions and 4.88 Ns under vacuum conditions with a 13 ml charge of liquid butane. Using the total thrust achieved the specific impulse of the system was calculated as 5 seconds under atmospheric conditions and 67.5 seconds under vacuum conditions with no mesh in the accumulator and using nozzle-1.

The theoretical model compared well with the experimental results except when nozzle-1 was modelled under atmospheric conditions. Under vacuum conditions the results obtained from the theoretical model compared well with the experimental results using both of the nozzles. In the modelling of the mesh in the accumulator an overall heat transfer factor was incorporated into the model to take into account the uncertainty of the heat transfer area as well as the overall heat transfer coefficient.

The theoretical model and experimental test results are discussed and thereafter conclusions are also drawn. There are also recommendations made for future work that could be done in the further development of a liquefied gas micro satellite thruster system. It is recommended that a “resistojet” type thruster should be tested at the University of Stellenbosch and that further testing be done with mesh in the accumulator to find the optimum amount of mesh that should be placed in the accumulator.

Opsomming

Die fokus van hierdie projek was om die werking van 'n vervloeiëdegas stuwervir 'n mikro satelliet te ondersoek. In die inleiding word die belangrikheid van hierdie projek met betrekking tot die literatuur gestel. Die mikpunte van die projek word ook genoem. In die literatuur oorsig word die onlangse ontwikkeling en ontwerp-spesifikasies van sommige relevante stuwervstelsels bespreek. 'n Eksperimentele model was ontwerp en gebou om die werking van 'n stuwervstelsel te toets. Aandag word ook gegee aan die metings- en kalibrasietegnieke wat gebruik is om die eksperimentele data te verkry. 'n Rekenaarprogram is ook geskryf om die stuwervstelsel te simuleer.

Die eksperimentele opstelling was so ontwerp dat 'n akkumulator gevul kan word met butaan vloeistof vanaf die opgaartenk. Die akkumulator was gevul met 13 ml butaan vloeistof wat eers verhit is voordat dit deur die mondstuk uitgelaat is. Koper maasdraad is in die akkumulator geplaas om die hitte oordrag na die butaan gas te verbeter voordat dit deur die mondstuk uitgelaat is. 'n Kantel balk was gebruik om die stukrag van die stelsel te meet. Die stelsel is onder atmosferiese toestande van 100 000 Pa sowel as onder vakuüm toestande van 20 Pa getoets. Daar was ook twee mondstukke getoets: mondstuk-1 met 'n 1 mm diameter monding en 'n 5 mm uitlaat diameter en mondstuk-2 met 'n 1 mm diameter monding en 'n 1.6 mm uitlaat diameter.

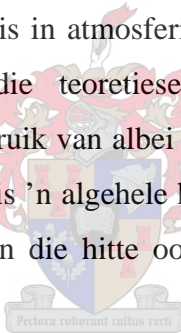
'n Rekenaarprogram is geskryf om die vloeivon die butaan gas deur die mondstuk sowel as die komplekse twee-fase gedrag van die butaan in die akkumulator te simuleer. Tradisionele gas dinamika is gebruik om die vloeideur die mondstuk te modelleer. Die oorgangstoestand van die stelsel is gemodelleer om die tempo van vloeistof na gas massa oordrag in die akkumulator te voorspel. Die rekenaarprogram is ook ontwikkel om die maasdraad in die akkumulator te simuleer.

Die eksperimentele resultate het getoon dat die toevoeging van koper maasdraad tot die akkumulator die totale stukrag verkry uit 13 ml butaan vloeistof met meer as 50 % verbeter het. In atmosferiese toestande was daar skokgolwe teenwoordig in beide van

die mondstukke wat getoets is. Mondstuk-2 het 'n verbetering van 91 % in die totale stukrag behaal oor 'n 5 sekonde ontluiking in vergelyking met die totale stukrag behaal met die gebruik van mondstuk-1.

Met geen maasdraad in die akkumulator nie en met die gebruik van mondstuk-1 is 'n piek stukrag van 39 mN bereik in atmosferiese toestande terwyl 'n piek stukrag van 495 mN bereik is onder vakuüm toestande. Dit het daarop neergekom dat 'n totale stukrag van 0.365 Ns in atmosferiese toestande en 4.88 Ns in vakuüm toestande bereik is met 13 ml butaan vloeistof met die gebruik van mondstuk-1. Met die gebruik van die totale stukrag is die I_{sp} van die stelsel bereken as 5 sekondes in atmosferiese toestande en 67.3 sekondes onder vakuüm toestande met geen maasdraad in die akkumulator en met die gebruik van mondstuk-1.

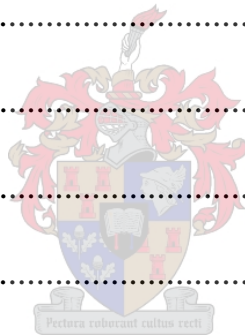
Die teoretiese model het goed vergelyk met die eksperimentele resultate behalwe wanneer mondstuk-1 gemodelleer is in atmosferiese toestande. In vakuüm toestande het die resultate behaal met die teoretiese model goed vergelyk met die eksperimentele resultate met die gebruik van albei mondstukke. In die modellering van die maasdraad in die akkumulator is 'n algehele hitte oordrag faktor geïnkorporeer in die model om die onsekerheid van die hitte oordrag area asook die algehele hitte oordragkoëffisiënt in ag te neem.



Die teoretiese model en eksperimentele toets resultate word bespreek en gevolgtrekkings word gemaak vanuit die bespreking. Daar is ook voorstelle gemaak vir toekomstige werk wat gedoen kan word in die toekomstige ontwikkeling van 'n vervloeidegas mikro satelliet stuerer sisteem. Dit word ook voorgestel dat 'n "resistojet" tipe stuerer getoets word by die Universiteit van Stellenbosch en dat verdere toetse gedoen word met maasdraad in die akkumulator.

Contents

Declaration	i
Summary	ii
Opsomming	iv
Acknowledgements	vi
Dedication	vii
Contents	viii
List of Figures	xii
List of Tables	xiv
Nomenclature	xv
1 Introduction.....	1-1
2 Objectives	2-1
3 Literature Survey	3-1
3.1 Historical Development	3-1
3.1.1 Historical development at University of Surrey	3-1
3.1.2 Historical development at University of Stellenbosch.....	3-4
3.2 Thrust Measurements.....	3-6
3.3 Design Specifications.....	3-6
4 Design Criteria of Experimental Set-up	4-1
4.1 Nozzle	4-1



4.2 Liquefied Gas Container (Storage Tank).....	4-2
4.3 Filling Tube.....	4-2
4.4 Accumulator.....	4-2
4.5 Heating.....	4-4
4.6 Sloshing.....	4-5
5 Experimental Set-up	5-1
5.1 Measurement and Control.....	5-1
5.1.1 Control of solenoid valves	5-1
5.1.2 Temperature measurement.....	5-2
5.1.3 Filtering of temperature data.....	5-3
5.1.4 Pressure measurement.....	5-4
5.1.5 Thrust measurement.....	5-5
5.2 Calibration.....	5-9
5.2.1 Pressure sensor calibration.....	5-9
5.2.2 Thrust sensor calibration.....	5-11
5.3 Charging Procedure	5-12
5.4 Vacuum Chamber Tests.....	5-13
6 Thermo-fluid Modelling of the System	6-1
6.1 Idealized Gas Dynamics	6-1
6.2 Calculation Procedure Logic Flow Diagram	6-12
6.3 Two-phase System Model.....	6-14
6.3.1 Initial conditions	6-16
6.3.2 Vapour control volume	6-16

6.3.3 Liquid control volume.....	6-18
6.3.4 Mesh in accumulator.....	6-20
6.4 Logic of Mathematical Model for Thruster System	6-22
7 Results.....	7-1
7.1 Experimental Results	7-1
7.1.1 Tests conducted at 25 °C	7-1
7.1.2 Different nozzle tests	7-6
7.1.3 Vacuum chamber testing.....	7-8
7.2 Theoretical Results.....	7-10
7.2.1 Atmospheric condition.....	7-11
7.2.2 Vacuum conditions	7-15
7.2.3 Placing of copper mesh in accumulator	7-17
7.2.4 Liquid surface area.....	7-19
7.2.5 Estimation of I_{sp} with mesh in accumulator.....	7-20
8 Discussion and Conclusion.....	8-1
8.1 Validity of Experimental Results	8-1
8.2 Validity of Theoretical Model	8-2
8.3 Mesh Inside Accumulator	8-3
8.4 Nozzle Size	8-4
8.5 Overall Performance of Thruster System	8-5
9 Recommendations.....	9-1
9.1 Resistojet	9-1
9.2 Use of Mesh in Accumulator	9-1

9.3 Dynamic Testing	9-1
9.4 Space Proven Components	9-2
9.5 Development of Accumulator Type Thruster	9-2
10 References.....	10-1
Appendix A: Correlation for Saturation Properties of Butane	A-1
Appendix B: Validity of Thrust Modelling	B-1
Appendix C: Theoretical Thrust Calculation.....	C-1
Appendix D: Photographs of Experimental Set-up.....	D-1



List of Tables

Table 5.3 Measured values from thermocouples and platinum resistor	5-2
Table 7.1 Method-1 of exhausting 13 ml initial charge.....	7-4
Table 7.2 Method 2 of exhausting 13 ml initial charge	7-5
Table 7.3 Method-3 of exhausting 13 ml initial charge.....	7-6
Table 7.4 Method-4 of exhausting 13 ml initial charge.....	7-6
Table 7.5 Thrust achieved at vacuum compared to atmospheric for the two different nozzles with no mesh in the accumulator	7-9
Table 7.6 Comparison between theoretical thrust and experimental for nozzle-1	7-16
Table 7.7 Comparison between theoretical thrust and experimental for nozzle-2	7-16
Table 7.8 Estimated I_{sp} values under vacuum conditions using nozzle-1.....	7-21
Table 7.9 Experimental and theoretical values for I_{sp} under vacuum conditions with different number of mesh discs in accumulator.....	7-21
Table A.1 Constants required for determining enthalpy.....	A-1
Table A.2 Constants required for determining specific heat	A-2
Table A.3 Constants required for determining saturation pressure	A-3
Table B.1 Results from Example 17.7	B-1
Table B.2 Results from Example 17.8	B-2
Table C.1 Comparison between analytical and experimental strain.....	C-2

List of Figures

Figure 3.1 Cutaway of the Mark-III resistojet	3-2
Figure 3.2 Cutaway of a “Resistojet”	3-4
Figure 3.3 Schematic of Weyer’s (2004) propulsion system.....	3-5
Figure 4.1 Schematic diagram of the experimental set-up	4-1
Figure 4.2 Schematic of accumulator	4-3
Figure 5.1 Diagram of valve control system.....	5-1
Figure 5.2 Steam temperature versus time.....	5-2
Figure 5.3 Ice water temperature versus time	5-3
Figure 5.4(a) Temperature data – unfiltered	5-4
Figure 5.4(b) Temperature data – filtered.....	5-4
Figure 5.5 Method of measuring thrust using a cantilevered beam.....	5-5
Figure 5.6 Strain gauge configuration to measure thrust.....	5-8
Figure 5.7 Pressure sensor calibration for inlet end pressure transducer.....	5-10
Figure 5.8 Pressure sensor calibration for outlet end pressure transducer.....	5-10
Figure 5.9 Thrust sensor calibration	5-11
Figure 5.10 Schematic diagram of filling set-up	5-12
Figure 6.1 Nozzle control volume	6-2
Figure 6.2 Determining position of shockwave	6-9
Figure 6.3 Calculation logic flow diagram of gas dynamics model	6-13
Figure 6.4 Diagram of accumulator - two-phase model	6-15
Figure 6.5 Diagram of vapour control volume	6-16
Figure 6.6 Diagram of liquid control volume	6-19
Figure 6.7 Diagram of accumulator with mesh	6-20
Figure 7.1 Pressure for method 1 of exhausting 13 ml initial charge with 20 mesh discs in accumulator.....	7-2
Figure 7.2 Thrust for method 1 of exhausting 13 ml initial charge with 20 mesh discs in accumulator.....	7-3
Figure 7.3 Pressure curve for method 2 of exhausting 13 ml initial charge with 0 mesh discs in accumulator.....	7-4
Figure 7.4 First thrust curve for method 2 of exhausting 13 ml initial charge with 0 mesh discs in accumulator	7-5

Figure 7.5 Pressure curves for the two nozzles at atmospheric conditions	7-7
Figure 7.6 Thrust curves for the two nozzles at atmospheric conditions.....	7-7
Figure 7.7 Comparison between vacuum chamber and atmospheric conditions tests	7-8
Figure 7.8 Comparison between vacuum chamber and atmospheric conditions tests	7-9
Figure 7.9 Comparison between experimental and theoretical pressure results (nozzle-1 and backpressure = 100 kPa)	7-11
Figure 7.10 Comparison between experimental and theoretical thrust results (nozzle-1 and backpressure = 100 kPa)	7-11
Figure 7.11 Comparison between experimental and theoretical pressure results (nozzle-2 and backpressure = 100 kPa)	7-13
Figure 7.12 Comparison between experimental and theoretical thrust achieved (nozzle-2 and backpressure = 100 kPa)	7-14
Figure 7.13 Comparison between experimental and theoretical pressure results (backpressure = 20 Pa).....	7-15
Figure 7.14 Comparison between experimental and theoretical thrust achieved (backpressure = 20 Pa).....	7-15
Figure 7.15 Theoretical pressure against time for different heat transfer correlation coefficients, b for different number of mesh discs	7-18
Figure 7.16 Pressure against time for different liquid-vapour contact areas	7-20
Figure 7.17 Comparison between experimental and theoretical I_{sp} under vacuum conditions with different number of mesh discs in the accumulator	7-21
Figure 8.1 Total thrust achieved against number of mesh discs for more-or-less the same initial conditions	8-4
Figure C.1 Sensor curve.....	C-2
Figure D.1 Experimental set-up.....	D-1
Figure D.2 Experimental set-up in vacuum chamber	D-1
Figure D.3 Accumulator	D-2
Figure D.4 Flange of accumulator	D-2

Nomenclature

Roman Symbols

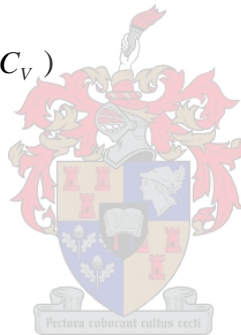
A	Area [m^2]
a	Speed of sound [m/s]
b	Width [m]
b	Heat transfer correlation coefficient
C_p	Constant pressure specific heat [$\text{J/kg} \cdot \text{K}$]
C_v	Constant volume specific heat [$\text{J/kg} \cdot \text{K}$]
E	Young's modulus of elasticity [N/m^2]
F	Force [N]
g	Gravitational acceleration, 9.81 [m/s^2]
h	Thickness [m]
I	Impulse [$\text{N} \cdot \text{s}$]
I	Cross-sectional moment of inertia [m^4]
K	Strain gauge factor
K	Intercept
k	Thermal conductivity [$\text{W/m} \cdot \text{K}$]
L	Length [m]
M	Mach number
M	Bending moment [$\text{N} \cdot \text{m}$]
m	Mass [kg]
\dot{m}	Mass flow rate [kg/s]
N	Number
n	Slope
p	Pressure [Pa]
\dot{Q}	Heat transfer rate [W]
R	Gas constant [$\text{J/kg} \cdot \text{K}$]
R	Electrical resistance [Ω]
T	Temperature [$^{\circ}\text{C}$] or [K]
t	Time [s]



V	Velocity [m/s]
V	Voltage [V]
U	Heat transfer coefficient [$\text{W}/\text{m}^2 \cdot \text{K}$]
x	Cartesian coordinate
y	Cartesian coordinate
z	Cartesian coordinate

Greek Symbols

Δ	Difference
ε	Strain
σ	Stress [N/m^2]
σ	Condensation coefficient
ρ	Density [kg/m^3]
γ	Specific heat ratio ($=C_p/C_v$)



Superscripts

*	Critical
---	----------

Subscripts

a	Ambient
B	Back
c	Copper
d	Mesh discs
e	Exit
ef	Effective
$evap$	Evaporation
f	Final
g	Gas
h	Hole
i	Initial

<i>l</i>	Liquid
<i>lv</i>	Liquid-vapour
<i>m</i>	Mesh
<i>mv</i>	Mesh-vapour
<i>norm</i>	Normal
<i>o</i>	Stagnation
<i>p</i>	Propellant
<i>s</i>	Surface
<i>sat</i>	Saturation
<i>sp</i>	Specific
<i>sp_o</i>	Specific base case
<i>sub</i>	Subsonic
<i>sup</i>	Supersonic
<i>T</i>	Temperature
<i>T</i>	Thrust
<i>t</i>	Throat
<i>v</i>	Vapour
<i>w</i>	Wall
<i>w</i>	Wire
<i>wl</i>	Wall-liquid
<i>wv</i>	Wall-vapour
<i>x</i>	Axial



1 Introduction

Since 1999 there has been a significant increase in the demand for precise positioning and manoeuvring of small satellites. This is driven mostly by small satellite constellations, which require propulsion for launcher injection error, drag compensation, constellation phasing and proximity manoeuvring and rendezvous (Gibbon et al., 2002). Space propulsion that has formally been exclusive to large costly missions, is now becoming a reality for more and more small satellites. Considerable on-orbit experience has been obtained with cold gases, liquefied gases and low power electrothermal devices. As more reliable, accurate systems can be developed at low cost, small satellite propulsion is becoming more feasible (Barker et al., 2005).

Traditionally cold gas nitrogen systems have been used as propulsion systems for small spacecraft. The main disadvantage of using a nitrogen system is that it has a relatively low storage density, even at high pressures. This requires a large storage tank and small spacecraft are often more volume constrained than mass limited. Recently liquefied gas systems have been looked at as an alternative to cold gas systems where the propellant is stored in liquids. Because liquefied gases are stored as liquids, they have a higher storage density, a smaller tankage volume, and are stored at very low pressures that require no regulation system (Gibbon et al., 2002).

This project is a continuation of a project by Weyer (2004) where he used an accumulator type propulsion system. An accumulator system would also be used in this project. One of the objectives of this project was to improve the heat transfer to the butane vapour in the accumulator. Another objective was to be able to measure the exact amount of liquid butane charge fed into the accumulator.

To improve the heat transfer to the butane vapour in the accumulator copper mesh was placed in the accumulator. A heat transfer correlation coefficient that takes into account the uncertainty of the heat transfer area, as well as the heat transfer coefficient of the mesh was determined by comparing the mathematical model to the experimental results.

2 Objectives

The objectives of this project were to simulate the performance of a micro satellite liquefied gas thruster system. In order to achieve this, a thruster system and test set-up were designed and built. These experimental results could then be compared to the results from the mathematical model developed and thereby the model could be validated.

After the thruster system was built, it had to be able to perform given functions. For instance the effect of different quantities of mesh in the accumulator had to be tested. Also, certain properties of the fluid needed to be measured accurately. The pressure and temperature had to be measured accurately, as well as the amount of butane liquid that was put into the accumulator before each test. The thrust that the system was able to achieve also needed to be measured accurately.

The purpose of the mathematical model of the system was to be able to predict the thrust that can be achieved by the thruster system. This meant that the properties of the fluid on the inside of the accumulator had to be predicted accurately. The thrust that the system will be able to achieve can be calculated using the properties of the fluid in the accumulator. The theoretical model will be validated by comparing the experimental results to the results predicted by the analytical model of the system.

With the now validated mathematical model of the thruster system, a thruster system can be designed by making use of the mathematical model. This would mean that a lot of time and money could be saved in the development and testing of a micro satellite thruster system using the validated mathematical model.

3 Literature Survey

Since 1999 there has been a significant increase in the demand for precise positioning and manoeuvring of small satellites. This demand is driven mostly by small satellite constellations, which require propulsion for launcher injection error, drag compensation, constellation phasing and proximity manoeuvring and rendezvous (Gibbon et al., 2002).

The objective of this literature survey is to summarise the work done on small satellite thrusters, also termed secondary propulsion systems, which use liquefied gas as a propellant. The historical development, thrust measurement systems as well as some of the design specifications of these thrusters will be discussed.

3.1 Historical Development

Most of the literature available on secondary propulsion systems making use of liquefied gas as propellant appears to have been done at the University of Surrey. In the overview of the historical development of these thruster systems, the work done at University of Surrey and the University of Stellenbosch will be presented.

3.1.1 Historical development at University of Surrey

A low power thruster concept was developed and tested by Sweeting et al. (1999). The Mark-I thruster demonstrated that it was feasible for small satellite applications. The Mark-I was not considered flight worthy, due to the fact that it took 30 min to reach a steady state. It was only able to achieve an I_{sp} of 48 seconds at sea level and the heating element only had a lifetime on the order of 1-2 hours at power levels of 200-560 Watts.

After the Mark-I thruster the Mark-II thruster was designed in order to improve on the problems encountered with Mark-I; the heater lifetime was increased to 150 hours and the efficiency was improved by a factor two. With a nozzle throat size of 0.12 mm friction losses start to play a significant roll. This meant that no matter how much power was put into the gas, the resulting increase in temperature was absorbed by friction losses in the throat of the nozzle. The heat transfer efficiency only reached 12 per cent with an

I_{sp} of 84 seconds. So they decided to design a bigger system, the Mark-III proto flight resistojet.

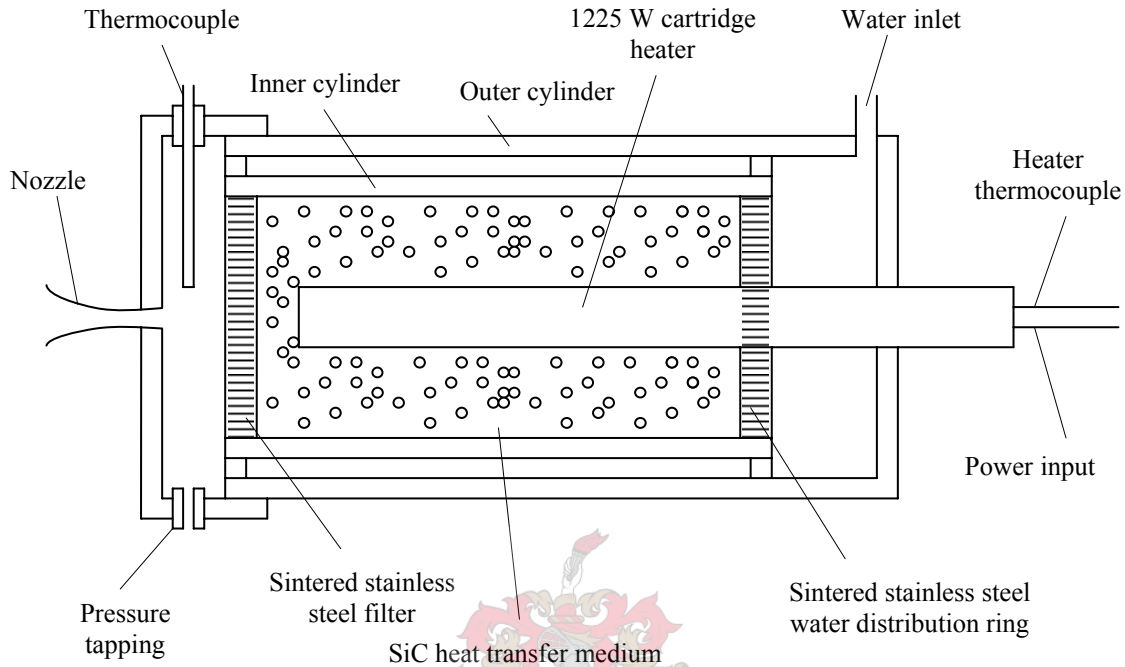


Figure 3.1 Cutaway of the Mark-III resistojet

In the Mark-III resistojet, shown in Figure 3.1, the water is fed through the water inlet under a high pressure. The sintered stainless steel water distribution ring then evenly distributes this water. Silicon carbide balls of 500 μm are packed around the heater. The water then passes through the silicon carbide heat transfer medium. Again it is evenly distributed, just before the nozzle exit, by a sintered stainless steel filter.

The idea is to heat the SiC heat transfer medium before the water is released into it. The water is then vaporized inside the chamber and exhausted through the nozzle as a gas.

On the 28th of June 2000 Surrey Satellite Technology Ltd (SSTL) launched its first nano satellite SNAP-1 (Gibbon et al., 2002). This 6.5 kg spacecraft was equipped with a small cold gas propulsion system utilising 32.6 grams of butane propellant. During the

propulsion system operation the system was able to raise the spacecraft's orbit by nearly 4 kilometres.

In the SNAP-1 propulsion system one of the most obvious features is that there is no storage tank. Instead the propellant is stored in the 1.1 metres of titanium tubing. A fill valve is welded directly to the one end of the tube assembly. The other end is connected to a titanium manifold. The manifold contains a pressure transducer and temperature sensor for system monitoring. Additionally, inside the manifold there are stainless steel mesh discs, which act both as filters and as heat transfer elements. The manifold has an external heater, which ensures propellant vaporisation during firings. Finally an isolation valve and a thruster valve are fitted inside the manifold.

In the first sequence of firings the propulsion system was able to raise SNAP-1's orbit between 3.1 and 3.4 km. In the second firing sequence the orbit was raised by 540 m. In both instances drag effects were taken into account and the distance given was the distance where it would have been had the propulsion system not been used. From these values they were able to calculate the total effective ΔV . The effective ΔV was between 1.9 and 2.1 m/s, giving a mission I_{sp} of approximately 43 s. This was lower than their theoretical value of 70 s. Given that 32.6 g of propellant was used in 297 s of firing, the effective firing is calculated as 46 mN. Again this was lower than predicted, given a firing temperature of more than 20 °C. One reason given in the article for the performance of the thruster, is that some 30-40 % of the propellant was expelled in liquid form.

A number of different propulsion concepts are discussed for advanced low cost propulsion in small satellites beyond "low earth orbit" (Barker et al., 2005). One of these concepts is the "resistojet" concept. The "resistojet" consists of a brazed stainless steel tube and expansion nozzle containing two Nichrome electrical resistance wire heaters spirally wound on a ceramic bobbin. It is designed for both liquid propellants such as butane, and gaseous propellants such as xenon or nitrogen.

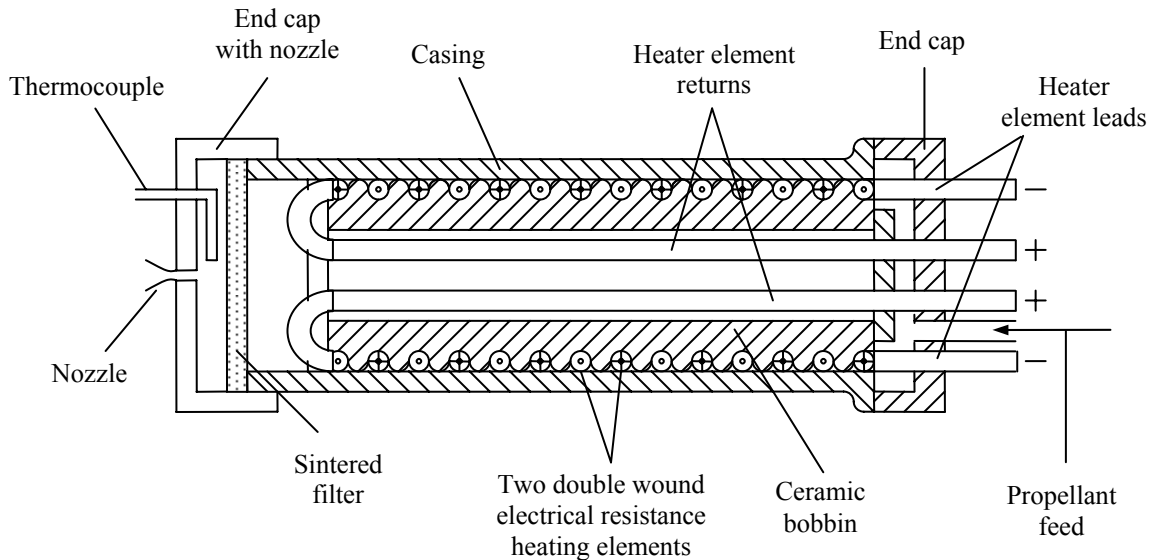
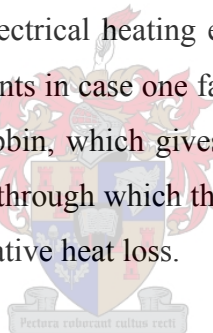


Figure 3.2 Cutaway of a “Resistojet”

The propellant is forced over the electrical heating elements wound spirally around the bobbin. There are two heating elements in case one fails. The propellant is forced to flow in a spiral flow path around the bobbin, which gives a longer contact time for the heat transfer to take place. The chamber, through which the propellant is forced, is surrounded by a heat shield to minimise the radiative heat loss.



The low power resistojets are however limited by a low I_{sp} (~50 s for xenon and ~100 s for nitrogen and butane). The reaction time of the system is also slow, with a 10 min warm-up period required.

3.1.2 Historical development at University of Stellenbosch

Weyer (2004) developed the first thruster at the University of Stellenbosch. It was constructed from Perspex to make it possible to observe the propellant behaviour inside the tank and tubing. The propellant used was butane used which was the same as butane used for refilling cigarette lighters. This butane was a mixture of normal butane, iso-butane and propane. The mixture ratio given by the manufacturer was 54 % normal butane, 24 % iso-butane and 22 % propane. The thruster system had a storage tank, which was filled with liquid butane. The liquid butane was then fed via a solenoid valve into an

accumulator – usually until the pressure in the accumulator and storage tank equalised. The model was fitted with two sources of electrical heating energy. One heating element was placed inside the storage tank and the other around a part of the accumulator.

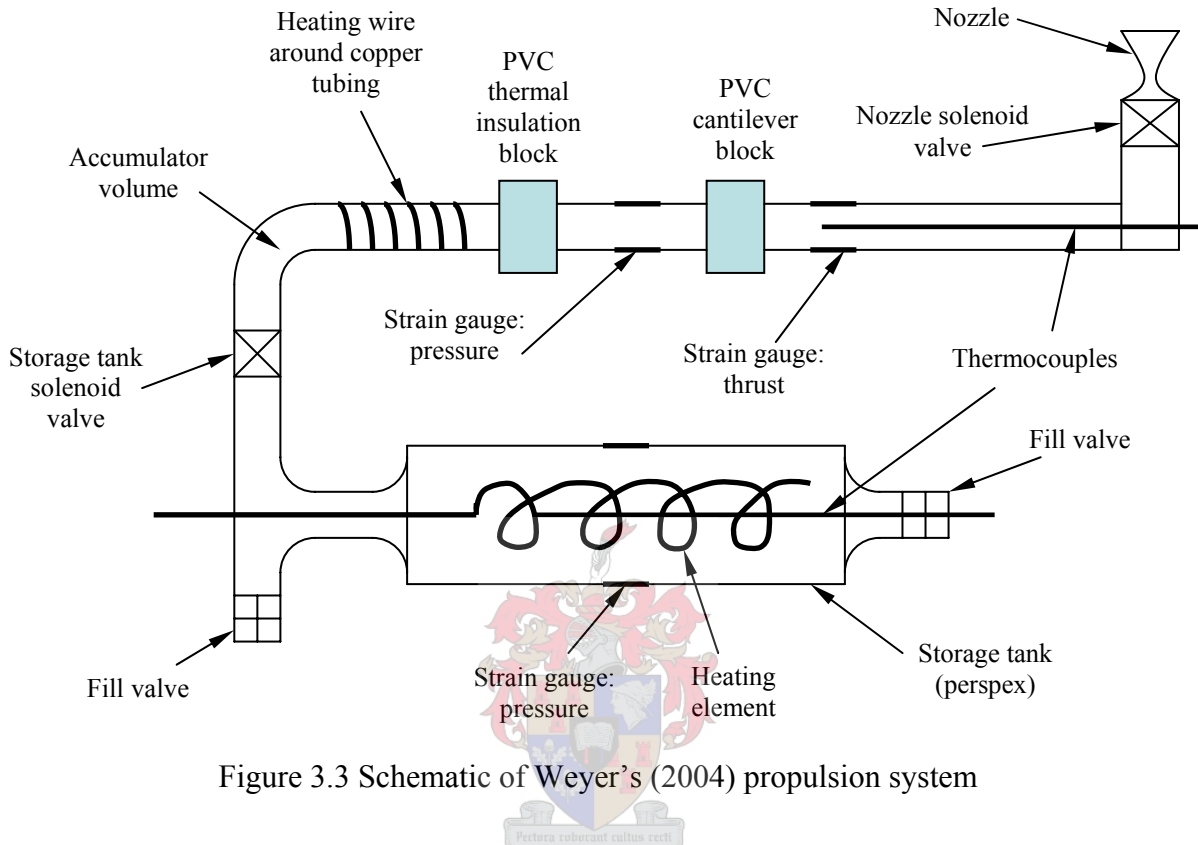


Figure 3.3 Schematic of Weyer's (2004) propulsion system

The butane was then heated inside the accumulator and the boiling propellant resulted in an increase in temperature and pressure, which was monitored. Superheating of the vapour also occurred depending on the amount of heat input and the vapour pressure. Once a satisfactory pressure had been reached the second (nozzle) solenoid valve was opened, allowing the propellant to flow out of the nozzle, creating the thrust.

The I_{sp} of the system was given as 36 s. Typical results for the butane firings from a pressure of 200 to 300 kPa into a back pressure of 100 kPa showed a peak thrust of about 50 mN, dropping of to about 30 mN over a period of about two seconds. The operating temperatures are not clear from the article, but from certain figures in the article it is estimated that the operating temperatures were between 10 and 15 °C for the accumulator and between 0 and 6 °C for the storage tank.

3.2 Thrust Measurements

Xiong et al. (2002) discusses a colloid micro thruster system that is able to produce controllable thrust levels in the order of μN . The colloid micro thruster system is not relevant to this project, as this project focuses on a liquefied gas thruster system, however the thrust measurement system that was used to measure the thrust produced is discussed in the article. In the experiment, a cantilever beam is used as a sensing element. The free end of the cantilever beam is then aligned with the thruster. The cantilever beam transforms thrust signals into vibration signals, which can be measured by a laser vibrometer (Polytech clv-1000). From the vibration amplitude the thrust can be obtained.

Ye et al. (2001) discusses a vaporizing water micro thruster. A method of determining the thrust similar to Xiong et al. was used. Again a cantilever beam is aligned to the thruster. A Doppler vibrometer is used to determine the displacement at the free end of the cantilever beam. The measured Doppler displacement can then be used to calculate the thrust.

Behkam et al. (2004) looks at a propulsion system for swimming *microrobots*. The authors propose a propulsion system inspired by motility mechanism of bacteria with peritrichous flagellation. The detail of the propulsion system will not be discussed here, however, the thrust measurement system is very similar to the one used in this thesis. The thrust force is also applied at the free end of a cantilever beam, as is the case in the previous two articles. The difference being that in this project the thrust is measured directly using strain gauges. The force sensor circuit is composed of a Wheatstone bridge circuit and a differential amplifier. A CA-1000 National Instruments Data Acquisition Board (DAQ) reads the voltage output of the amplifying circuit into a MATLAB program. The voltage can then be directly converted to a thrust force.

3.3 Design Specifications

According to Sidi (1997) any orbital change of a satellite is accompanied by a velocity change. This velocity change necessitates a certain quantity of fuel consumption. Orbit manoeuvres and changes can be adjusted by single and/or multiple thrust impulses. With a single thrust impulse very limited kinds of orbit changes can be achieved, whereas multiple thrust impulses can effect any desired orbit change. A rocket engine develops thrust by expelling propellant at a higher velocity relative to the satellite. The thrust F_T can be calculated as follows:

$$F_T = V_e \frac{dm}{dt} + A_e [p_e - p_a] = V_{ef} \frac{dm}{dt} \quad [N] \quad (3.1)$$

where p_e and p_a are the gas pressure and ambient pressure at the exit of the nozzle, V_e is the exhaust velocity, V_{ef} is the effective exhaust velocity of the expelled mass with respect to the satellite, dm/dt is the mass flow rate of the propellant, and A_e denotes the area of the nozzle exit.

The specific impulse I_{sp} of the thruster is a measure of the efficiency with which the propellant mass is converted into thrust energy. The I_{sp} of the thruster can be calculated by:

$$I_{sp} = \frac{F_T}{g \frac{dm}{dt}} \quad [s] \quad (3.2)$$

where g is the gravitational constant. A high specific impulse is indicative of a lower propellant consumption per unit thrust.

To calculate the velocity change per exhausted fuel mass, the acceleration F/m is integrated to find:

$$\Delta V = \int_{t_i}^{t_f} \frac{F_T}{m} dt = \int_{t_i}^{t_f} \frac{g I_{sp}}{m} \frac{dm}{dt} dt = g I_{sp} \int_{m_i}^{m_f} \frac{1}{m} dm \quad (3.3)$$

where t_i , t_f and m_i , m_f are the initial and final time and masses of the spacecraft. The solution, given below, is known as the rocket equation:

$$m_f = m_i \exp\left(-\frac{\Delta V}{gI_{sp}}\right) \quad (3.4)$$

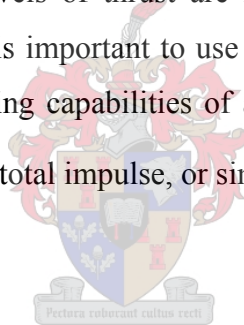
The mass m_p of propellant expelled from the satellite can then be calculated:

$$m_p = m_f - m_i = m_i \left[1 - \exp\left(-\frac{\Delta V}{gI_{sp}}\right) \right] \quad (3.5)$$

This equation is used to calculate the mass of propellant m_p required to change the velocity of the satellite by ΔV with an initial mass m_i . Increasing the specific impulse I_{sp} , will decrease the expelled mass of propellant.

According to Sidi (1997) propulsion systems are used for producing forces. Forces are used to increase the linear velocity of the satellite. Relatively large masses need to be accelerated and therefore high levels of thrust are necessary. Since the thruster must accelerate its own weight also, it is important to use thrusters and propellants with very high specific impulse I_{sp} . The lifting capabilities of a propulsion system are defined as

$\int_{t=0}^{\infty} F_T dt$; this is called the system total impulse, or simply the *impulse* in seconds.



4 Design Criteria of Experimental Set-up

In designing the experimental set-up it was decided to make use of an accumulator into which a metered amount of liquid butane could be fed. In the accumulator the butane is heated and then exhausted through the nozzle by opening the nozzle valve shown in Figure 4.1. The set-up also needed to be able to be placed inside the vacuum chamber that was used for the vacuum tests. A schematic diagram of the experimental set-up is shown in Figure 4.1 and a schematic diagram of the accumulator, in more detail, is shown in Figure 4.2. Refer to Figure D.1 in Appendix D for a photograph of the experimental set-up.

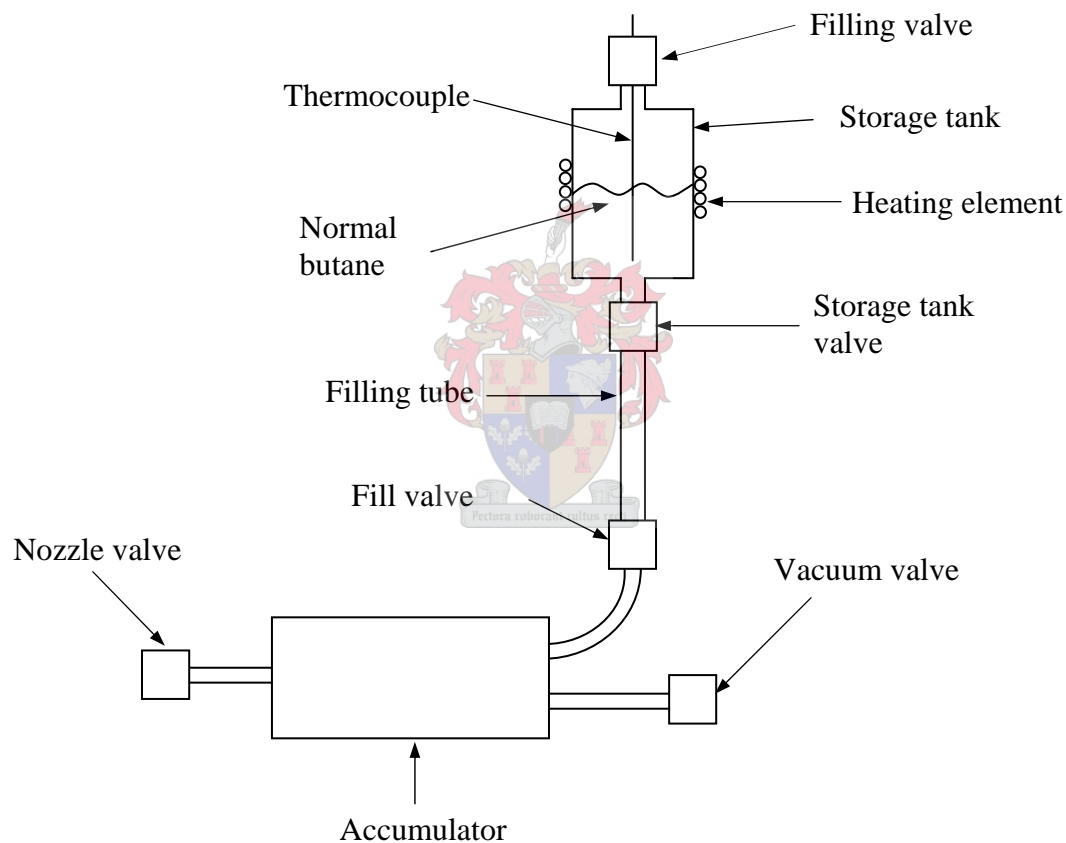


Figure 4.1 Schematic diagram of the experimental set-up

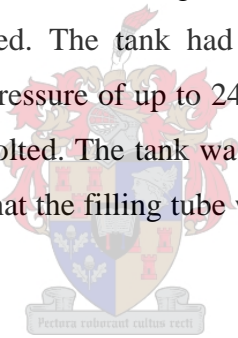
4.1 Nozzle

From ideal gas nozzle theory (Anderson, 2004) the appropriate size of the nozzle can be calculated. The inlet pressure and temperature, backpressure and the thrust force expected are all specified. For these specified conditions the nozzle size can then be calculated. There is no optimum sized nozzle as the inlet pressure varies continually

during a firing. However to extend the previous work done by Weyer (2004) and Rosenberg (2005) the same nozzle used in their projects was used for the initial tests. The nozzle had a throat diameter of 1 mm and an exit diameter of 5 mm while the length of the divergent part of the nozzle was 10 mm. Later a second nozzle was tested which had a throat diameter of 1 mm and an exit diameter of 1.6 mm. These two nozzles were tested under both atmospheric and vacuum conditions.

4.2 Liquefied Gas Container (Storage Tank)

The tank in which the butane was stored was a stainless steel cylinder. The container had two openings, one on either side of the cylinder. A needle valve and thermocouple was connected to the one end of the cylinder. The needle valve was used to fill the container with butane. On the other end of the container a solenoid valve was used to fill the filling tube with liquid butane. Between the storage tank and the filling tube a Parker Hannifin (direct acting, normally closed, 1/8", part number 363380) solenoid valve was used. The tank had a flange welded to it and was designed to be able to handle a pressure of up to 24 bar. A stand was made to which the flange of the tank could be bolted. The tank was supported such that it was in an upright position (Figure 4.1) so that the filling tube would be filled with liquid butane only.



4.3 Filling Tube

A 13 mm glass tube was used as a filling tube. The purpose of the tube was to be able to calculate the mass of liquid butane that was fed into the accumulator from the storage tank. By using a glass filling tube the precise initial liquid butane charge could be visibly verified. The volume of the filling tube was 13 ml.

4.4 Accumulator

The accumulator is similar to the Mark-III thruster discussed in Sweeting et al. (1999). Copper mesh was used (instead of the silicone carbide spheres) to improve the heat transfer rate at which the vapour could be heated. Copper has a higher heat transfer coefficient and also the surface area of the mesh is much higher than the carbide spheres. Figure 4.2 shows a schematic of the accumulator. Refer to Figure D.3

in Appendix D for a photograph of the accumulator and Figure D.4 for a photograph of the flange with mesh placed around the heating element and thermocouple pockets.

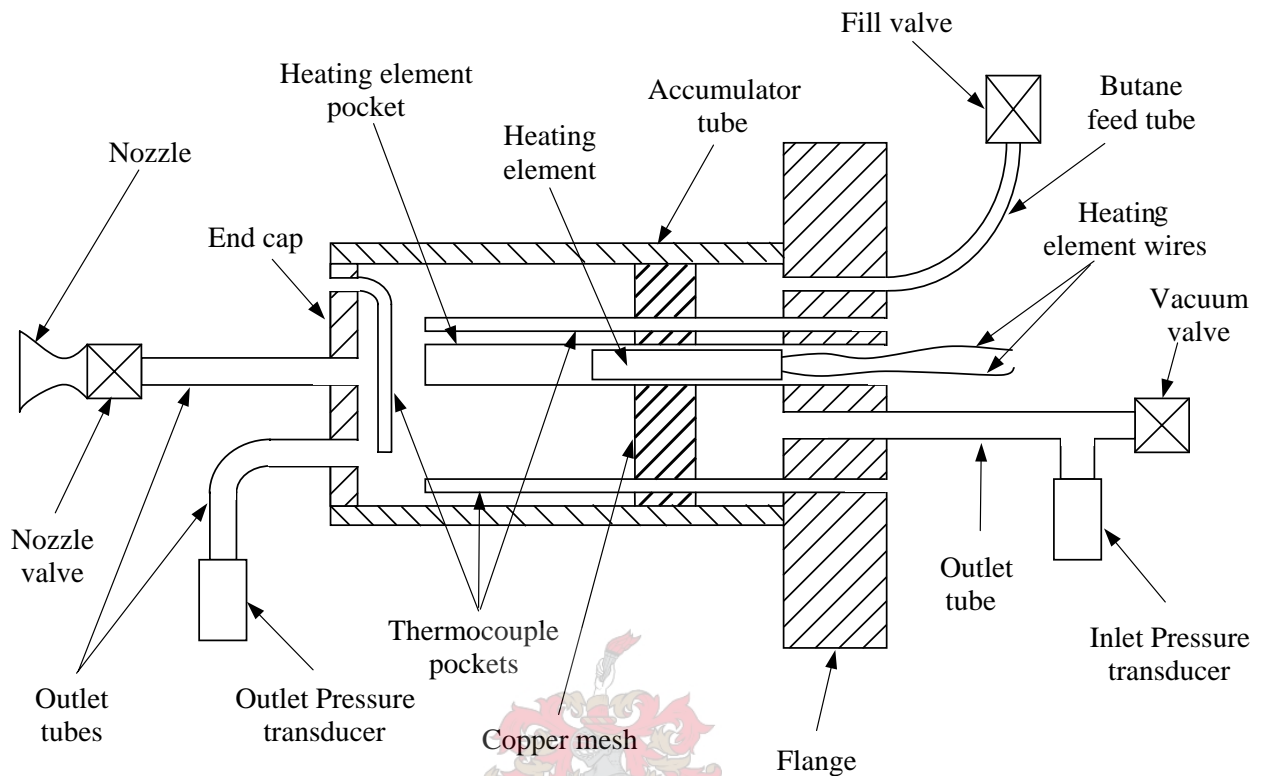


Figure 4.2 Schematic of accumulator

The accumulator consisted of a 52 mm inside diameter stainless steel tube with a flange on the one side and an end cap on the other. The volume of the accumulator, without any mesh inside was 417 ml. When mesh was placed inside, the volume of the mesh was calculated and then subtracted from the total volume of the accumulator to get the free volume.

In Figure 4.2 it can be seen that there are three tubular pockets inside of the accumulator tube that are welded onto the flange. Two of the pockets are used as thermocouple pockets, while the other one is used for placing a heating element inside of it. In Figure 4.2 there is also a butane feed tube welded onto the flange coming out of the accumulator tube. This feed tube is used to feed the charge of liquid butane from the filling tube via the fill valve into the accumulator. The outlet tube is connected to a pressure transducer and a vacuum valve. This vacuum valve is connected to a vacuum pump to draw a vacuum in the accumulator and filling tube. A

vacuum had to be drawn after each test to ensure that no air or butane was left in the accumulator after the test.

The copper mesh in Figure 4.2 is mesh discs that were cut out so that it would fit inside of the accumulator tube. There were three holes punched into the discs so that it could be slid around the heating element pocket and two thermocouple pockets. These pockets also acted as supports for the mesh.

In Figure 4.2 it can be seen that there is only one thermocouple pocket welded onto the end cap that is on the inside of the accumulator tube. In the figure it can be seen that the pocket is bent so that it runs across the outlet tubes. This is done so that the thermocouple can measure the temperature of the gas leaving the accumulator through the nozzle valve. The one outlet tube coming out of the accumulator is connected to the nozzle valve, while the other outlet tube is connected to the outlet pressure transducer.

There were three valves attached to the accumulator. The fill valve was the same type of Parker Hannifin (direct acting, normally closed, 1/8", part number 363380) solenoid valve used between the storage tank and the filling tube. This valve was used to feed the charge of liquid butane into the accumulator. The nozzle and vacuum valves were Sirai (direct acting, normally closed, 1/8", part number Z610A) solenoid valves. The nozzle valve was connected to the nozzle through which the butane was exhausted out of the accumulator.

4.5 Heating

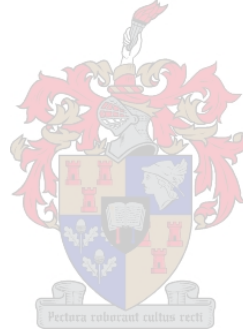
Copper mesh with 40 holes per linear 25.4 mm and a wire thickness of 0.26 mm was used to improve the heat transfer rate at which the vapour could be heated.

The heating element used was a 500 W, 240 V firerod. It was placed inside the heating element pocket, as shown in Figure 4.2. A variable voltage source was connected to it to provide the power.

4.6 Sloshing

According to Weyer (2004) when liquid is stored inside a tank on a satellite, there will be a significant amount of mass on board the satellite that will not be rigidly attached to the satellite structure. This can lead to a phenomenon known as sloshing. Sloshing refers to the free surface oscillations of a liquid in a partially filled tank. This liquid motion in the propellant tanks can have a significant influence on the attitude of the dynamics, since sloshing of propellants may adversely affect the stability of a space vehicle and the integrity of the tank structure.

Because no dynamic tests were conducted in this project, the sloshing of the propellant inside of the storage tank would not play a roll on the tests that were conducted. If it were desired to do dynamic tests the storage and sloshing of the liquid butane would have had to be looked at in more detail.



5 Experimental Set-up

5.1 Measurement and Control

The experimental work required accurate measurement of temperature, pressure and thrust force, and the control of the solenoid valves using a personal computer. All the measurements and control were done using commercially available data acquisition hardware and software. The input/output (I/O) hardware used was a *National Instruments PCI-6014 basic multifunction DAQ board* (serial number 188626D-01). The software used for the communication with the I/O device was *LabView 7.1*.

5.1.1 Control of solenoid valves

The normally closed solenoid valves which were used required a 24 V direct current voltage to open. The power input terminals of the valves were connected to a relay board. The relay board was supplied with a 24 V direct current voltage from a power supply. The power supply was plugged into a 220 V alternating current wall socket. The relay switches required a 5 V signal to send power to the valves. This 5 V signal was sent to the relay board from the multifunction DAQ I/O card in the personal computer (PC). A diagram of the system is shown in Figure 5.1. The power rating of the valves were 6 W, thus typical current drawn by the valves was about 0.25 A.

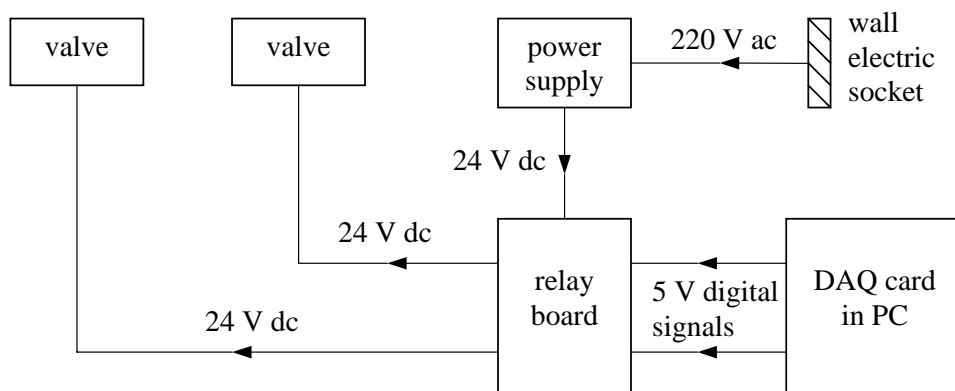


Figure 5.1 Diagram of valve control system

It was possible to control the sequence of the valves opening using the *LabView* software on the personal computer. The sequence was developed so that the nozzle valve could be operated in a pulsed fashion. The user could specify the time length of

the pulse for the valve to be opened, as well as the time during which the valve was closed.

5.1.2 Temperature measurement

Chromel and alumel (type K) thermocouples were used to determine the temperature of the butane inside of the accumulator, while a copper-constantan (type T) thermocouple was used to determine the temperature of the butane in the storage tank. The voltage from the different thermocouples were read in on some of the channels of the I/O card using the software that was supplied with the card to automatically convert the voltage differences to temperature units in °C.

In the configuration of the thermocouples the cold junction compensation (CJC) value needs to be set. The default value is 25 °C. The CJC value was determined using a calibrated sub-standard platinum resistance thermometer, model number 935-14-72. The CJC value was set at 23.4 °C. The thermocouples were placed in water at different temperatures, with the platinum resistor. The values measured are given in Table 5.3.

Table 5.3 Measured values from thermocouples and platinum resistor

Platinum resistor [°C]	Thermocouple [°C]	Error [%]
16.6	16.7	0.60
18.2	18.3	0.55
27	26.8	0.74
38.2	37.6	1.57

Figures 5.2 and 5.3 show the temperatures measured with the thermocouples placed in steam from boiling water and in a well stirred ice bucket.

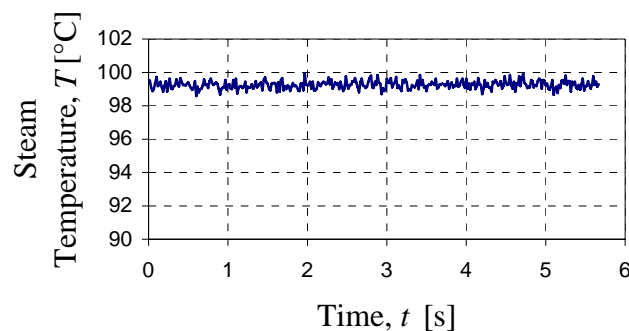


Figure 5.2 Steam temperature versus time

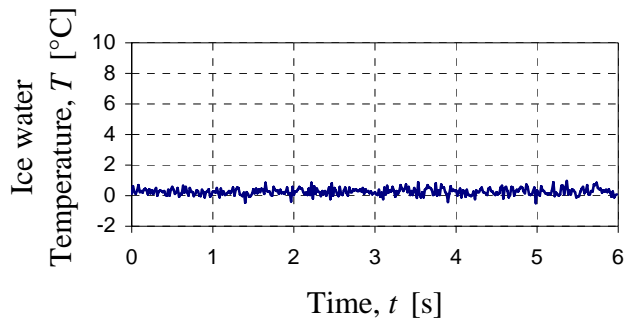


Figure 5.3 Ice water temperature versus time

5.1.3 Filtering of temperature data

Figure 5.4(a) is a graph depicting temperature versus time recorded in a stable temperature environment of about 18 °C. It can be seen that the data appears very erratic with variation of about 0.6 °C either side of the average. These temperatures were sampled using a type K thermocouple. The channel with which the temperature was sampled was set to a maximum resolution in the range of -1.2 to 4.1 mV, corresponding to a temperature range of -5 to 100 °C. The specific noise level on the card for this range is approximately 50 μ V. From tables for type K thermocouples it can be seen that a change of 1 °C correlates to a change of approximately 40 μ V. The thermocouples were connected to the DAQ card with no pre-amplification, thus the noise must be generated from the card. This noise can be eliminated to some extent by filtering the data through a low pass filter. In the program used to read in the signals, *LabView*, there are a number of numerical filters available. A second order Butterworth low-pass filter with a cut-off frequency of 10 Hz was used to filter the temperature readings. Figure 5.4(b) shows the same data as shown in Figure 5.4(a), only filtered through the low-pass Butterworth filter.

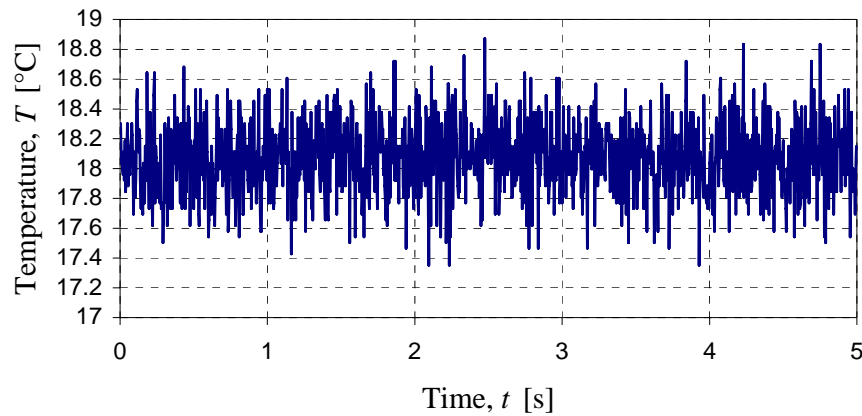


Figure 5.4(a) Temperature data – unfiltered

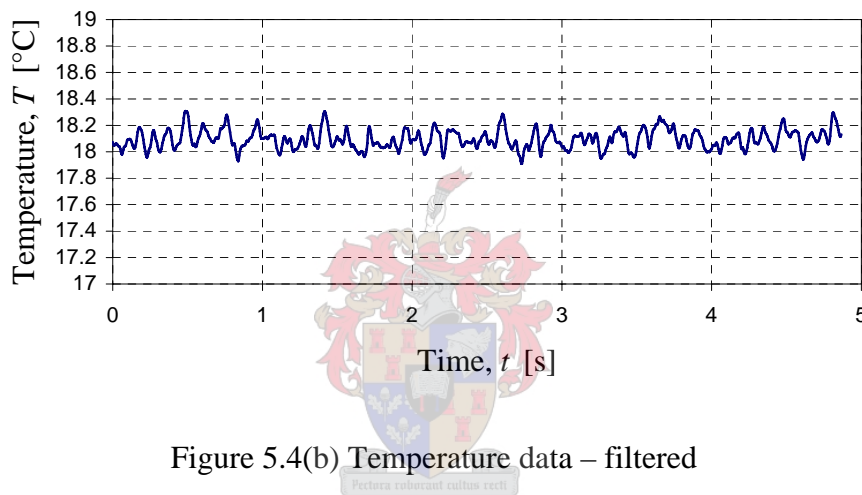


Figure 5.4(b) Temperature data – filtered

5.1.4 Pressure measurement

The pressure was measured using Hottinger Baldwin Messtechnik absolute pressure transducers. Two pressure transducers were used to measure the pressure inside the accumulator. One was placed at the liquid charge inlet of the accumulator while the other one was placed at the outlet (nozzle end) of the accumulator. The pressure transducer used at the inlet of the accumulator had a range of 0 – 50 kPa. The pressure transducer used at the outlet of the accumulator had a range of 0 - 10 kPa. (The reason two different pressure transducers were used, was due to availability).

The reason two pressure transducers were placed on either side of the accumulator was to see if a pressure drop could be observed across the mesh inside of the accumulator. From the results it was shown that there was no measurable pressure drop across the mesh. The pressure transducers were both connected to a bridge

amplifier. The bridge amplifier gave an output signal of between -10 V and 10 V . This output was connected to the DAQ card from where the data was read into the personal computer.

5.1.5 Thrust measurement

The accuracy with which the thrust could be measured played a major role in the experimental set-up. Due to the relatively small thrust values measured, special consideration had to be given to the measurement method. The method that was employed is similar to that discussed by Ye et al. (2001), Xiong et al. (2002), Stephen et al. (2004) and Behkam et al. (2004). All of the methods discussed in these articles, make use of a cantilever beam. In this project a cantilevered beam is used to measure the thrust directly, as is discussed by Behkam et al. (2004).

Description of method used

In this project the thruster was mounted such that it fired onto the tip of the cantilever beam, the same as is discussed by Ye et al. (2001) and Xiong et al. (2002). The cantilever beam was mounted on a stand that could be adjusted in front of the nozzle such that the free end of the beam could be aligned with the nozzle. When the thruster is firing, the cantilever beam deflects and a strain is induced due to the bending moment caused by the propellant exiting the nozzle and hitting against the free end of the beam. The maximum strain is induced at the supporting end of the beam. The strain gauges were mounted as close as possible to the supporting end of the beam in order to measure as high a strain as possible.

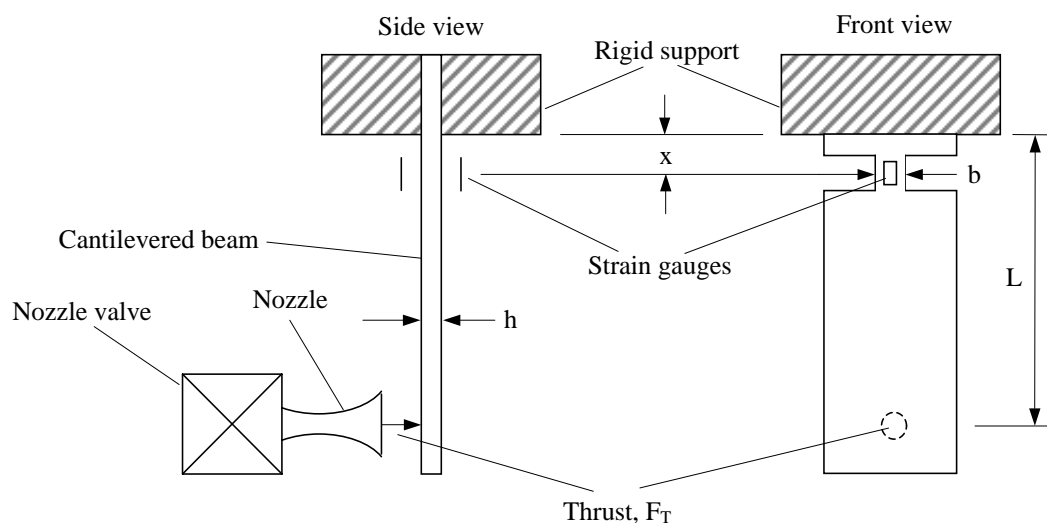


Figure 5.5 Method of measuring thrust using a cantilevered beam

From general solid mechanics the bending moment M , a distance x away from the fixed end, resulting from a tip load F on a cantilever of length L is:

$$M = F(L - x) \quad (5.1)$$

The resulting normal stress σ_x (in the axial direction) on the surface of the beam is:

$$\sigma_x = -\frac{My}{I_{yy}} \quad (5.2)$$

where y is the distance from the neutral axis to the outer surface of the beam, and I_{yy} is the area moment of inertia about the y -axis.

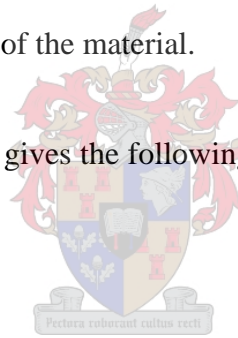
From the stress strain relations (Benham, et al., 1999) the strain in the x -direction is given by:

$$\varepsilon_x = \frac{\sigma_x}{E} \quad (5.3)$$

where E is the Young's modulus of the material.

Rearranging the above equations gives the following expression for the thrust force as a function of the strain:

$$F = -\frac{\varepsilon_x I_{yy} E}{(L - x)y} \quad (5.4)$$



Effect of beam stiffness on strain resolution

Due to the small thrust expected careful consideration must be given to the parameters determining the stiffness of the measuring structure. The parameters affecting the stiffness of the beam are the material, length and sectional inertia properties of the beam. Typically, the smallest strain that can be measured by a strain gauge is in the region of 0.5×10^{-6} . It is important to ensure that the set-up is not so stiff that the strain registered is too small for the capabilities of the measuring equipment. However, the stiffer the beam is, the easier it will be to calibrate the beam. Therefore, as stiff a beam as possible capable of measuring the thrust accurately was chosen.

A relatively stiff beam was made from stainless steel ($E = 1.96 \times 10^{11}$ N/m², with length $L = 0.2$ m, width $b = 0.036$ m and thickness $h = 0.002$ m). The strain gauges were mounted a distance $x = 0.027$ m from the supported end.

Moment of inertia: I_{yy}

$$I_{yy} = \frac{bh^3}{12} = \frac{0.036 \times 0.002^3}{12} = 2.4 \times 10^{-11} \quad [\text{m}^4] \quad (5.5)$$

Different forces were applied at the free end of the beam. The expected strain, ε_x , for a 1 N force is:

$$\begin{aligned} \varepsilon_x &= -\frac{F(L-x)y}{I_{yy}E} = -\frac{(1)(0.2-0.027)(-0.001)}{(2.4 \times 10^{-11})(1.96 \times 10^{11})} \\ &= 3.667 \times 10^{-5} \quad [\text{m/m}] \\ &= 36.77 \quad [\mu\text{m/m}] \end{aligned} \quad (5.6)$$

Similarly the expected strain for a 0.5 N force was 18.39 $\mu\text{m/m}$ and for a 0.1 N force the strain was expected as 3.68 $\mu\text{m/m}$.

The strain gauges were connected to the bridge amplifier to measure the thrust experimentally. The strain gauge bridge used is discussed in the following section. From the tests done with the relatively stiff beam it was found that a theoretical strain as small as ± 4 $\mu\text{m/m}$ could be measured accurately with the instrumentation. A second beam with thickness $h = 0.0009$ m was tested. The strain gauges was placed where the beam had a width of $b = 0.009$ m at a distance $x = 0.023$ m from the supported end. The thrust is applied at a length $L = 0.19$ m.

Moment of Inertia: I_{yy}

$$I_{yy} = \frac{bh^3}{12} = \frac{0.009 \times 0.0009^3}{12} = 5.47 \times 10^{-13} \quad [\text{m}^4] \quad (5.7)$$

Different forces were applied at the free end of the beam. The expected strain, ε_x , for a 100 mN force was:

$$\varepsilon_x = -\frac{F(L-x)y}{I_{yy}E} = -\frac{(0.1)(0.19-0.023)(0.00045)}{(5.47 \times 10^{-13})(1.96 \times 10^{11})} \quad (5.8)$$

$$= 70.13 \quad [\mu\text{m/m}]$$

Similarly the expected strain for a 0.05 N force was 35.06 $\mu\text{m/m}$ and for a 0.01 N force the strain expected was 7.01 $\mu\text{m/m}$. The expected thrust was in the region of 0.1 N and since the experimental results show that a strain as small as $\pm 4 \mu\text{m/m}$ could be measured the sensor with a thickness of 0.0009 m would be able to measure a thrust accurately even for a thrust as low as 0.01 N. Therefore it was decided to use the sensor with a thickness of 0.0009 m to measure the thrust force.

Strain gauge configuration

To measure the thrust, two strain gauges were attached opposite each other on the beam in order to form a temperature compensated half bridge as shown in Figure 5.6. Note that only R_1 and R_2 are active strain gauge resistances. R_3 and R_4 are merely additional resistances (within the bridge amplifier) used to complete the Wheatstone bridge.

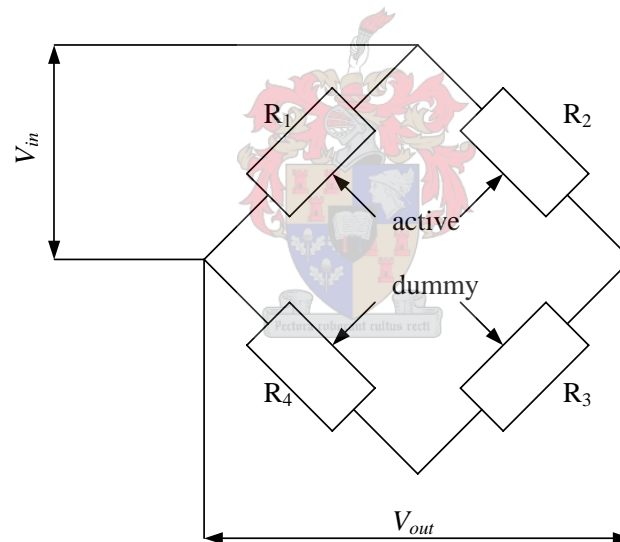


Figure 5.6 Strain gauge configuration to measure thrust

The general equation for the voltage V_{out} given a change in the resistance ΔR of the strain gauges, for an input voltage V_{in} applied over the bridge is (Boctor et. al, 1997):

$$\frac{V_{out}}{V_{in}} = \frac{1}{4} \left[\frac{\Delta R_1}{R_1} - \frac{\Delta R_2}{R_2} + \frac{\Delta R_3}{R_3} - \frac{\Delta R_4}{R_4} \right] \quad (5.9)$$

The basic strain gauge equation is given by

$$\frac{\Delta R}{R} = K\varepsilon \quad (5.10)$$

where K is the gauge factor (equal to 2.075 for the strain gauges used). In the bridge considered, R_3 and R_4 do not take part in the deformation and equation 5.9 becomes:

$$\frac{V_{out}}{V_{in}} = \frac{K}{4}[\varepsilon_1 - \varepsilon_2] \quad (5.11)$$

Gauges 1 and 2 are mounted directly opposite each other on the cantilevered beam; hence they experience the same magnitude of strain in the axial direction but of different sign, i.e.:

$$\varepsilon_1 = -\varepsilon_2 = \varepsilon_x \quad (5.12)$$

Hence the ratio of input over output voltage would be:

$$\frac{V_{out}}{V_{in}} = \frac{K}{4}[2\varepsilon_x] = \frac{K}{2}\varepsilon_x \quad (5.13)$$

It is easily shown that this bridge is temperature compensated. Assume a strain due to bending of the cantilever of $\varepsilon_1 = \varepsilon_x$ and $-\varepsilon_2 = \varepsilon_x$. Additionally assume a strain induced due to temperature of ε_T in both gauges. Hence, the strains experienced in gauge 1 and 2 are as follows:

$$\varepsilon_1 = \varepsilon_x + \varepsilon_T \quad (5.14)$$

$$\varepsilon_2 = -\varepsilon_x + \varepsilon_T \quad (5.15)$$

Substituting the above two expressions into equation 5.11 gives the following expression, which is exactly the same as that given in equation 5.13:

$$\frac{V_{out}}{V_{in}} = \frac{K}{4}[(\varepsilon_x + \varepsilon_T) - (-\varepsilon_x + \varepsilon_T)] = \frac{K}{2}\varepsilon_x \quad (5.16)$$

The theory presented in this section would be used if the thrust generated would be calculated theoretically from the voltage output that is received from the bridge amplifier. However, for the experimental work the thrust measurement was also calibrated as described in section 5.2.2.

5.2 Calibration

5.2.1 Pressure sensor calibration

The pressure transducers were calibrated using a high pressure hydrostatic pump. The voltage output from the bridge amplifier was then compared to the pressure reading on a calibrated pressure gauge. The graphs shown below depict the pressure versus

voltage reading. A straight line was fitted through each of the data sets to give the calibration equations 5.17 and 5.18 (p in kPa and V in volts). The R^2 values are the coefficients of determination, an indicator ranging from 0 to 1 that reveals how closely a corresponding curve corresponds to the actual data. The closer R^2 is to 1 the better the correlation.

Inlet end pressure transducer:

$$p = 325.12 \times V \quad (5.17)$$

$$R^2 = 1.00$$

Outlet end pressure transducer:

$$p = 99.375 \times V \quad (5.18)$$

$$R^2 = 1.00$$

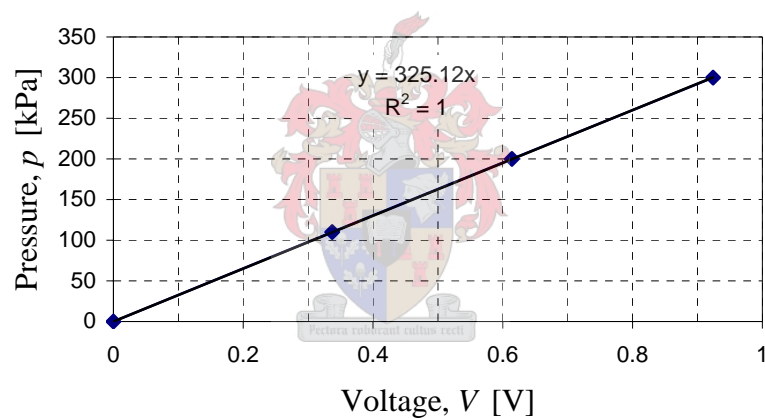


Figure 5.7 Pressure sensor calibration for inlet end pressure transducer

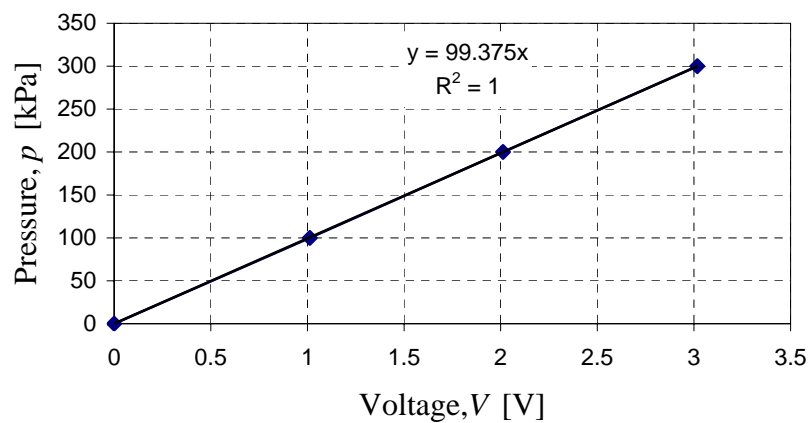


Figure 5.8 Pressure sensor calibration for outlet end pressure transducer

5.2.2 Thrust sensor calibration

In section 5.1.5 a theoretical method to calculate the thrust was presented. To eliminate experimental errors the thrust gauge was calibrated experimentally. These errors can be due to a slight misalignment of the strain gauges – the gauges might not be perfectly aligned with the beam axis and might not be exactly opposite each other. Additional errors might be due to the accuracy and noise of the instrumentation. Another source of errors could be due to slight local stress concentrations on the material on to which the strain gauges were attached.

Calibration was done by placing mass pieces on the cantilever at a position opposite the nozzle exit. The force was calculated by multiplying the weight of the mass pieces with the gravitational acceleration g (9.81 m/s^2). The resulting strain was measured for each applied force and a plot was made of the force against the voltage measured. A straight line was obtained by performing a least squares fit of the data to give the calibration equation. The plot of force against voltage can be seen in Figure 5.9. The calibration equation (with $R^2 = 1.00$) for the thrust F_T in N as a function of voltage V in V is:

$$F_T = 0.5654 \times V \quad (5.19)$$

In the case of the thrust sensor the R^2 value was also equal to 1.

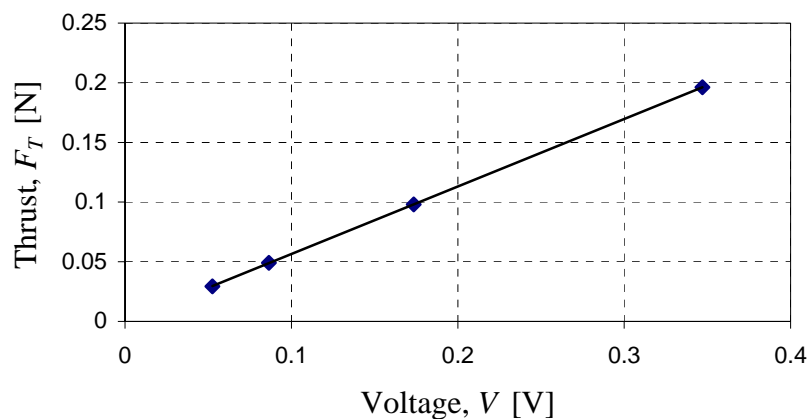


Figure 5.9 Thrust sensor calibration

It is useful to check the error between experimental and theoretical results for the strain gauges by comparing the voltage output from the experimentation and the expected voltage from the theory. This comparison is done in Appendix C.1 and the results are given in Table C.1 and Figure C.1.

5.3 Charging Procedure

The accumulator was charged with 13 ml of liquid butane. This butane was then heated to a certain pressure inside the accumulator before it was exhausted through the nozzle. A schematic of the experimental set-up for the filling procedure is shown in figure 5.1.

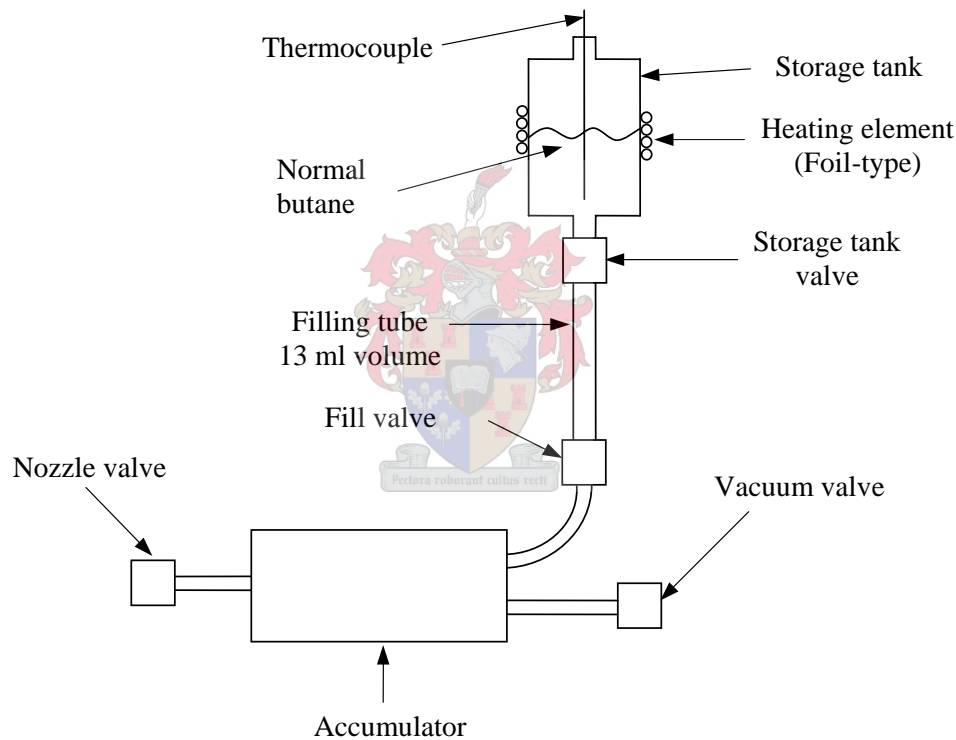


Figure 5.10 Schematic diagram of filling set-up (Figure 4.1 repeated)

To ensure that the filling tube would be filled with liquid butane and no butane vapour and that all the liquid would run into the accumulator, the storage tank was heated and a vacuum was drawn in both the accumulator and the filling tube. The storage tank was heated, using a foil type heating element wound around the tank that was connected to a variable power supply. A thermocouple was placed in the tank so that the temperature in the tank could be monitored.

The vacuum valve (shown in Figure 5.10) was connected to the vacuum pump (two-stage Galileo TEC). To draw a vacuum in the filling tube and the accumulator both the vacuum and fill valves needed to be opened.

After the storage tank was heated to ± 40 °C and a vacuum was drawn in the filling tube and the accumulator, the filling tube can be filled. The storage tank valve is opened until the filling tube is filled with liquid butane. Once the filling tube is full the storage tank valve is closed and the fill valve is opened until all the liquid butane has run down into the accumulator. When the filling tube is empty the fill valve can be closed.

5.4 Vacuum Chamber Tests

To validate the theoretical results obtained from the analytical model of the system under space conditions a set of tests were also conducted in a vacuum chamber. These tests were done in a vacuum of ± 20 Pa, compared to the atmospheric conditions of $\pm 100\,000$ Pa. Testing under these conditions would ensure that no shockwaves would form inside of the nozzle.

The storage tank and filling tube was not able to fit into the vacuum chamber. After the accumulator was charged with liquid butane the storage tank and filling tube was removed and only the accumulator placed in the vacuum chamber.

6 Thermo-fluid Modelling of the System

The thermo-fluid modelling of a thruster system can be a very powerful tool in the design of thruster systems. It can be used to predict the behaviour and performance of such a system for different operating conditions. If the numerical model is able to simulate accurately the performance of the thruster system, a lot of time and money can be saved in the development of the thruster system. For instance, different nozzles, pressures and temperatures can be simulated without actually having to do the tests. For this reason a mathematical model was developed.

The liquefied gas thruster system was approximated as being one-dimensional flow problem and a control-volume approach was taken in applying the equations of change. In addition the time dependence of the system was taken into account, i.e. the transient thermal and flow behaviour of the system was also modelled. Idealised gas dynamics were used to model the flow through the nozzle. A two-phase model was used to model the transient behaviour of the butane inside the accumulator.

In order to establish the validity of the mathematical model, experiments were conducted and the results from the two were compared. The design and experimental set-up has already been discussed in the chapters 4, and 5 while the results are given in chapter 7.

6.1 Idealized Gas Dynamics

To calculate the thrust the following exit properties of the flow at the exit plane of the nozzle need to be known: \dot{m}_e , V_e and p_e . These properties were calculated using traditional gas dynamic theory (Anderson, 2004 and White, 1999). Simplified gas dynamics assumes a reservoir of gas at constant pressure and temperature. In modelling of the system this is not the case as the pressure inside the reservoir starts to drop as soon as the valve is opened. However the assumption was made that the velocity of the fluid at the entrance of the nozzle is low enough to assume that the pressure and temperature is equal to the stagnation pressure and temperature of the reservoir or accumulator. The flow of the fluid through the nozzle was modelled as a single control volume. The stagnation properties of the fluid inside the accumulator

were taken as the initial conditions for each new time step. Figure 6.1 shows the control volume for the nozzle.

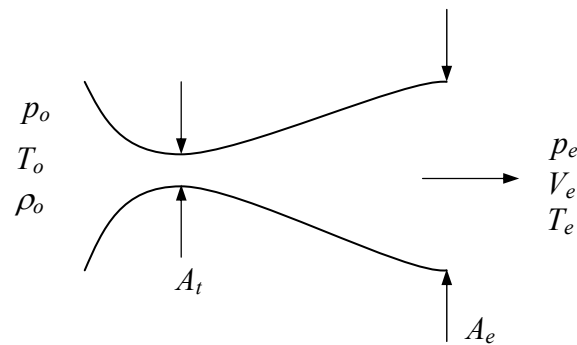


Figure 6.1 Nozzle control volume

The other assumptions made in the theory of the gas flow through the nozzle are: the fluid behaves as an ideal gas, it is a calorically perfect gas, no frictional losses occur inside the accumulator, and isentropic flow through the nozzle. According to Anderson (2004) an ideal gas is one in which intermolecular forces are neglected. By ignoring these forces the so-called ideal gas equation of state will hold:

$$p = \rho RT \quad (6.1)$$

where p is the pressure, T is the absolute temperature and ρ is the density. R is the specific gas constant and equal to the universal gas constant divided by the molecular mass. For an ideal gas the specific gas constant is assumed to be a constant. Also, for constant specific heats the fluid can be considered a calorically perfect gas. When the assumptions above are made for a fluid then the following relations for the properties of the fluid through a quasi one-dimensional duct are valid (Anderson, 2004):

$$\frac{T_o}{T} = 1 + \frac{\gamma - 1}{2} M^2 \quad (6.2)$$

$$\frac{p_o}{p} = \left(1 + \frac{\gamma - 1}{2} M^2 \right)^{\frac{\gamma}{\gamma - 1}} \quad (6.3)$$

$$\frac{\rho_o}{\rho} = \left(1 + \frac{\gamma - 1}{2} M^2 \right)^{\frac{1}{\gamma - 1}} \quad (6.4)$$

where γ is the specific heat ratio equal to C_p/C_v . M is the Mach number defined as:

$$M = \frac{V}{a} \quad (6.5)$$

where V is the velocity of the gas and a is the speed of sound in the gas. The speed of sound is calculated using:

$$a = \sqrt{\gamma RT} \quad (6.6)$$

The numerical model used these simple relations to calculate the properties of the fluid exiting the nozzle in order to be able to calculate the thrust of the thruster system.

When given the initial conditions to the fluid properties and nozzle dimensions, then it is possible to calculate the exit properties of the fluid and hence the thrust of the system. The initial conditions that are given are:

- Stagnation pressure, p_o and temperature, T_o
- Back pressure, p_B
- Nozzle dimensions: exit area, A_e and throat area, A_t

The density, ρ_o can be calculated using the ideal gas equation.

In the flow through the nozzle there are different possible scenarios. These are:

- No flow through the nozzle (this would happen when $p_o = p_B$)
- Subsonic flow through the entire nozzle
- Sonic flow at the throat and subsonic flow through the rest of the nozzle
- Sonic flow at the throat, while “shock free” supersonic flow through the rest of the nozzle
- Sonic flow at the throat, while supersonic flow through the rest of the nozzle with oblique shockwaves forming after the exit plane
- Sonic flow at the throat, while supersonic flow through the rest of the nozzle with expansion waves forming after the exit plane
- Sonic flow at the throat, supersonic flow until a normal shock wave is formed in the nozzle, and then subsonic flow through the rest of the nozzle.

In order to be able to determine which particular scenario would occur three different exit pressures need to be calculated. These are:

- p_{sup} - when supersonic flow exists throughout the nozzle
- p_{sub} - when subsonic flow exists from the throat to the exit plane of the nozzle
- p_{norm} - when a normal shockwave exists in the divergent part of the nozzle

For $p_{sup} = p_B$ sonic flow will occur at the throat of the nozzle with supersonic flow through the rest of the nozzle.

For $p_{sup} < p_B < p_{norm}$ sonic flow will occur at the throat of the nozzle with supersonic flow through the rest of the nozzle. An oblique shockwave will occur after the exit plane of the nozzle.

For $p_{sup} > p_B$ sonic flow will occur at the throat of the nozzle with supersonic flow through the rest of the nozzle. Expansion waves will occur after the exit plane of the nozzle.

For $p_{norm} = p_B < p_{sub}$ sonic flow will occur at the throat of the nozzle with supersonic flow until an oblique shockwave will occur inside the diverging part of the nozzle. After the shock wave subsonic flow will occur in the rest of the nozzle.

For $p_B = p_{sub}$ sonic flow will occur at the throat of the nozzle with subsonic in the rest of the nozzle.

For $p_B > p_{sub}$ subsonic flow in entire nozzle.

With the given initial conditions the flow through the nozzle can be numerically modelled. The first step is to calculate the properties of the fluid at the throat for sonic flow. Sonic flow at the throat means that the flow at the throat will be critical, and the flow is classified as critical when the Mach number, M , is equal to 1. The following relations apply for the properties in the throat:

$$p_t = p_o \left(\frac{2}{\gamma + 1} \right)^{\frac{\gamma}{\gamma - 1}} \quad (6.7)$$

$$T_t = \frac{2T_o}{\gamma + 1} \quad (6.8)$$

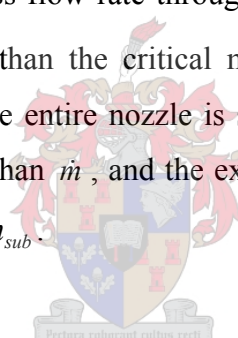
$$\rho_t = \rho_o \left(\frac{2}{\gamma + 1} \right)^{\frac{1}{\gamma - 1}} \quad (6.9)$$

$$a = \sqrt{\gamma R T_t} \quad (6.10)$$

$$V_t = \sqrt{2C_p(T_o - T_t)} \quad (6.11)$$

$$\dot{m} = a \rho_t A_t \quad (6.12)$$

where p_t is the critical pressure at the throat, T_t the temperature, ρ_t the density, a the speed of sound, V_t the velocity of the fluid and \dot{m} the mass flow at the throat. If the flow through the throat of the nozzle is critical, then the mass flow rate through the entire nozzle is equal to the mass flow rate through the throat. Thus, $\dot{m}_e = \dot{m}$. The mass flow can never be more than the critical mass flow through the throat \dot{m} . However, if the flow through the entire nozzle is subsonic, i.e. $M < 1$ at the throat, then the mass flow will be less than \dot{m} , and the exit mass flow rate would equal the subsonic mass flow rate, $\dot{m}_e = \dot{m}_{sub}$.



Subsonic flow with sonic flow in throat

The flow conditions at the exit of the nozzle can now be calculated using the known properties of the flow at the throat. In order to know whether the flow through the divergent part of the nozzle is subsonic or supersonic, the flow is assumed to be subsonic from the throat to the exit of the nozzle. An iteration process was used to calculate the exit conditions. Because an iteration process was used, a value for the exit velocity was chosen. The equations used to calculate the flow through the nozzle, whether subsonic or supersonic, are the same and therefore it is important that the value chosen for the velocity is in the right order. For subsonic conditions the flow slows down through the nozzle, so a value smaller than the speed of sound through the nozzle throat was chosen. In this case a starting value for the velocity of half that of the speed of sound at the throat was chosen.

The exit properties are calculated using this chosen exit velocity. After the exit properties are calculated a new exit velocity is also calculated. If this newly calculated exit velocity is lower than the one chosen at the beginning a new lower value for the exit velocity is calculated by subtracting a small value from the exit velocity chosen at the beginning. The exit properties and exit velocity are recalculated again using this new chosen exit velocity. This process is repeated and a small value is subtracted from the chosen velocity until the chosen velocity is equal to or within a certain specified range of the value calculated. However if the calculated value of the velocity in the first calculation is higher than the chosen one a higher chosen velocity is calculated by adding a small value until the chosen velocity is satisfactory.

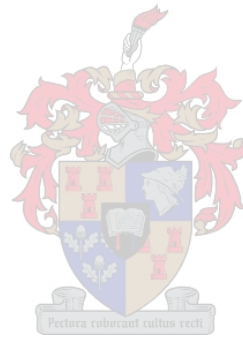
The equations used to calculate the exit conditions are:

$$T_{sub} = \frac{2C_p T_t + a^2 - V_{sub}^2}{2C_p} \quad (6.13)$$

$$p_{sub} = p_t \left(\frac{T_{sub}}{T_t} \right)^{\frac{\gamma}{\gamma-1}} \quad (6.14)$$

$$\rho_{sub} = \frac{p_{sub}}{RT_{sub}} \quad (6.15)$$

$$V_{sub} = \frac{\dot{m}}{\rho_{sub} A_e} \quad (6.16)$$



Using these equations the properties of the flow at the exit of the nozzle are determined.

The exit pressure calculated can now be compared to the backpressure. If the pressure at the exit is higher than that of the backpressure, the flow is supersonic through the divergent part of the nozzle. However if the calculated pressure is lower than the backpressure, the flow is subsonic throughout the nozzle and the sonic conditions at the throat is no longer valid. If the pressure is exactly equal to that of the backpressure, the sonic conditions at the throat is valid and the flow is subsonic through the rest of the nozzle.

Supersonic flow

If the subsonic pressure is found to be higher than the backpressure, then the properties of the fluid need to be calculated for supersonic flow from the throat to the exit plane of the nozzle. The area-Mach number relation is used to calculate the supersonic flow properties at the exit of the nozzle. The relation is given by:

$$\left(\frac{A}{A^*}\right) = \frac{1}{M^2} \left[\frac{2}{\gamma+1} \left(1 + \frac{\gamma-1}{2} M^2 \right) \right]^{\frac{\gamma+1}{\gamma-1}} \quad (6.17)$$

The same iterating methodology was followed as that used in the calculation of the flow properties for the subsonic flow conditions. A Mach number was however chosen instead of the velocity. For the case of supersonic flow in the nozzle the Mach number must be greater than one.

$$T_{sup} = \frac{T_o}{1 + \frac{\gamma-1}{2} M^2} \quad (6.18)$$

$$p_{sup} = \frac{p_o}{\left(1 + \frac{\gamma-1}{2} M^2 \right)^{\frac{\gamma}{\gamma-1}}} \quad (6.19)$$

$$\rho_{sup} = \frac{\rho_o}{\left(1 + \frac{\gamma-1}{2} M^2 \right)^{\frac{1}{\gamma-1}}} \quad (6.20)$$

$$V_{sup} = \frac{\dot{m}}{\rho_{sup} A_e} \quad (6.21)$$

With the supersonic flow properties now known at the exit, the exit pressure can again be compared to that of the backpressure. If the exit pressure calculated is higher than the backpressure the flow is under-expanded. Otherwise, if the pressure is lower than the backpressure, the flow is over-expanded. If the exit pressure is equal to the backpressure, then the flow is isentropic. The ideal situation is for the supersonic exit pressure to equal that of the backpressure. This would be the optimum condition and would result in the maximum thrust, for the specified initial conditions.

Normal shock wave at exit plane of nozzle

If the flow is over-expanded there is a chance that a normal shock might form at the exit plane of the nozzle, or even in the divergent part of the nozzle. To check this, a normal shock wave is assumed at the exit plane of the nozzle.

The Mach number used to calculate the flow properties on the other side of the normal shockwave will be equal to the Mach number calculated for the supersonic flow through the nozzle. The following equations are used to calculate the properties just after the normal shock at the exit plane:

$$T_{norm} = T_{sup} \frac{\left[\left(1 + \frac{\gamma-1}{2} M^2 \right) \left(\frac{2\gamma}{\gamma-1} M^2 - 1 \right) \right]}{\left[\frac{(\gamma+1)^2}{2(\gamma-1)} M^2 \right]} \quad (6.22)$$

$$p_{norm} = p_{sup} \left(\frac{2\gamma}{\gamma+1} M^2 - \frac{(\gamma-1)}{(\gamma+1)} \right) \quad (6.23)$$

$$V_{norm} = \frac{p_{sup} \times V_{sup} \times T_{norm}}{p_{norm} \times T_{sup}} \quad (6.24)$$

If the value of the pressure calculated just after the shock is higher than that of the backpressure, then the normal shock is situated outside of the nozzle. However, if the pressure is lower than that of the back pressure then the normal shock will be situated somewhere inside the nozzle, between the throat and the exit plane of the nozzle. If the pressure calculated is equal to the backpressure, then a normal shock will form at the exit plane of the nozzle.

Normal shock wave inside nozzle

If the pressure calculated for choked flow at the throat and subsonic in the rest of the nozzle is higher than the backpressure, then the flow has to be supersonic in the nozzle. If the pressure just after a normal shockwave at the exit plane of the nozzle is still lower than the backpressure, then a normal shockwave will form somewhere inside of the nozzle, between the throat and the exit plane. The position of the

shockwave has to be determined iteratively, by making use of a bisection method. This method was used by Weyer (2004).

With the known properties of the flow at the throat and a given backpressure, the exit flow properties can be calculated. The position of the shockwave inside the nozzle will be determined by the backpressure. The shockwave will be positioned such that the exit pressure is equal to the backpressure. Figure 6.2 shows a diagram of the methodology used in calculating the position of the shockwave.

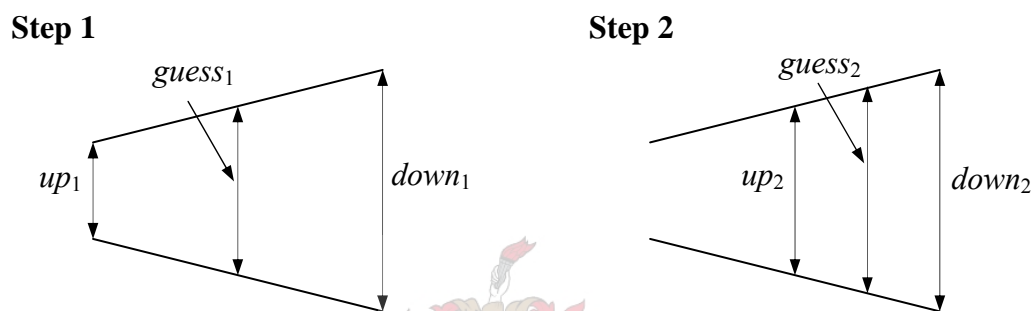


Figure 6.2 Determining position of shockwave

The first step is to guess an area of the nozzle where the shockwave occurs. This first guess ($guess_1$) is half way between the exit and throat of the nozzle. With the area A known equation 6.17 can be used to calculate the Mach number. With the known Mach number the properties just before the shockwave can be calculated, using equations 6.18 to 6.21. These equations are valid, as the flow from the throat up until the shockwave is supersonic. The properties just after the shockwave are calculated using equations 6.22 to 6.24. It is important to note that the stagnation properties just after the shockwave also need to be calculated in order to be able to calculate the flow properties at the nozzle exit. The stagnation properties are calculated using the following equations:

$$T_o = \frac{\left(\frac{V_{norm}^2}{2} + C_p T_{norm} \right)}{C_p} \quad (6.25)$$

$$M_o = \sqrt{\frac{\left(\frac{T_o}{T_{norm}} - 1\right) \times 2}{(\gamma - 1)}} \quad (6.26)$$

$$p_o = p_{norm} \times \left(1 + \frac{\gamma - 1}{2} M_o^2\right)^{\frac{\gamma}{\gamma - 1}} \quad (6.27)$$

$$\rho_o = \frac{p_o}{RT_o} \quad (6.28)$$

where the subscript o refers to the stagnation properties just after the normal shockwave, and the subscript $norm$ refers to the properties of the flow just after the normal shockwave.

Again equation 6.17 is used to calculate the exit Mach number. This time A^* in equation 6.17 is equal to the area where the shockwave is guessed. Therefore A^* is equal to $guess_1$ and A in equation 6.17 is equal to the exit plane area. With the area ratio A/A^* known the exit Mach number can be calculated using the same methodology as that used for the supersonic flow, only now the flow is not supersonic. Therefore the Mach number chosen needs to be less than one for subsonic flow. With the exit Mach number known the exit properties can now be calculated using equations 6.18 to 6.21.

The exit pressure can now be compared to the backpressure. If the pressure calculated is lower than the backpressure, then the shockwave will be situated closer to the throat, than the first guess. In this case the $down_2$ (see Figure 6.2) value is set equal to $guess_1$, and up_2 stays equal to up_1 . The new $guess_2$ is now situated halfway between $down_2$ and up_2 . However if the pressure calculated is higher than the backpressure, then the shockwave will be situated closer to the exit of the nozzle. The same procedure is followed in determining the new position, as in the other case, only now the value of up_2 is set equal to $guess_1$, and this time $down_2$ stays equal to $down_1$. The second case, where the calculated pressure is higher than the backpressure is shown in Figure 6.2, step 2.

This procedure is followed until the position of the shockwave is determined. In our case it was found that after 20 iterations the change in the area was so small that there were no longer any change in the exit pressure calculated.

Subsonic flow – through entire nozzle

If the pressure calculated at the exit plane of the nozzle (for sonic conditions at the throat and subsonic through the rest of the nozzle) is lower than the backpressure, then subsonic conditions exists through the entire nozzle from the throat to the exit plane.

For subsonic flow through the entire nozzle, the exit pressure has to be equal to the backpressure. The rest of the exit flow properties are calculated using the following equations:

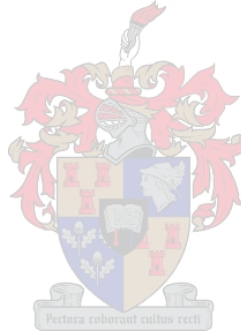
$$P_{sub} = P_B \quad (6.29)$$

$$T_{sub} = T_o \left(\frac{P_{sub}}{P_o} \right)^{\frac{\gamma-1}{\gamma}} \quad (6.30)$$

$$V_{sub} = \sqrt{2C_p(T_o - T_{sub})} \quad (6.31)$$

$$\rho_{sub} = \frac{P_{sub}}{RT_{sub}} \quad (6.32)$$

$$\dot{m}_{sub} = V_{sub} \times \rho_{sub} \times A_{exit} \quad (6.33)$$



Because the flow at the throat is not choked, the flow properties in the throat need to be calculated using the calculated exit flow properties of the flow. It is necessary to make use of an iteration process to calculate the properties in the throat. The first step is to guess a value for the velocity of the flow in the throat. After the throat velocity is chosen the rest of the properties at the exit can be calculated. From the properties calculated a new value for the throat velocity is also calculated. If this newly calculated value for the velocity is lower than the one chosen at the beginning a new, lower value for the throat velocity is chosen. This is done in small increments until the value of the chosen velocity is equal to, or within a certain range of the value calculated. However if the value calculated is higher than the chosen one, a smaller value is chosen and the iteration process is repeated. With a chosen value for the

velocity at the throat V_t , the following equations are used to calculate the properties of the flow in the throat:

$$T_t = T_o - \frac{V_t^2}{2C_p} \quad (6.34)$$

$$p_t = p_o \left(\frac{T_t}{T_o} \right)^{\frac{\gamma}{\gamma-1}} \quad (6.35)$$

$$\rho = \frac{p_t}{RT_t} \quad (6.36)$$

$$V_t = \frac{\dot{m}_{sub}}{\rho A_t} \quad (6.37)$$

This concludes all the different mathematical equations and procedures for the calculation of the flow properties through the nozzle. As a matter of fact the pressure inside the accumulator needs to be higher than the backpressure, for flow to occur through the nozzle. Of course, if the pressure inside the accumulator is below the backpressure there will be flow from outside, through the nozzle, and into the accumulator thereby yielding a negative thrust force. This will not occur in space and is any way very small for typical earth conditions.

With the flow properties known at the exit of the nozzle the thrust force can now be calculated using equation 3.1:

$$F_T = \dot{m}_e V_e + (p_e - p_B) A_e \quad (6.38)$$

where the subscript e refers to the exit properties. The next section will give a detailed logic description of the mathematical procedure described in this section.

6.2 Calculation Procedure Logic Flow Diagram

The diagram below shows the logic used in calculating the exit properties of the flow through the nozzle. The initial conditions of the fluid properties in the accumulator are calculated using a two-phase model (section 6.3) of the butane inside the accumulator. With the stagnation properties of the fluid inside the accumulator known, the fluid

properties through the nozzle were calculated using equations 6.1 to 6.38. With the exit fluid properties known the thrust given by the thruster could be calculated.

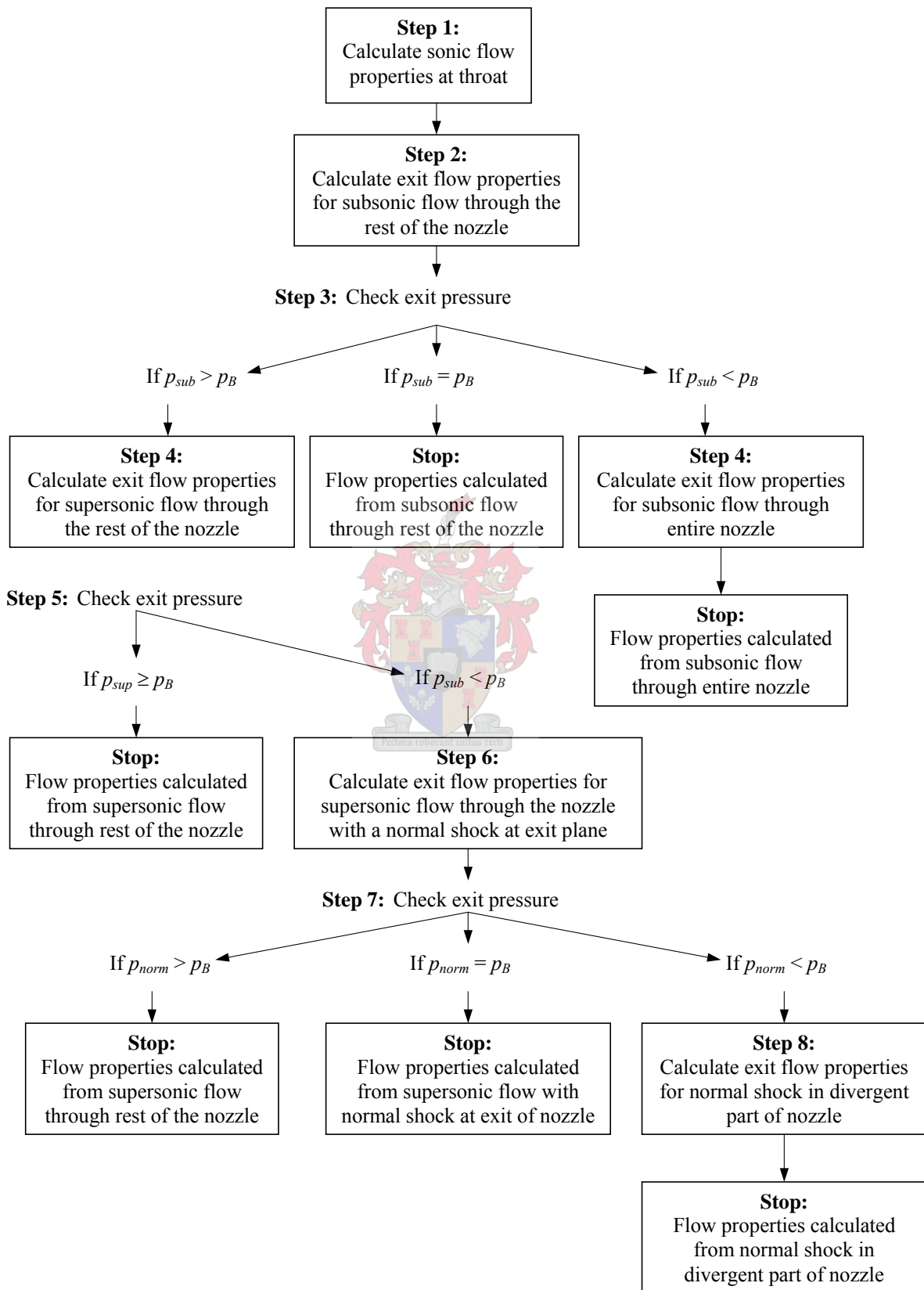


Figure 6.3 Calculation logic flow diagram of gas dynamics model

The first step in Figure 6.3 is to calculate the properties of the fluid at the throat, for sonic conditions. With the properties at the throat known the exit conditions for subsonic flow through the rest of the nozzle are calculated. The exit pressure calculated for these flow conditions can then be compared to the backpressure to which the nozzle exited. If the pressure is equal to the backpressure then there will be sonic flow at the throat with subsonic flow through the rest of the nozzle. However, if the pressure is less than the backpressure then the flow will be subsonic through the entire nozzle. If this is the case then the fluid properties are calculated for subsonic flow through the throat of the nozzle, as well as through the rest of the nozzle. This pressure will then be equal to the backpressure. However, if the pressure calculated in step 2 is greater than the backpressure, then the flow will be supersonic in the divergent part of the nozzle.

If the exit pressure calculated for supersonic flow through the nozzle is equal or greater than the backpressure then the exit properties will be equal to that of the properties calculated for the supersonic flow through the nozzle. However, if this is not the case and the supersonic exit pressure is lower than the backpressure then a normal shockwave is assumed at the exit plane of the nozzle. If the pressure calculated just after the shockwave is higher than the backpressure, then the exit pressure will still be equal to the supersonic exit pressure. If the pressure is equal to the backpressure, then a normal shockwave will exist at the exit plane of the nozzle and the properties of the flow will be equal to those calculated for the normal shockwave at the exit plane. However, if the pressure of the normal shockwave is less than the backpressure then a normal shockwave will occur somewhere inside the divergent part of the nozzle. If this is the case then the position of the normal shockwave must be calculated such that the exit pressure will be equal to the backpressure. If the position of the shockwave has been determined then the exit flow properties for the fluid can also be calculated.

6.3 Two-phase System Model

The fluid inside the accumulator was modelled using a two-phase model. Enough liquid butane was put into the accumulator so that there would be both liquid and

vapour in the accumulator. Before the nozzle valve is opened the fluid in the accumulator is assumed to be in thermodynamic equilibrium. In the accumulator there were two control volumes; one for the liquid butane, and one for the vapour. A basic diagram of the accumulator, nozzle and valve are shown in Figure 6.4.

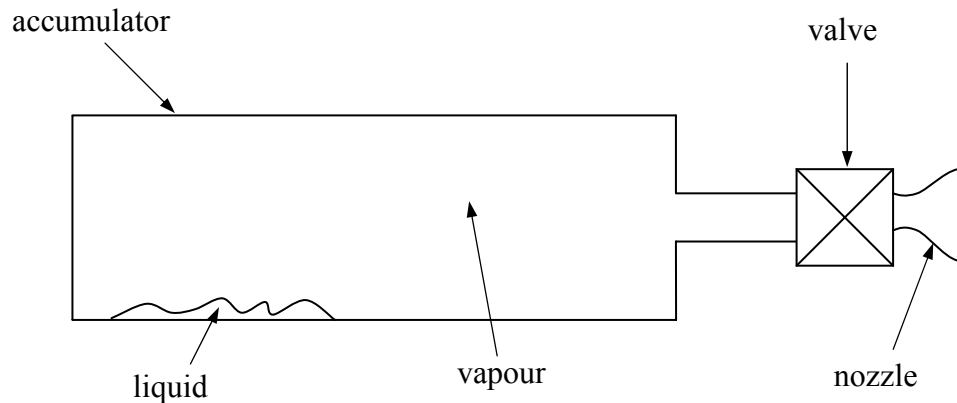


Figure 6.4 Diagram of accumulator - two-phase model

The reason why a two-phase model was developed is to be able to predict the stagnation conditions of the vapour in the accumulator as once the valve is opened the vapour need not be in equilibrium with the liquid. The stagnation properties referred to in the previous section with a subscript o are equal to the vapour properties in the accumulator. For example, the vapour pressure calculated in this section as p_v is equal to the stagnation pressure p_o of the previous section. With the stagnation conditions known the mathematical model described in the previous section can be used to predict the thrust achieved by the thruster system. The initial conditions of the fluid inside of the accumulator, before the nozzle valve is opened, are given. When the nozzle valve is opened, then the transient behaviour of the fluid is modelled using a simple two-phase model as described in the following section.

The thruster system functions more or less as follows: firstly liquid butane is fed into the accumulator from the storage tank. Then the accumulator is heated until a certain temperature is reached in the accumulator. At this point the butane is in thermodynamic equilibrium. Then the nozzle valve is opened, and the butane vapour is exhausted through the nozzle. As soon as the nozzle valve is opened, the pressure in the accumulator starts to drop. This causes the liquid butane inside of the accumulator to start evaporating. Simultaneously heat transfer is taking place between the accumulator wall and both the liquid and vapour control volumes.

6.3.1 Initial conditions

The initial conditions inside the accumulator were calculated using the given information. The information given was:

- mass of liquid butane fed into the accumulator from the storage tank
- temperature and pressure of both the liquid and vapour in the accumulator
- wall temperature of the accumulator
- thermodynamic equilibrium inside the accumulator
- volume of accumulator
- amount of mesh discs placed in accumulator.

The mass of the vapour is calculated using the ideal gas equation, while the liquid mass is calculated by subtracting the vapour mass from the initial mass of butane put into the accumulator.

$$m_v = \frac{p_v V}{RT_v} \quad (6.39)$$

$$m_l = m_{initial} - m_v \quad (6.40)$$

where $m_{initial}$ is the initial mass of butane put into the accumulator and V is the volume of the accumulator.



6.3.2 Vapour control volume

The assumption is made that the volume of the vapour control volume is equal to the total volume of the accumulator. The liquid volume is small and essentially has no effect on the much larger accumulator control volume. Figure 6.5 shows a diagram of the vapour control volume.

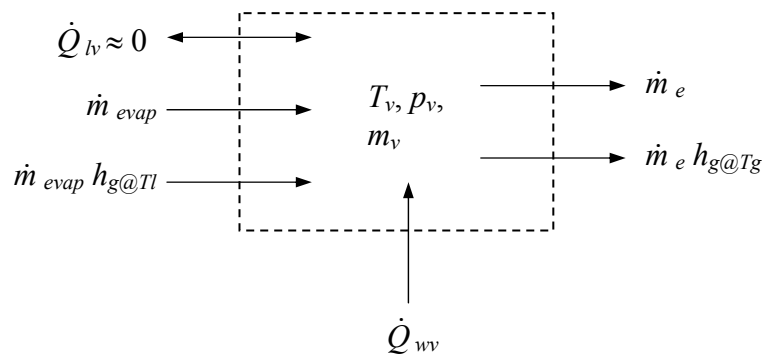


Figure 6.5 Diagram of vapour control volume

The mass of vapour exiting through the nozzle is subtracted from the initial vapour mass in the accumulator to calculate the new mass of the vapour in the accumulator after the first time step. From the continuity equation we get:

$$m_v^{new} = m_v - \Delta t(\dot{m}_e) \quad (6.41)$$

The new stagnation pressure inside of the accumulator is calculated, using the newly calculate vapour mass. The ideal gas equation is used to calculate the new stagnation pressure in the accumulator with the temperature equal to the stagnation temperature of the previous time step.

$$p_v^{new} = \frac{m_v^{new} R T_v}{V} \quad (6.42)$$

With the new stagnation pressure known in the accumulator, the mass evaporated from the liquid because of the pressure difference can be calculated (see section 6.33). The heat transfer from the wall of the accumulator to the vapour is calculated using:

$$\dot{Q}_{wv} = U_{wv} A_{wv} (T_w - T_v) \quad (6.43)$$

where U_{wv} is the heat transfer coefficient between the wall of the accumulator and the vapour, A_{wv} is the contact surface area and T_w is the temperature of the wall. The next step is to recalculate the mass of the vapour by adding the mass that was evaporated from the liquid control volume.

$$m_v^{new-new} = m_v^{new} + \Delta t(\dot{m}_{evap}) \quad (6.44)$$

Next the stagnation temperature of the vapour can be calculated. The energy equation is used to calculate the stagnation temperature of the vapour in the accumulator.

$$T_v^{new} = T_v + \frac{\Delta t}{m_v^{new-new} C_v} (\dot{m}_{evap} h_{g@T_s} + \dot{Q}_{wv} - \dot{m}_e C_p T_v) \quad (6.45)$$

With the new temperature calculated for the vapour, a correlation can be used in order to calculate the enthalpy and specific heat at constant pressure. The correlations used are given in Appendix A. With the calculated specific heat at constant pressure the specific heat at constant volume can be calculated using:

$$C_v^{new} = C_p^{new} - R \quad (6.46)$$

Because it is assumed that the gas behaves as an ideal gas, the specific gas constant R , is assumed to be a constant. A new specific heat ratio can also be calculated using the newly calculated specific heat values.

$$\gamma = \frac{C_p^{new}}{C_v^{new}} \quad (6.47)$$

Lastly the stagnation pressure of the vapour in the accumulator with the newly calculated values for the mass and temperature is recalculated. Again the ideal gas equation of state is used to calculate the pressure in the accumulator.

$$p_v^{new-new} = \frac{m_v^{new-new} RT_v^{new}}{V} \quad (6.48)$$

6.3.3 Liquid control volume

When the liquid and vapour of the fluid is in thermodynamic equilibrium no heat transfer or mass transfer will take place between the two phases. Initially, before the nozzle valve is opened, this is the case inside of the accumulator. However, as soon as the nozzle valve is opened, the pressure in the accumulator starts to drop. As the pressure in the accumulator drops liquid evaporates in accordance with (Mills, 1999):

$$\dot{m}_{evap} = A_{lv} \frac{2\sigma}{2 - \sigma} \left(\frac{p_l}{\sqrt{2\pi RT_l}} - \frac{p_v^{new}}{\sqrt{2\pi RT_v}} \right) \quad (6.49)$$

where A_{lv} = surface area of liquid-vapour contact area

σ = condensation coefficient

$p_l = p_{sat@T_l}$, saturation vapour pressure corresponding to liquid surface temperature

T_l = temperature of liquid surface

p_v^{new} = pressure of vapour adjacent to the liquid surface

T_v = temperature of vapour adjacent to the liquid surface

As the liquid evaporates its temperature drops, unless heat is transferred into it to make up for the enthalpy of evaporation. Note that a negative mass transfer will occur if the pressure of the vapour adjacent to the liquid is higher than the saturation pressure of the liquid, or the temperature of the vapour is a lot less than the

temperature of the liquid. This will mean that instead of the liquid evaporating, vapour condensation will take place.

Figure 6.6 shows the liquid control volume and all the mass and energy transfers affecting the liquid control volume. The contact area between the liquid and the accumulator was taken as 0.0004 m^2 . The influence of the liquid surface area is discussed in more detail in section 7.4.

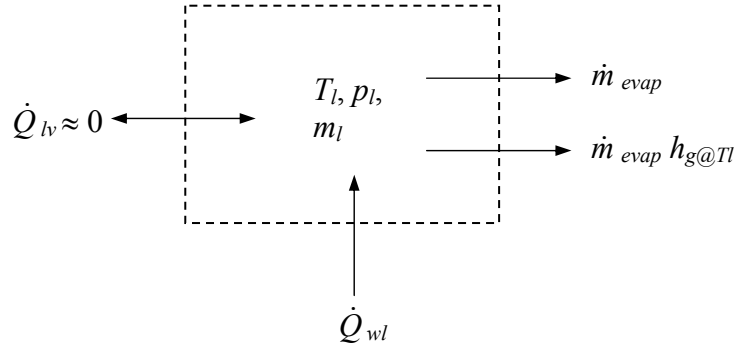


Figure 6.6 Diagram of liquid control volume

To calculate the mass of liquid evaporated equation 6.49 is used. After the mass of liquid is determined the heat transfer from the accumulator wall to the liquid is calculated.

$$\dot{Q}_{wl} = U_{wl} A_{lv} (T_w - T_l) \quad (6.50)$$

where U_{wl} is the heat transfer coefficient between the wall and the liquid. The area A_{lv} used is the same area used in equation 6.49 to calculate the evaporating liquid. The temperature of the liquid is assumed to be the same as the temperature of the liquid surface T_l used in equation 6.49.

Since the mass evaporated is already calculated, the new mass of the liquid can also be calculated by subtracting the evaporated mass from the initial mass of the liquid.

$$m_l^{new} = m_l - \Delta t (\dot{m}_{evap}) \quad (6.51)$$

Now the new temperature of the liquid can be calculated. From the energy equation we get:

$$T_l^{new} = T_l + \frac{\Delta t}{m_l^{new} C_{v,l}} (\dot{Q}_{wl} - \dot{m}_{evap} h_{g@T_s}) \quad (6.52)$$

The correlation given in Appendix A was used to calculate the new saturation pressure of the liquid, corresponding to the newly calculated liquid temperature.

6.3.4 Mesh in accumulator

Copper mesh was placed in the accumulator to improve the heat transfer to the butane vapour. Mesh with 40 holes per linear 25.4 mm and a wire thickness of 0.26 mm was used. The mesh was cut into round discs and stacked in the accumulator. Figure 6.7 shows the accumulator with the mesh inside.

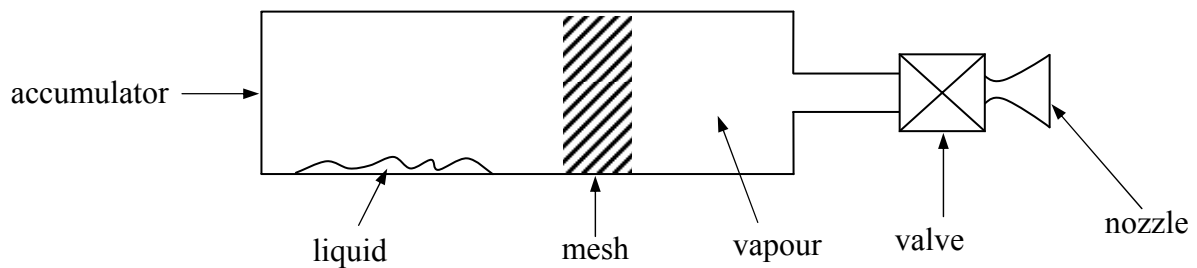


Figure 6.7 Diagram of accumulator with mesh

An estimation of the area over which the heat transfer would take place in the mesh had to be made. Each of the discs that were placed in the accumulator weighed 3 grams. So the length of the copper wire per disc can be calculated using:

$$L_w = \frac{m_d}{\rho_c A_w} \quad (6.53)$$

where m_d is the mass of copper per disc, ρ_c is the density of the copper, A_w is the area of the wire and d_w is the diameter of the wire, where:

$$A_w = \frac{\pi d_w^2}{4} \quad (6.54)$$

Knowing the length of the wire per disc the heat transfer area can now be calculated:

$$A_{ht} = L_w \pi d_w N_d \quad (6.55)$$

where N_d is the number of mesh discs placed in the accumulator.

In order to determine the velocity of the fluid through the mesh the area through which it could flow had to be determined. By calculating the size of each hole in the mesh and then multiplying it by the number of holes in each disc the area through which the fluid can flow is determined. The velocity through the mesh can then be calculated using:

$$V_m = \frac{\dot{m}_e}{\rho_v A_h} \quad (6.56)$$

where \dot{m}_e is the mass flow of the vapour butane exiting the nozzle, ρ_o is the density of the butane in the accumulator and A_h is the total area through which the butane can flow in each mesh disc. With the velocity of the fluid through the mesh known the Reynolds number can be calculated using:

$$Re = \frac{V_m d_w \rho_v}{\mu_v} \quad (6.57)$$

where μ_v is the dynamic viscosity of the butane vapour. It was found that the Reynolds number was very low and therefore the heat transfer coefficient could be estimated using:

$$U_m = \frac{k_v}{\frac{1}{3} L_h} \quad (6.58)$$

where k_v is the thermal conductivity of the butane vapour and L_h is the length of the hole in the mesh. Knowing the thickness of the wire (0.26 mm), as well as the mesh number (40 mesh) the length of the hole L_h is determined.

With the heat transfer coefficient known, as well as the heat transfer area, the heat transfer from the mesh to the butane vapour can be calculated.

$$\dot{Q}_{mv} = U_m A_{ht} (T_m - T_v) \quad (6.59)$$

where T_m is the temperature of the mesh and T_v the temperature of the butane vapour inside of the accumulator.

Now the energy equation is used to determine the new temperature of the mesh.

$$T_m^{new} = T_m - \frac{\Delta t}{m_d N_d C_{p,c}} \dot{Q}_{mv} \quad (6.60)$$

The new temperature of the butane vapour is calculated using equation 6.45, only now the heat transfer from the mesh to the butane vapour is added. So, equation 6.45 now becomes:

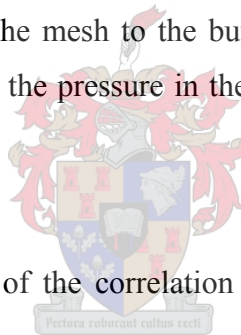
$$T_v^{new} = T_v + \frac{\Delta t}{m_v^{new-new} C_v} (\dot{m}_{evap} h_{g@T_s} + \dot{Q}_{wv} + \dot{Q}_{mv} - \dot{m}_e C_p T_v) \quad (6.61)$$

The results that were obtained from the two-phase model with the mesh inside of the accumulator are discussed in section 7. It was found that the heat transfer from the mesh to the butane vapour was overestimated. In order to get a better estimate of the pressure inside of the accumulator the heat transfer coefficient and heat transfer areas were adjusted. These were both initial estimates and are therefore adjusted to get a better estimate of the heat transfer. Because the wires of the mesh are folded over each other, in order to form the mesh, the contact area over which the heat transfer takes place can be up to 50 % less than was initially thought. The heat transfer coefficient is also very difficult to estimate, as it is not possible to know the exact mass flow of the fluid through the mesh inside of the accumulator.

It was decided to incorporate a heat transfer correlation coefficient to take into account the uncertainty of the contact surface area, as well as the uncertainty of the heat transfer coefficient. A new variable b was incorporated into equation 6.59. Thereby the heat transfer from the mesh to the butane vapour could be adjusted, in order to get a better estimate for the pressure in the accumulator. Equation 6.59 then becomes:

$$\dot{Q}_{mv} = bU_m A_{ht} (T_m - T_v) \quad (6.62)$$

The results for different values of the correlation coefficient, b is given in section 7.2.3.



6.4 Logic of Mathematical Model for Thruster System

The initial conditions of the fluid properties in the accumulator are given. The stagnation pressure and temperature of the vapour inside the accumulator is used in order to calculate the flow of the butane through the nozzle using idealized gas dynamics. A transient two-phase model making use of control volumes are used to simulate the behaviour of the butane in the accumulator. As soon as the nozzle valve is opened butane vapour exits through the nozzle, the pressure inside of the accumulator starts to drop and liquid butane starts to evaporate. This was all modelled mathematically by making use of the equations given in sections 6.1 and 6.3. The steps are set out below that were used in the logic of the computer program.

Step 1: Calculate initial conditions inside of the accumulator.

Step 2: Calculate mass flow through nozzle using idealized gas dynamics for a small time step.

Step 3: Calculate new mass of vapour in accumulator (vapour control volume).

Step 4: Calculate new stagnation pressure inside of the accumulator (vapour control volume).

Step 5: Calculate mass evaporated from liquid butane in accumulator (liquid control volume).

Step 6: Calculate energy transfer from accumulator wall to both the vapour and liquid (vapour and liquid control volumes).

Step 7: Calculate energy transfer from copper mesh to the vapour (vapour control volume).

Step 8: Calculate the new mass of the vapour by adding the evaporated mass of the liquid (vapour control volume).

Step 9: Calculate the new mass of the liquid by subtracting the evaporated mass from the liquid mass (liquid control volume).

Step 10: Calculate the new stagnation temperature of the vapour (vapour control volume).

Step 11: Calculate the new saturation pressure of the liquid using a correlation (liquid control volume).

Step 12: Calculate the new enthalpy and specific heat at constant pressure of the vapour using a correlation (vapour control volume).

Step 13: Calculate the specific heat at constant volume as well as the specific heat ratio of the vapour (vapour control volume).

Step 14: Calculate new stagnation pressure of the vapour inside of the accumulator (vapour control volume).

Step 15: Go back to step 2, and repeat all the steps for the next time step.

This procedure is followed for a specified number of time steps and only as long as the pressure inside of the accumulator is higher than the backpressure.

7 Results

In this section the observations and measurements obtained from the experimental testing and theoretical modelling analyses of the system are given and discussed. The theoretical and experimental results are also compared.

7.1 Experimental Results

Before the experimental tests were conducted, certain initial conditions under which the thruster would operate had to be decided upon. A first set of tests (using nozzle-1) was done with the accumulator tank at a temperature of about 25 °C. These tests were conducted to test the influence of the amount of copper mesh in the accumulator. A second set of testing was done using a different nozzle (nozzle-2) with no mesh in the accumulator. All of the above tests were conducted at an atmospheric pressure of 100 000 Pa. A third (and final) set of tests was conducted in a vacuum chamber, at a pressure of 20 Pa. Although no mesh was used in the accumulator both nozzle-1 and nozzle-2 were tested. Both nozzle-1 and nozzle-2 had a throat diameter of 1 mm. Nozzle-1 had a exit diameter of 5 mm and nozzle-2 had a exit diameter of 1.6 mm.

7.1.1 Tests conducted at 25 °C

Thermocouples were placed in the three accumulator temperature sensor pockets (Figure 4.2) to determine the temperature of the fluid in the accumulator. Initially it was thought that the temperatures that were measured by the thermocouples were indeed the temperature of the butane in the accumulator. It was found however that this was not necessarily the case. The temperatures measured took a lot longer to reach equilibrium. As is discussed in section 5.4, the thermocouples were placed in stainless steel tubes in the accumulator. These stainless steel tubes were heated with a combination of radiation from the electrical heater in the accumulator and the conduction from the butane vapour. Extreme caution had thus to be taken in interpreting these temperature readings. The temperatures did become stable, but only after about 6 to 8 hours. So, the temperature in the accumulator was set equal to the saturation temperature of the butane corresponding to the saturation of the pressure in the accumulator for the theoretical model.

As discussed in section 6.3 the accumulator was charged with a measured amount of butane. This was done so that the I_{sp} of the thruster system could be determined. If it is known how much butane is exhausted, and how much thrust was achieved, the I_{sp} value of the system can be calculated with:

$$I_{sp} = \frac{\int F_T dt}{g \cdot m} \quad (7.1)$$

where F_T is the thrust achieved, g is equal to the gravitational constant and m is the mass of butane exhausted. Four different ways of exhausting all of the butane were tested.

Method 1 – opening the nozzle valve until the pressure in the accumulator is equal to the backpressure and there is no more pressure recovery observed.

Method 2 – opening the nozzle valve for 2 seconds, closing it for 10 seconds and then opening it for two seconds again. This is repeated until all the butane is exhausted.

Method 3 – opening the nozzle valve for 2 seconds, closing it for 50 seconds and then opening it for two seconds again. This is repeated until all the butane is exhausted.

Method 4 – opening the nozzle valve for 5 seconds, closing it for 50 seconds and then opening it for two seconds again. This is repeated until all the butane is exhausted.

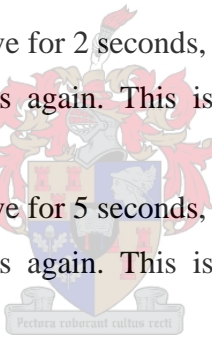


Figure 7.1 shows both pressure readings of the butane inside of the accumulator while Figure 7.2 shows the thrust achieved for one such a single burst (method 1), with 20 discs of copper mesh placed inside the accumulator. It can be seen that both pressure readings coincide with each other.

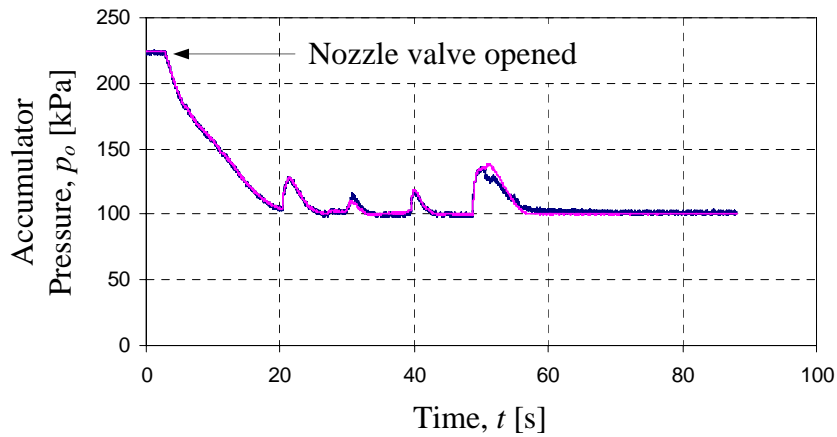


Figure 7.1 Pressure curve for method 1 of exhausting 13 ml initial charge with 20 mesh discs in accumulator for nozzle-1

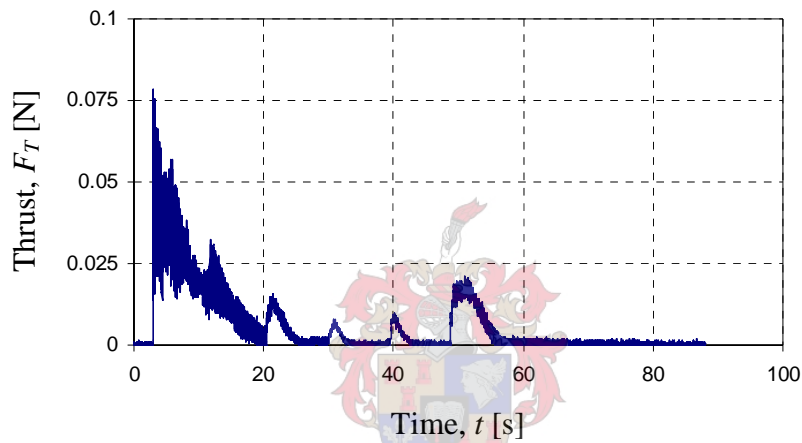


Figure 7.2 Thrust for method 1 of exhausting 13 ml initial charge with 20 mesh discs in accumulator for nozzle-1

In Figure 7.1 it is seen that after the initial drop in pressure, a number of smaller pressure curves are noticed while the nozzle valve is open. These occur because of the liquid butane in the accumulator evaporating. The liquid evaporates because the saturation pressure of the liquid at the liquid temperature is higher than the vapour pressure inside of the accumulator. It stops evaporating again because as the butane evaporates the temperature of the liquid butane decreases and thereby reducing the boiling point. However, there is continual heat transfer from the wall of the accumulator to the liquid and thus the liquid temperature and saturation pressure is increased. The reason why only the pressure and thrust curves for the case where 20 mesh discs were used are given, is because the pressure and thrust curves for the different amounts of copper mesh were very similar. The main difference was that the more mesh was placed in the accumulator the greater the heat capacity and the slower

the pressure dropped. Because the pressure drop in the accumulator was slower, the total thrust achieved with mesh in the accumulator was also higher.

Table 7.1 shows the comparison of the total thrust achieved using method 1 for exhausting the butane, with different number of mesh discs in the accumulator for nozzle-1.

Table 7.1 Method-1 of exhausting 13 ml initial charge for nozzle-1

	Start up Temperature [°C]	Start up Pressure [kPa]	$\int_0^{\infty} F_T dt$ [Ns]	I_{sp} [s]
No mesh	23.0	229.0	0.326	4.5
5 mesh	22.9	228.4	0.341	7.4
20 mesh	22.3	224.1	0.498	6.9
50 mesh	18.0	195.0	0.446	6.2
80 mesh	17.2	190.0	0.462	6.4
80 mesh	20.2	209.5	0.485	6.7

Figure 7.3 shows the pressure curve using method 2 for exhausting a charge of 13 ml of butane. The valve was opened for a 2 second burst and then closed for a 50 second period. The pressure curve for only the first four bursts are shown. Figure 7.4 shows the thrust curve for the first burst. Figures 7.3 and 7.4 are for an experiment conducted with no mesh in the accumulator.

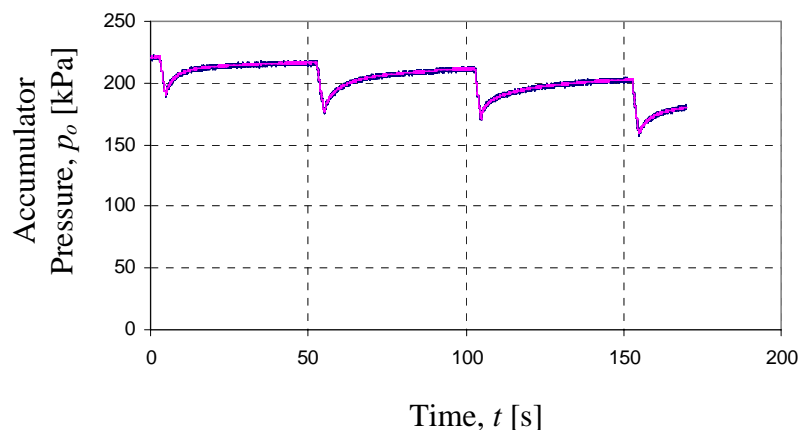


Figure 7.3 Pressure curve for method 2 of exhausting 13 ml initial charge with 0 mesh discs in accumulator for nozzle-1

Figure 7.3 shows the pressure measured with the two pressure transducers. These two pressure curves lie on top of each other.

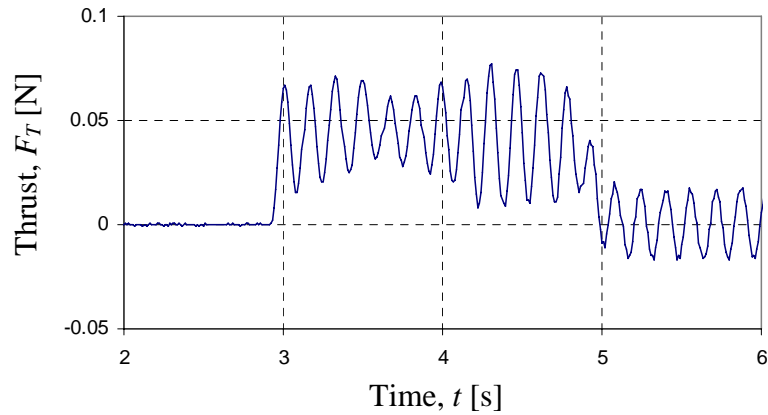


Figure 7.4 First thrust curve for method 2 of exhausting 13 ml initial charge with 0 mesh discs in accumulator for nozzle-1

From Figure 7.4 the 6 Hz fundamental mode of vibration of the thrust sensor can be seen. From this we can see that the response of the sensor is fast enough to accurately capture 1 to 2 second thrust bursts because its period is $\frac{1}{6} \approx 0.17$ [s].

Table 7.2 shows the results using method 2 for exhausting the butane. Table 7.3 shows the results using method 3 of exhausting of the butane while Table 7.4 shows the results using method 4 of exhausting of the butane. From these tables it can be seen that the highest average I_{sp} for the different number of mesh discs is achieved when using method 3. When using method 3 the nozzle valve is closed for a longer period of time which gives more time for heat transfer to take place from the mesh to the butane vapour in the accumulator.

Table 7.2 Method 2 of exhausting 13 ml initial charge for nozzle-1

	Start up Temperature (°C)	Start up Pressure (kPa)	$\int_0^{\infty} F_T dt$ [Ns]	I_{sp} [s]
No mesh	22.9	228.2	0.365	5.0
5 mesh	22.8	228.0	0.407	5.6
20 mesh	22.5	225.6	0.583	8.1
50 mesh	18.0	195.3	0.515	7.1
80 mesh	16.8	187.5	0.573	7.9
80 mesh	20.5	211.5	0.566	7.8

Table 7.3 Method 3 of exhausting 13 ml initial charge for nozzle-1

	Start up Temperature (°C)	Start up Pressure (kPa)	$\int_0^{\infty} F_T dt$ [Ns]	I_{sp} [s]
No mesh	23.1	230.0	0.382	5.3
5 mesh	22.4	224.6	0.414	5.7
20 mesh	22.2	223.5	0.62	8.6
50 mesh	18.5	198.0	0.553	7.6
80 mesh	16.8	187.5	0.615	8.5
80 mesh	20.4	211.0	0.605	8.4

Table 7.4 Method 4 of exhausting 13 ml initial charge for nozzle-1

	Start up Temperature (°C)	Start up Pressure (kPa)	$\int_0^{\infty} F_T dt$ [Ns]	I_{sp} [s]
No mesh	22.3	224.4	0.365	5.0
5 mesh	22.9	228.6	0.489	6.8
20 mesh	22.6	225.9	0.549	7.6
50 mesh	18.0	194.7	0.515	7.1
80 mesh	17.0	188.5	0.515	7.1
80 mesh	20.3	210.0	0.595	8.2

7.1.2 Different nozzle tests

The nozzle (nozzle-1) that was used in the tests conducted at 25 °C to test the influence of the amount of mesh in the accumulator had shockwaves in the nozzle. The formation of shockwaves is discussed in more detail in section 6.1. A second nozzle was designed that would allow for supersonic flow to exist throughout the nozzle. Although shockwaves did form in this nozzle (nozzle-2) as the pressure continually decreased in the accumulator, there were however no shockwaves present at the start of the tests. Nozzle-1 used in the tests conducted at 25 °C had a throat diameter of 1 mm and an exit diameter of about 5 mm. Nozzle-2 also had a throat diameter of 1 mm, but its exit diameter was only 1.6 mm. Figure 7.5 and Figure 7.6 show the pressure and thrust curves for the two different nozzles. In these tests that were conducted there was no mesh put in the accumulator. To compare the two nozzles the nozzle valve was opened for 5 seconds before closing it again. The valve was only opened and closed once.

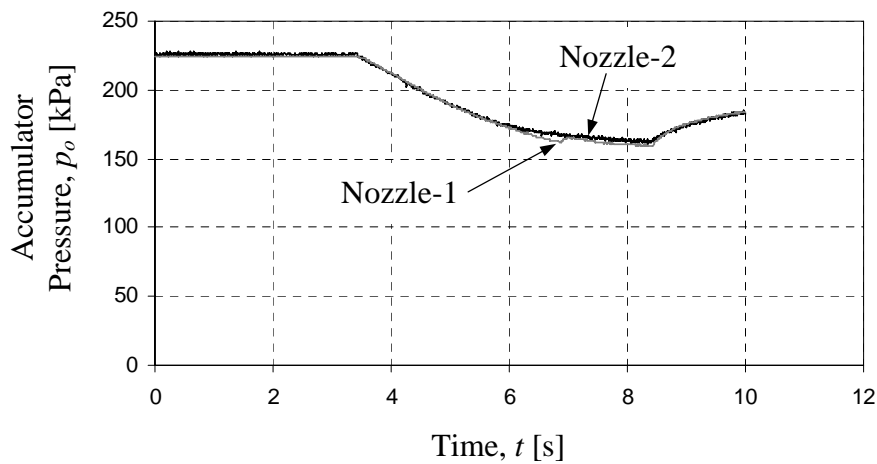


Figure 7.5 Pressure curves for the two nozzles at atmospheric conditions

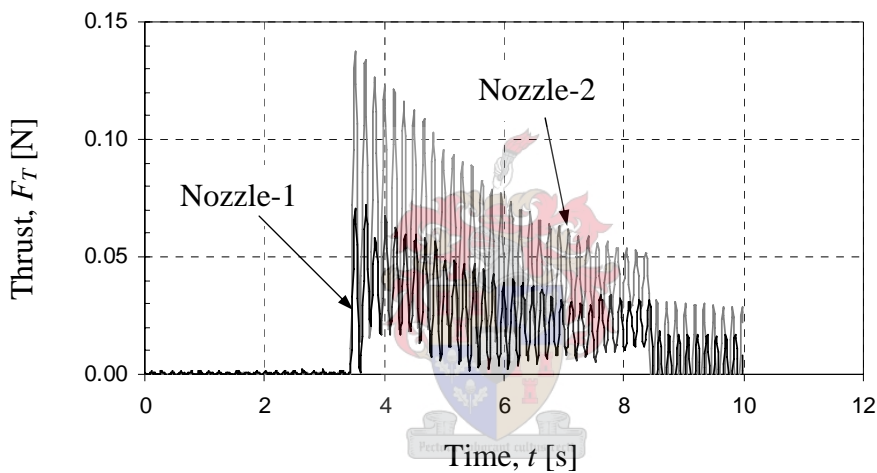


Figure 7.6 Thrust curves for the two nozzles at atmospheric conditions

From Figure 7.5 it can be seen that the two pressure curves coincide. This is because the throats of the two nozzles are the same size; both have a 1 mm diameter. If the flow in the throat is choked, which is the case, then the mass flow is governed only by the size of the throat. In other words, what is happening on the inside of the accumulator is not affected by what is happening to the flow after the throat. So the pressure curves of the fluid in the accumulator is expected to follow the same path for the two different nozzles.

However, if one looks at the thrust curves of the two different nozzles it can be seen that they are very different from each other. The total thrust for the two nozzles are:

$$\text{Nozzle-1} - \int_{3.3}^{8.3} F_T dt = 0.136 \text{ [N.s]}$$

$$\text{Nozzle-2} - \int_{3.3}^{8.3} F_T dt = 0.26 \text{ [N.s]}$$

The total thrust for nozzle-2 shows a 91 % increase in the total thrust over the five-second burst, compared to the total thrust achieved by nozzle-1. The peak thrust achieved with nozzle-2 was about 75.75 mN while the peak thrust for nozzle-1 was about 39.23 mN. This showed an increase of about 93 % in the peak thrust achieved by nozzle-2 compared to that achieved by nozzle-1.

7.1.3 Vacuum chamber testing

Tests were conducted in a vacuum chamber to thereby simulate conditions where the backpressure is nearly zero. In the vacuum chamber the pressure was equal to 20 Pa. Again there was no mesh in the accumulator for these tests. Nozzle-1 and nozzle-2 were tested, and the results compared with the tests conducted under atmospheric conditions. The pressure in the vacuum chamber of 20 Pa was low enough that no shockwaves would form in either of the two nozzles. Figure 7.7 shows the comparison between the pressure curves for the vacuum test compared to the test done under atmospheric conditions for nozzle-1 and nozzle-2. The thrust curves for nozzle-1 and nozzle-2 are shown in Figure 7.8.

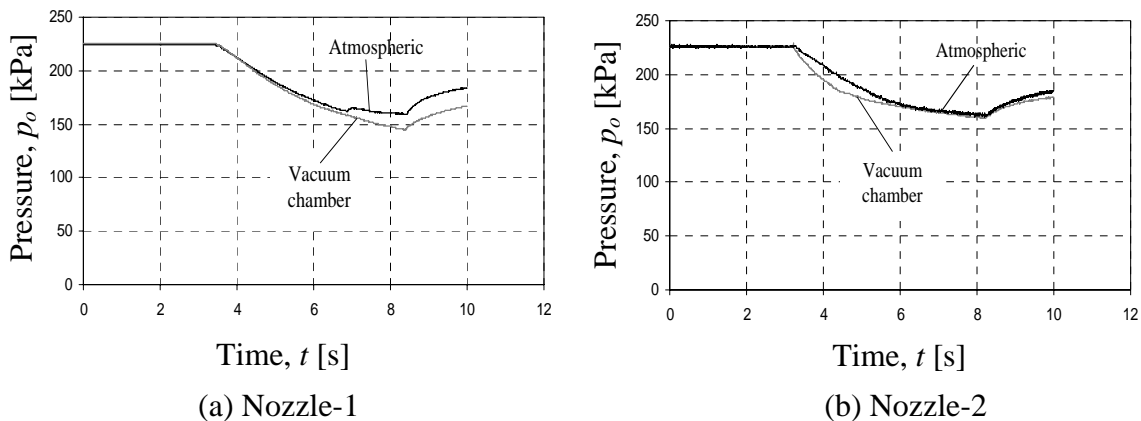


Figure 7.7 Comparison between vacuum chamber and atmospheric tests

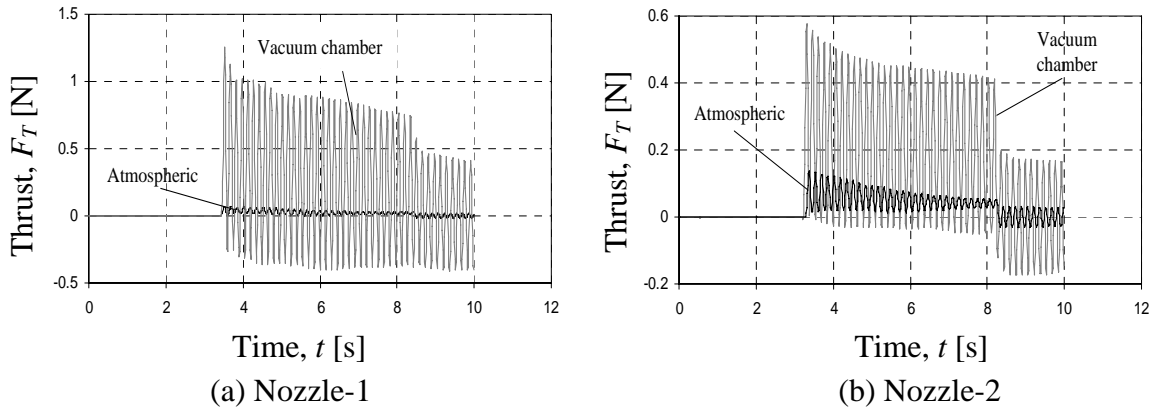


Figure 7.8 Comparison between vacuum chamber and atmospheric conditions tests

From Figure 7.7 it can be seen that the pressure curves lie very close to each other. The reason for the slight discrepancies between the pressure curves is due to the inconsistent and unpredictable evaporation of the liquid butane. However, Figure 7.8 shows that the thrust curves are very different from each other. The peak thrusts and total thrusts for the 5 second bursts are displayed in Table 7.5.

Table 7.5 Thrust achieved at vacuum and atmospheric conditions for the two different nozzles with no mesh in the accumulator

	Start up Pressure (kPa)	Start up Temperature ($^{\circ}$ C)	Peak Thrust (mN)	$\int_{3.8}^{8.3} F_T dt$ [Ns]
Nozzle-1 (Atmospheric)	224.4	22.3	39.23	0.136
Nozzle-1 (Vacuum)	225.6	22.5	495.00	1.39
Nozzle-2 (Atmospheric)	226.2	22.7	75.75	0.26
Nozzle-2 (Vacuum)	226.1	22.7	288.00	1.08

From Table 7.5 it can be seen that the peak thrust achieved under vacuum conditions for nozzle-1 is almost 13 times better than the thrust achieved under atmospheric conditions. That is more than a 1000 % increase in the peak thrust achieved with the same nozzle. Also, the total thrust achieved during the 5 second bursts, show an increase of more than 10 times. That is a 920 % increase in the total thrust achieved with the same nozzle. The reason for the increase in thrust is due to the fact that in the vacuum chamber there are no shockwaves present inside the nozzle. The reason for the shockwaves in the nozzle is discussed in more detail in section 6.3. Basically it comes down to the fact that as the flow is accelerated the pressure drops. However, the exit pressure needs to be equal to the backpressure, to which the flow is

exhausted. If the pressure drops too low, shockwaves develop in the nozzle, to compensate for the low pressure, and this increases the pressure again so that the pressure at the exit plane of the nozzle is equal to the backpressure. In the case of the vacuum chamber tests, the backpressure was so low that the flow could exit at a very high velocity, without shockwaves being present in the nozzle because the backpressure was almost equal to zero.

For nozzle-2 the increase in the peak thrust and total thrust over the 5 second thrust period were not so significant. With nozzle-2 the increase in the peak thrust was less than 4 times, which meant a 280 % increase in the peak thrust. The total thrust force over the 5 second thrust period was just over 4 times more, with a 315 % increase in the total thrust. The reason why the increase of the thrust in nozzle-2 is so much less than the increase observed in nozzle-1 is because nozzle-2 was designed specifically to perform better under atmospheric conditions. So even though nozzle-2 experienced an increase in the thrust, it was not as significant as the thrust increase of nozzle-1.

The total thrust achieved using nozzle-1 with a 13 ml liquid butane charge in the vacuum chamber was 4.88 Ns. This resulted in an I_{sp} of 67.5 seconds. From Table 7.4 it can be seen that total thrust achieved using nozzle-1 under atmospheric conditions was 0.365 Ns, which resulted in an I_{sp} of 5 seconds. This is an increase of more than 1200 % in the I_{sp} of the system under vacuum conditions.

From Table 7.5 it can be seen that nozzle-2 is suited more for conditions where the thruster exhausts to a higher backpressure and nozzle-1 is more suited to conditions where the backpressure is a lot lower. This clearly shows the importance of using the correct nozzle, for the conditions under which the nozzle would operate. The nozzle size is discussed in more detail in section 8.2.

7.2 Theoretical Results

From the results obtained it can be seen that there are many parameters affecting the thruster system performance. However, the experimental set-up was not only used to see the effect of placing copper mesh in the accumulator and using different nozzle diameters had on the thruster system, it was also used to validate the analytical model. An analytical model was developed to model both the complex two-phase behaviour

of the liquid-vapour butane in the accumulator, as well as the flow of the fluid as it exited through the nozzle using idealized gas dynamics.

The analytical model was developed such that it can predict the performance of the thruster system, given the initial conditions of the thruster system. These initial conditions include the temperature and pressure of the butane vapour in the accumulator, as well as the backpressure to which the fluid was exited. The throat and exit diameter of the nozzle also needs to be specified, as well as the number of copper mesh discs placed in the accumulator.

7.2.1 Atmospheric condition

The first case where the analytical model was compared to the results obtained experimentally, was for the case with no mesh in the accumulator. The throat and exit diameters of nozzle-1 were used and the backpressure was set equal to the atmospheric pressure. Also, it was decided to look at the case where the nozzle valve was opened for 5 seconds before closing it again. In Figure 7.9 the comparison between the theoretical pressure predicted and the experimental pressure obtained in the accumulator can be seen. Figure 7.10 shows the comparison between the thrust predicted and the thrust measured experimentally.

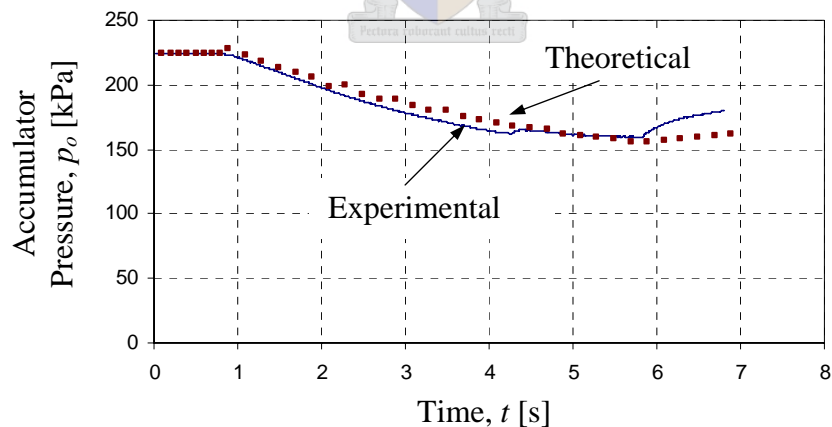


Figure 7.9 Comparison between experimental and theoretical pressure results
(nozzle-1 and backpressure = 100 kPa)

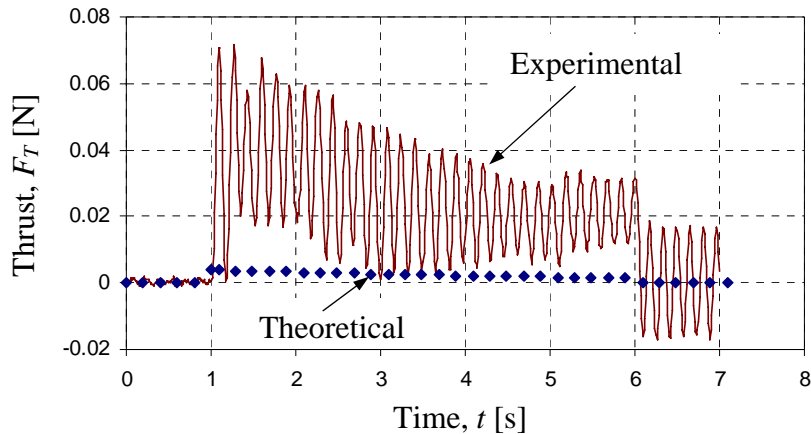


Figure 7.10 Comparison between experimental and theoretical thrust results (nozzle-1 and backpressure = 100 kPa)

From Figure 7.9 it can be seen that the pressures between the theoretical model and that of the pressure determined experimentally in the accumulator compare very well with each other. Again there are a few minor differences as the pressure drops lower. These differences are attributed to the unpredictable increase in the evaporation of the liquid butane inside of the accumulator.

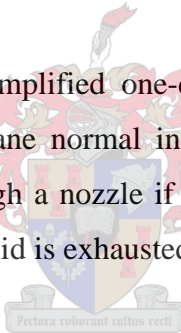
In Figure 7.10 it can be seen that the experimental and theoretical results for the system do not compare well. As is discussed in the section 7.1 above, shockwaves formed continuously in nozzle-1 right from the time that the nozzle valve was opened. One of the possible reasons for the big difference between the results can be that the thrust was measured inaccurately. This option was looked at in great detail, by recalibrating the thrust sensor, and doing further tests with other nozzles, as well as under vacuum conditions. It was found that the thrust sensor was calibrated correctly and was indeed measuring correctly.

Another possibility was that the sensor was measuring the thrust correctly, but that the theoretical model was unable to predict the thrust correctly. It was reasonably certain that the inlet conditions were calculated correctly, because of the good comparison between the pressure measured experimentally and that determined theoretically. Therefore it was assumed that the position of the shockwave in the nozzle was determined inaccurately. To see whether the analytical model could indeed calculate the position of a shockwave accurately in a nozzle, the model was used to determine

the position of shockwaves in different nozzles using examples out of the literature. Unfortunately the examples out of the literature only made use of air as a fluid medium, however the validity of the analytical model could still be determined using these examples. The results are given in Appendix B. The results show that the analytical model was able to calculate the position of a shockwave accurately inside a nozzle.

According to Hill et al. (1992) a shock is strongly affected by interacting with the nozzle boundary layer. The shock can separate the boundary layer and set up a complex flow disturbance within the nozzle, which in turn will greatly affect the shock configuration. It is also stated that the shock inside a nozzle with high exit plane pressure is definitely not plane normal. The simple model that was used in order to calculate the flow through the nozzle, assumed that if a shock formed in the nozzle that it was plane normal. According to Hill this is not necessarily the case.

Therefore it is shown that the simplified one-dimensional theoretical model, that assumes a shockwave to form plane normal inside of a nozzle, cannot accurately predict the thrust developed through a nozzle if shockwaves form continuously in a nozzle right from the time that a fluid is exhausted through the nozzle.



The next case that was looked at was the case where nozzle-2 was used instead of nozzle-1. The rest of the experimental set-up was identical to that used in the previous set-up. The backpressure was equal to the atmospheric pressure, there was no mesh in the accumulator and the nozzle valve was opened for 5 seconds before it was closed again. Figure 7.11 shows the comparison between the pressures for the experimental results and that obtained from the theoretical results. Figure 7.12 shows the thrust achieved theoretically compared to the thrust measured experimentally.

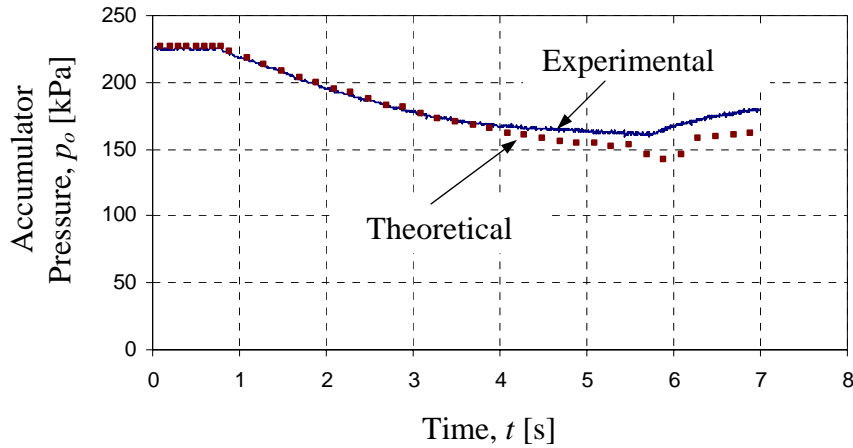


Figure 7.11 Comparison between experimental and theoretical pressure results
(nozzle-2 and backpressure = 100 kPa)

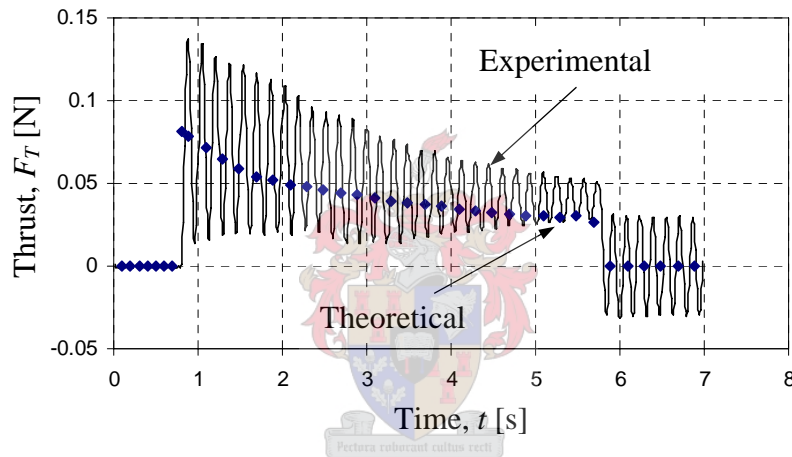


Figure 7.12 Comparison between experimental and theoretical thrust achieved
(nozzle-2 and backpressure = 100 kPa)

In this case, where nozzle-2 was used, the difference between the theoretical pressure calculated and the experimentally determined pressure, is bigger than in the case where nozzle-1 was used. Again this difference is attributed to the unpredictability of the evaporation of the liquid butane inside the accumulator. However, the theoretically predicted pressure still follows the experimental pressure very accurately.

If one looks at the thrust achieved experimentally and the thrust curve predicted theoretically using nozzle-2, the theoretical thrust compares a lot better with the experimental thrust than was the case when nozzle-1 was modelled. The reason that the thrust is predicted more accurately is because there are no shockwaves in the

nozzle as soon as the nozzle valve is opened. This was not the case for nozzle-1, whereas soon as the nozzle valve was opened shockwaves formed inside of the nozzle. Shockwaves do start to form in nozzle-2 after 1 second of firing.

The results obtained from the experimental measurements and the theoretical modelling of the thruster system is given in Table 7.6 and Table 7.7. The results include both the modelling of the thrust under atmospheric conditions as well as the thrust results from the vacuum chamber.

7.2.2 Vacuum conditions

The experimental set-up and instrumentation in the vacuum chamber was very much the same as that for the tests conducted under atmospheric conditions. There was no mesh in the accumulator, both the nozzles were tested, and the nozzle valve was opened for a 5 second period to exhaust the butane before it was closed again. In the vacuum chamber the backpressure was equal to 20 Pa.

Both nozzle-1 and nozzle-2 were modelled and compared to the experimental results. Figure 7.13 shows the pressures obtained from the experimental results compared to the theoretical results using both nozzle-1 and nozzle-2. Figure 7.14 shows the thrust measured experimentally compared to the thrust predicted theoretically using both nozzle-1 and nozzle-2. The results obtained for nozzle-1 are given in Table 7.6 while Table 7.7 gives the results for nozzle-2.

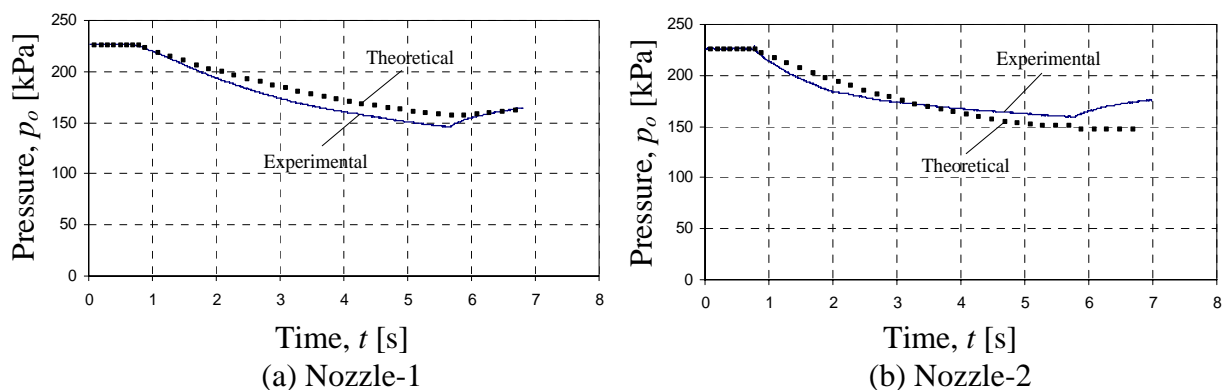


Figure 7.13 Comparison between experimental and theoretical pressure results
(backpressure = 20 Pa)

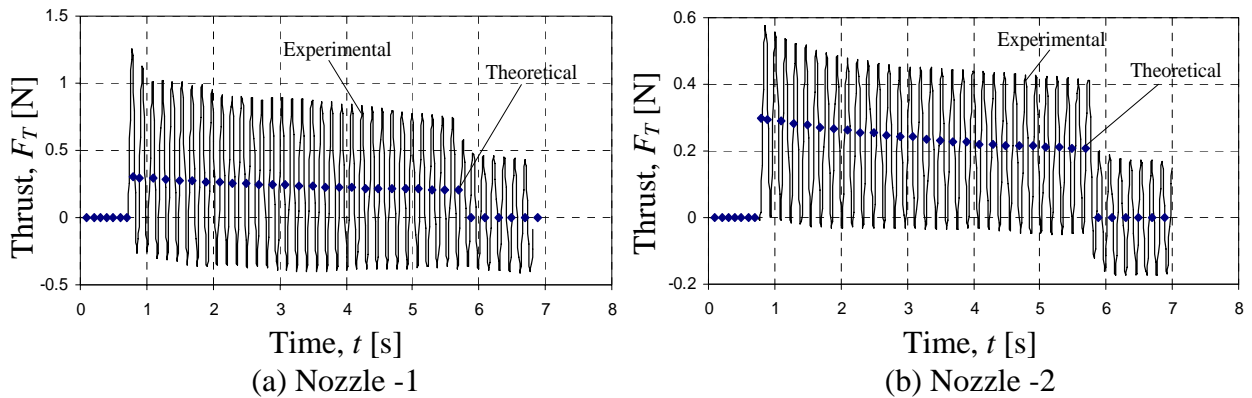


Figure 7.14 Comparison between experimental and theoretical thrust achieved
(backpressure = 20 Pa)

Figure 7.13 shows a good correlation between the experimentally measured pressure curves and the theoretically predicted pressure curves. The pressure increase in the accumulator due to the evaporating liquid is not influenced by the backpressure, to which the butane is exited. The reason why the pressure in the accumulator is not influenced by the backpressure is because the flow at the throat of the nozzles is choked.

The theoretically predicted thrust is in the same order as that measured experimentally. The thrusts predicted by the analytical model and measured experimentally are given in Table 7.6. It shows the results obtained under atmospheric conditions as well as the vacuum conditions. It also shows the results for both nozzle-1 and nozzle-2.

Table 7.6 Comparison between theoretical and experimental thrust for nozzle-1

	Start-up Pressure (kPa)	Start-up Temperature (°C)	Peak Thrust (mN)	$\int_{0.8}^{5.8} F_T dt [Ns]$
Theoretical – Atmospheric	224.4	22.3	4.09	0.013
Experimental – Atmospheric	224.4	22.3	39.23	0.14
Theoretical – Vacuum	225.3	22.3	300.00	1.16
Experimental – Vacuum	225.3	22.3	495.00	1.39

Table 7.7 Comparison between theoretical and experimental thrust for nozzle-2

	Start-up Pressure (kPa)	Start-up Temperature (°C)	Peak Thrust (mN)	$\int_{0.8}^{5.8} F_T dt [\text{Ns}]$
Theoretical – Atmospheric	226.2	22.7	81.60	0.201
Experimental – Atmospheric	226.2	22.7	75.75	0.26
Theoretical – Vacuum	226.1	22.7	282.00	1.01
Experimental – Vacuum	226.1	22.7	288.00	1.08

From Table 7.6 it can be seen that the theoretical and experimental results do not correlate very well for the atmospheric conditions. However, under vacuum conditions the total thrust predicted over the 5 second thrust period is out by less than 20 %. Therefore, for the case where shockwaves do not form inside of nozzle-1, the analytical model is able to predict the thrust of the system very accurately.

From Table 7.7 it can be seen that the correlation between the theoretical and experimental results under atmospheric conditions, using nozzle-2, is a lot better than was the case when using nozzle-1. For the atmospheric conditions the total thrust predicted was out by less than 30 %. The error in the prediction of the total thrust under the vacuum conditions is less than 7 %. This shows that the simple model used to simulate the thruster system is able to predict the thrust accurately, provided that there are not shockwaves inside of the nozzle as soon as the nozzle valve is opened.

7.2.3 Placing of copper mesh in accumulator

The simple model of the thruster system with the copper mesh inside of the accumulator is discussed in more detail in section 6.3.3. In this section the results obtained from the theoretical model will be given and compared with the experimental results for different number-of-mesh discs in the accumulator. The nozzle valve is opened for a 5 second burst before it is closed again. After the valve is closed the pressure recovery of the butane in the accumulator is observed.

In section 6.3.3 a heat transfer correlation coefficient is incorporated into the model to take into account the uncertainty of the heat transfer area as well as the heat transfer coefficient. The results for different values of the heat transfer correlation coefficient b (see equation 6.62) are shown in Figure 7.15. Each one of the figures is for a different number of mesh discs in the accumulator.

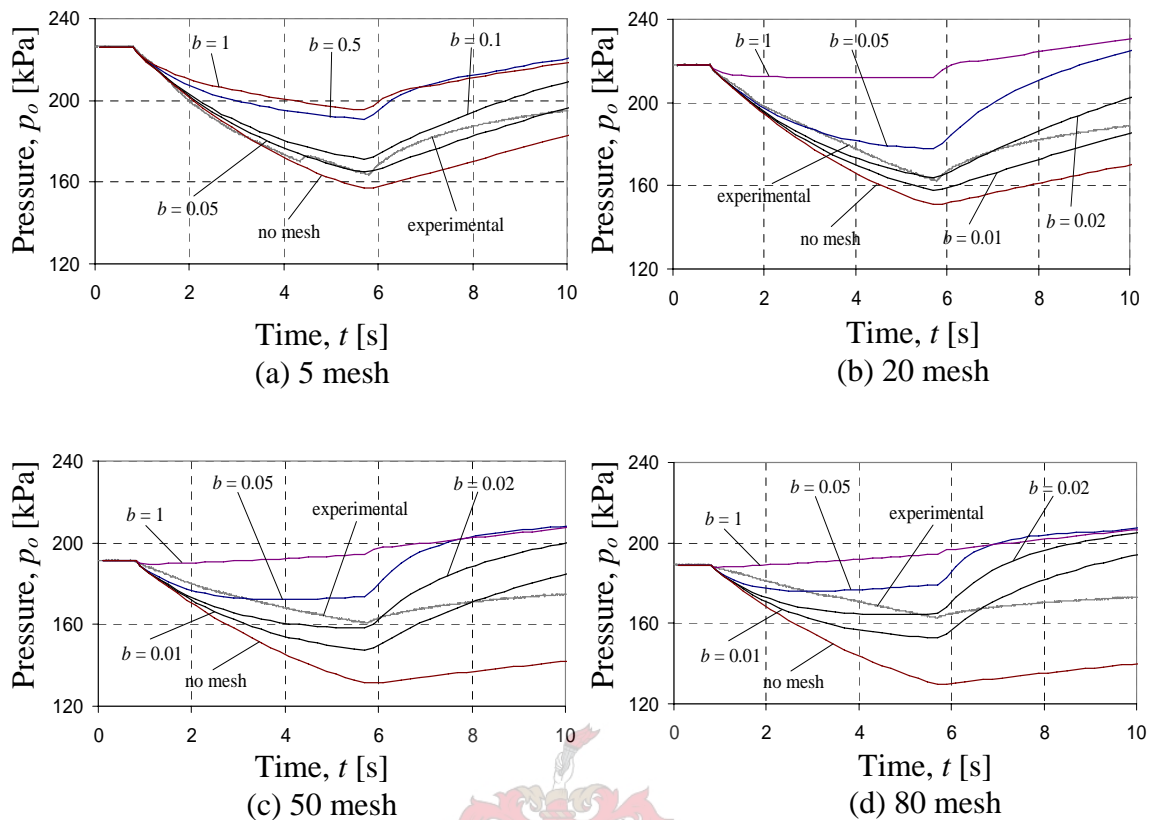


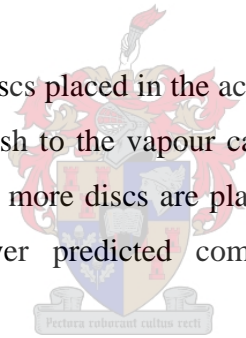
Figure 7.15 Theoretical pressure against time for different heat transfer correlation coefficients, b for different number of mesh discs

From Figure 7.15(a) it can be seen that the most accurate comparison between the experimental and theoretical results are obtained when $b = 0.05$. Figures 7.15(b), (c) and (d) show that the best comparison is achieved with $b = 0.02$. In Figure 7.15(a), with 5 mesh discs in the accumulator, the theoretical results still follow the experimental results quite well. Even the pressure recovery, after the valve is closed is simulated quite accurately. The more mesh is placed in the accumulator, the more difficult it becomes to model the pressure recovery accurately. For the 20, 50 and 80 mesh discs in the accumulator the pressure curve still follows the experimental curve well with the nozzle valve open, but once the nozzle valve is closed the pressure recovery is over predicted.

In the modelling of the system a single vapour control volume for the butane is assumed. With the addition of the mesh to the accumulator an extra heat source is now added to this control volume. When the nozzle valve is closed, heat is transferred from the mesh to the vapour. In the experimental set-up only a portion of the vapour

is in contact with the mesh, and because the nozzle valve is closed there will be very little movement of the fluid inside of the accumulator. Therefore, that portion of the vapour that is in contact with the mesh will heat up relatively quickly, while the rest of the vapour will remain at a lower temperature; and as the temperature of the vapour in contact with the mesh increases, the heat transfer from the mesh to that portion of the vapour will decrease. However, in the modelling of the system the butane vapour was modelled as a single control volume and therefore the temperature of the entire control volume would be equal. Because of this assumption the temperature of the vapour would remain lower, as the mesh now has to heat the entire vapour control volume and not just the vapour in contact with the mesh. Therefore the temperature difference between the vapour and the mesh would remain larger for a longer period of time than is actually the case. Therefore the heat transfer from the mesh to the vapour is higher than in actual fact and that is why the theoretical pressure recovery over predicts the pressure in comparison to the experimental pressure recovery.

The more the number of mesh discs placed in the accumulator, the more the influence of the heat transfer from the mesh to the vapour can be observed. This can be seen from Figure 7.15. Therefore, the more discs are placed in the accumulator, the more the theoretical pressure is over predicted compared with the experimentally determined pressure recovery.



7.2.4 Liquid surface area

In the modelling of the thruster system a liquid-vapour contact area is needed. In the model this area was used to calculate the mass of liquid that evaporated as well as the heat transfer between the accumulator wall and the butane liquid. Because this area could not be determined experimentally, different areas were estimated. The nozzle valve was opened for a 5 second period and then closed again and there were no mesh discs placed in the accumulator. Figure 7.16 shows the pressure of the butane vapour inside of the accumulator for different liquid-vapour contact areas. The largest area chosen was 0.000484 m^2 while the smallest area was 0.0001 m^2 .

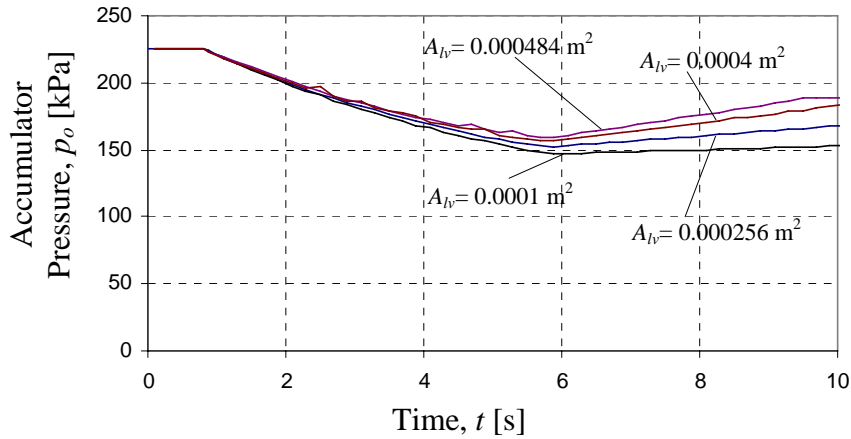


Figure 7.16 Pressure against time for different liquid-vapour contact areas

If the area was increased to a value above 0.000484 m^2 , the heat transfer was increased so much that all the liquid butane evaporated within the first time step. From Figure 7.16 it can also be seen that with the area equal to 0.0001 m^2 the rate at which the pressure recovery takes place after the nozzle valve is closed is almost insignificant. With the area, A_{lv} , equal to 0.0004 m^2 the best correlation between the theoretical and experimental results were obtained and therefore this was the area used for A_{lv} in equation 6.49 section 6.3.

7.2.5 Estimation of I_{sp} with mesh in accumulator

Under atmospheric conditions with no mesh in the accumulator the I_{sp} achieved with nozzle-1 was 4.95 s. Under vacuum conditions, also with no mesh in the accumulator, the I_{sp} achieved with nozzle-1 was 67.5 s. If the same increase that was achieved under atmospheric conditions with the addition of mesh in the accumulator is assumed under vacuum conditions, the I_{sp} of the system with mesh in the accumulator can be estimated. This assumption is valid only if the flow through the throat of the nozzle is choked, which was the case in the tests that were conducted. If the flow through the throat of the nozzle is choked, then the pressure in the accumulator is not influenced by the backpressure to which the nozzle exhausts. Table 7.8 shows the estimated I_{sp} values for the system with mesh in the accumulator under vacuum conditions using nozzle-1. The I_{sp} – Atmospheric values in Table 7.8 are the I_{sp} values from Table 7.4.

Table 7.8 Estimated I_{sp} values under vacuum conditions using nozzle-1

Mesh discs	I_{sp} - Atmospheric	I_{sp} - Vacuum
0	5	67.5 - Experimental
5	6.8	91.8 - Estimated
20	7.6	102.6 - Estimated
80	8.2	110.7 - Estimated

Using the estimated values for the I_{sp} in vacuum a linear regression analysis can be used to give the I_{sp} of the system as a function of the number of mesh discs in the accumulator. The assumed form of the equation is given as:

$$I_{sp} = I_{sp_o} + KN_d^n \quad (7.2)$$

where I_{sp_o} is for the base case with no mesh in the accumulator under vacuum conditions, and K and n are determined using the data set given in Table 7.8. Table 7.9 shows the experimental values for the I_{sp} compared to the theoretically calculated values (using equation 7.2) with $I_{sp_o} = 67.5$ s, $K = 18$ and $n = 0.20$. Figure 7.17 shows the comparison between the experimental and theoretical I_{sp} against the number of mesh discs in the accumulator under vacuum conditions.

Table 7.9 Experimental and theoretical values for I_{sp} under vacuum conditions with different number of mesh discs in accumulator

Mesh discs	I_{sp} - Experimental	I_{sp} - Theoretical	% - Difference
5	91.8	92.34	0.59
20	102.6	100.27	2.32
80	110.7	110.74	0.036

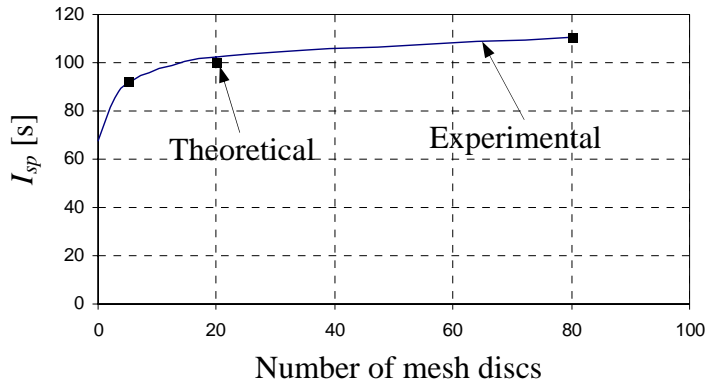


Figure 7.17 Comparison between experimental and theoretical I_{sp} under vacuum conditions with different number of mesh discs in the accumulator

8 Discussion and Conclusion

In the following section the theoretical model and experimental test results are discussed. Following the discussion conclusions are also drawn.

8.1 Validity of Experimental Results

The pressure in the accumulator was measured using two separate pressure transducers. One pressure transducer was situated at the inlet side of the accumulator, with the other one closer to the exit (nozzle end). An example of the measured pressures is shown in Figure 7.3 where the pressure curves coincide. The modelled pressure curves in the accumulator also matched the experimentally measured pressure curves very closely. This was the case for both nozzle-1 and nozzle-2 in both atmospheric and vacuum conditions. Examples of this are shown in Figure 7.9 and Figure 7.11 where it can again be seen that the two pressures coincide with each other.

There was some concern with the validity of the thrust measurements, as the thrust measured using nozzle-1 under atmospheric conditions did not match the results obtained from the theoretical model of the system. In order to prove that the thrust measurements were valid the thrust sensor was recalibrated and the original calibration curve was shown to be accurate. Also, the thrust that was measured using nozzle-2 under both atmospheric and vacuum conditions agreed well with the theoretical model of the system. The thrust measured using nozzle-1 under vacuum conditions also agreed well with the theoretical model. So, it was demonstrated that the thrust measurements were valid, and that the discrepancy between the theoretical and experimental results using nozzle-1 under atmospheric conditions had to be due to some other reason. This discrepancy will be discussed in more detail in the next section (section 8.2).

The two pressure transducers measured the same pressure and agreed well with the analytical model. Not only was the thrust sensor recalibrated, but the results obtained also agreed well with the analytical model using nozzle-2 under both atmospheric and vacuum conditions as well as using nozzle-1 under vacuum conditions. Therefore, it

can be concluded that all the experimental results are valid and can be used with confidence.

8.2 Validity of Theoretical Model

In order to validate the theoretical model the theoretical results were compared to the experimental results. In the first tests done under atmospheric conditions with nozzle-1 the thrust calculated by the theoretical model did not compare well with the experimental thrust achieved. However, in the modelling of the flow through nozzle-2 the thrust did compare well with the experimental thrust under atmospheric conditions. The difference between nozzle-1 and nozzle-2 under atmospheric conditions is that in the case of nozzle-1 shockwaves form inside of the divergent part of the nozzle as soon as the nozzle valve is opened. However, in nozzle-2 the shockwave only starts to move inside of the divergent part of the nozzle after the pressure in the accumulator drops low enough. Under vacuum conditions the theoretical thrust compared well with the experimental thrust for both of the nozzles.

In the simple theoretical model used it was assumed that if a shockwave formed inside of the divergent part of the nozzle, that it was plane normal. This assumption, of a plane normal shock in a nozzle, is assumed in most of the literature available on flow through a nozzle. However, all of the literature also assumes a constant pressure source, which was clearly not the situation here. In none of the literature found is a system considered with a variable pressure source. This is because this is a much more difficult problem because it entails an iteration process (as explained in section 6.1 and 6.2) to calculate the position of the normal shock in the nozzle. According to Hill et al. (1992) this assumption of a shockwave in a nozzle being plane normal with high exit plane pressure is definitely not valid. From the results (section 7.2) it can be seen that the assumption made of a shockwave being plane normal in a nozzle is not valid in this project. The shock *separates* the boundary layer and sets up a complex flow disturbance within the nozzle (Hill et al. (1992)) that will not be able to be simulated with the simple model that was used. Therefore a more advanced complex model would have to be used to determine the actual shock configuration of the flow in the nozzle and this was beyond the scope of this project.

The two-phase model of the liquid-vapour butane was able to accurately capture the behaviour of the flow and heat transfer in the accumulator. The two-phase model was able to predict the pressure in the accumulator very accurately in comparison to the pressure measured experimentally. The behaviour of the butane with mesh discs in the accumulator was also simulated with reasonable success. This model has however certain limitations. One of the assumptions made was to model the vapour as a single control volume. With the mesh in the accumulator this single control volume for the vapour proved to over predict the pressure recovery in the accumulator after the nozzle valve was closed. In order to be able to model the pressure recovery in the accumulator more accurately a more complicated model is required, which was again not in the scope of this thesis. A more complicated model could be to model the vapour as three control volumes: two vapour control volumes on either side of the mesh, and one control volume for the vapour in contact with the mesh.

From this discussion it can be concluded that the thrust predicted by the theoretical model is valid if there are no shockwaves present in the nozzle as soon as the nozzle valve is opened. Also, the two-phase model of the butane in the accumulator is able to accurately predict the pressure of the butane vapour in the accumulator, provided that there is no mesh in the accumulator. With mesh in the accumulator the model adopted in this thesis is still able to predict the pressure in the accumulator with reasonable success.

8.3 Mesh Inside Accumulator

The results obtained from the experimental testing of the system show that the performance of the thruster system can be greatly improved with the addition of copper wire mesh in the accumulator. From Table 7.1 to Table 7.4 can be seen that the average total thrust achieved by the thruster system with no additional mesh in the accumulator, was 0.365 Ns. With 5 discs of copper mesh in the accumulator an increase of 13 % in the total thrust compared with no mesh in the accumulator was achieved. With 20 discs of copper mesh an increase of 54 % in the total thrust was achieved. With 50 discs of copper mesh an increase of 39 % in the total thrust was achieved. With 80 discs of copper mesh the increase was 48 %. It must be remembered that the start-up pressures for all the different quantities of mesh in the

accumulator was not always the same. With a higher start up pressure and 80 mesh discs in the accumulator the increase in the total thrust was 54 %. This was the same as the increase when 20 mesh discs were used, although the start up pressure in the case where the 20 mesh discs were used was slightly higher. Figure 8.1 shows the total thrust against the number of mesh discs in the accumulator. From the figure it can be seen that the thrust seems to flatten out after 20 mesh discs are placed in the accumulator as the thrust achieved with the 80 mesh discs is equal to the thrust achieved with the 20 mesh discs.

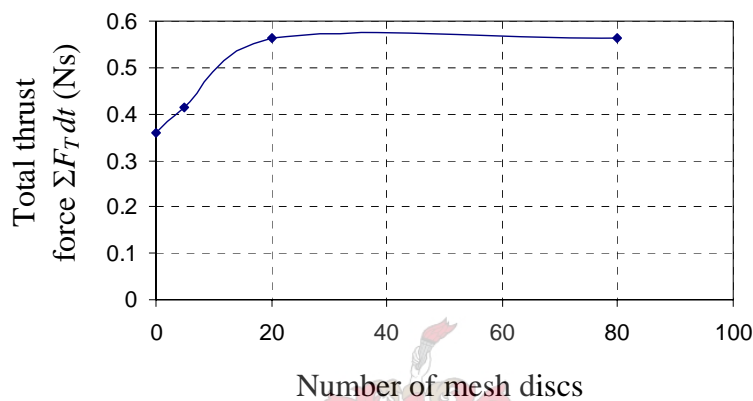


Figure 8.1 Total thrust achieved against number of mesh discs for more-or-less the same initial conditions for nozzle-1 under atmospheric conditions

From the experimental results it can also be seen that there was not a visible pressure drop across the mesh in the accumulator. This can be seen in Figure 7.1 where the pressure curves from the pressure transducers situated on either side of the mesh in the accumulator coincide. The reason for the increase in the thrust achieved with the addition of the mesh to the accumulator is because of the increase in the heat transfer. The more mesh discs the better, however whether or not there is an optimum number of discs was not established in this project.

8.4 Nozzle Size

The size (throat and exit diameter) of the nozzle has a significant influence on the performance of the thruster. Table 7.5 shows the influence that the size of the nozzle has on the total thrust that was achieved over the 5 second bursts. It is important to note that nozzle-2, with the smaller exit diameter, performed significantly better under atmospheric conditions than nozzle-1, under the same conditions. However, under

vacuum conditions, nozzle-1 performed better. This shows that the nozzle must be designed in accordance with the conditions under which it will be used. This includes the supply pressure to the nozzle as well as the backpressure, to which it is exhausted.

Using a smaller nozzle might increase the efficiency of the thruster but might not deliver enough thrust. In this project the thrust sensor was able to measure thrusts as small as 10 mN. The sensitivity of the thrust sensor was a limiting factor in the thrust that needed to be delivered, therefore the throat diameter used was much larger than the nozzle throat diameter that will be used in an actual space application.

The two nozzles that were tested both had the same throat diameter. This meant that the mass flow through the two nozzles would be the same, provided that the flow is choked at the throat of the nozzles. This was the case for both of the nozzles for all the tests that were done. Under atmospheric conditions shockwaves were present in the flow through both of the nozzles. In nozzle-2 a shockwave formed outside of the nozzle initially, and as the pressure in the accumulator decreased the position of the shockwave moved into the divergent part of the nozzle. In nozzle-1 a shockwave was present in the divergent part of the nozzle from the start of the test. Because of the presence of the shockwave in nozzle-1 from the start of the test its performance was significantly worse than that of nozzle-2. The presence of shockwaves in the nozzle decreases the performance of the nozzles significantly. This is clearly seen in Table 7.5 where the thrust achieved under vacuum conditions are compared to the thrust achieved under atmospheric conditions. In the vacuum chamber there were no shockwaves present in either of the two nozzles.

The highest total thrust achieved over a 5 second burst under atmospheric conditions was 0.26 Ns (see Table 7.5) using nozzle-2 while under vacuum conditions the highest total thrust achieved over a 5 second burst was 1.39 Ns using nozzle-1. Therefore we can conclude that nozzle-1 is more suited for space applications where the backpressure is equal to zero, while nozzle-2 is more suited for atmospheric conditions where shockwaves start to play a roll in the performance of the nozzle.

8.5 Overall Performance of Thruster System

The specific impulse I_{sp} is the unit that is generally used to measure the efficiency with which a satellite thruster system is able to convert the propellant mass into work (Sidi, 1997). The I_{sp} of the thruster is calculated using equation 3.2. The higher the specific impulse, the less propellant mass is consumed to obtain the same thrust. It is useful to compare the I_{sp} of the system with other existing systems, such as those developed at Surrey Space Centre.

Under atmospheric conditions with no mesh in the accumulator the I_{sp} achieved with nozzle-1 was 6 s. Under vacuum conditions, also with no mesh in the accumulator, the I_{sp} achieved with nozzle-1 was 67.5 s. Under atmospheric conditions with 20 mesh discs in the accumulator the I_{sp} achieved with nozzle-1 was 9.43 s. Using equation 7.1 an increase in the thrust under vacuum conditions with mesh in the accumulator is estimated. Table 7.8 shows that the estimated I_{sp} , using equation 7.1, for the system with 20 mesh discs in the accumulator under vacuum condition is 102 s.

The I_{sp} that was achieved by the SNAP-1 system developed by Surrey Space Centre was 43 seconds. The novel resistojet thrusters discussed by Sweeting et al. (1999) had a typical I_{sp} value of between 150 and 200 seconds. Instead of using butane as the propellant, water was used in these resistojet thrusters, so it may be difficult to compare the performance to our system where butane was used. The low power resistojet discussed by Baker et al. (2005) has a typical I_{sp} value of about 100 seconds when using butane as propellant. The estimated I_{sp} of our system of 102 s compares well with the I_{sp} value of the low power resistojet system (Baker, 2005) of 100 s.

9 Recommendations

In this section recommendations are made for future work that should be done if the use of liquefied gas micro satellite thruster systems are to be developed.

9.1 Resistojet

From the literature survey it seems evident that the research and development of liquefied gas systems as secondary propulsion systems are moving away from the accumulator concept to the resistojet concept. In the case of the accumulator the liquid butane is fed into the accumulator via a feed valve from the storage tank, heated and then exhausted via another exhaust valve. In the case of the resistojet the liquid butane is also fed into the resistojet from the storage tank via a feed valve. However, there is not another exhaust valve before the vapour is exhausted through the nozzle and therefore the liquid butane needs to be fed into the resistojet under a high pressure from the storage tank. In order to lay a sound foundation for further research in this type of thruster system it is recommended that a resistojet type thruster should be tested and modelled at the University of Stellenbosch.

9.2 Use of Mesh in Accumulator

It is recommended that finer mesh should be tested in the accumulator, as there was no pressure drop observed across the mesh in the accumulator. Using a finer mesh would increase the I_{sp} of the accumulator type thruster system to well above the I_{sp} of the resistojet. Although there were no pressure drop across the mesh in the tests done the increase in the thrust with an increase of the mesh above 20 discs were not significant. In this case an optimum solution might be to fill the whole accumulator with mesh, as there were no pressure drop observed across the mesh. It is suggested that the optimum amount of mesh discs will be in the order of 100 mesh discs for this case.

9.3 Dynamic Testing

Although the thrust of the system can be measured while the system is static, and therefore the performance of the system can be determined, other aspects of the system need to be tested dynamically. Sloshing plays a big role in the dynamic

movement of liquefied gas thrusters. This phenomenon can only be tested with dynamic tests. At the University of Stellenbosch there is a frictionless table available that can be used for the dynamic testing of such a system. For dynamic testing it is recommended that a much lighter thruster system be designed, compared with the one used in this thesis.

There are other aspects, other than sloshing, that also need to be looked at when doing dynamic tests. One of these is the frictional drag that needs to be overcome. The tests conducted on the frictionless table are not done under vacuum or zero gravity conditions, as will be the case in space. Therefore, when designing a thruster system for testing on the frictionless table the frictional drag and atmospheric backpressure need to be taken into account. The nozzle used in these tests should be specially designed to simulate the same thrust characteristics in air that would be experienced by the nozzle used in space, otherwise the calibration of the control logic could be incorrect if used in actual space conditions.

9.4 Space Proven Components

The components used in this project were commercially available components. In order for a thruster system to be acceptable to be used in space, it needs to make use of space proven technology (Gibbon et al., 2002). For test purposes it is recommended to use space proven valves. Also, the storage tank that was used was a commercially available stainless steel tank. It is recommended to look at other options that can serve as a storage tank. For instance, it might be useful to look at a tank with a bladder inside the tank, or maybe open-cellular mesh, to prevent sloshing of the liquid in the tank. The reason why commercially available components were used was because space proven components are a lot more expensive. However, if a thruster system is to be developed that can be used in space, it needs to make use of these space proven components, otherwise it cannot be considered for space applications.

9.5 Development of Accumulator Type Thruster

The performance of the thruster system that was developed compares very well with the performance of some of the leading thruster systems developed globally. However, the performance of this accumulator type thruster system can still be

improved quite significantly. This can be done by increasing the temperature and pressure of the butane vapour to superheated conditions inside of the accumulator. It is therefore recommended that further work take cognizance of this potential improvement. Some of other aspects that should be looked at in the further development of such a thruster system is to improve the heat transfer to both the liquid and vapour in the accumulator. Also, the energy that is needed to heat up the system has to be controlled and quantified and the effect of thermal insulation on the heat-up time and heat loss during the heat-up phase prior to initiation of the thruster.



10 References

Anderson J D, 2004, *Modern Compressible Flow*, McGraw-hill, New York.

ASHRAE Handbook, 2001, *Fundamentals*, ASHRAE, Atlanta.

Baker A M, da Silva Curiel A, Schaffner J and Sweeting M, 2005, “You can get there from here”: Advanced low cost propulsion concepts for small satellites beyond LEO, *Acta Astronautica*, Vol. 57, pp 288-301.

Behkam B and Sitti M, 2004, E. Coli inspired propulsion for swimming microrobots, *Proceedings of IMECE International Mechanical Engineering Conference*, pp 13-19.

Benham P P, Crawford R J and Armstrong C G, 1996, *Mechanics of Engineering Materials*, Pearson Education Limited, Harlow, England.

Boctor S A, Ryff P F, Hiscocks P D, Ghorab M T, Holmes M R, 1997, *Electrical Concepts and Applications*, West, St. Paul.

Cengel Y A and Boles M A, 2002, *Thermodynamics: An Engineering Approach*, McGraw-hill, New York.

Gibbon D M, Baker A M, 2003, The design, development and in-flight performance of a low power resistojet thruster, *American Institute of Aeronautics and Astronautics*, 4548, pp 1-10.

Gibbon D M, Underwood C and Sweeting M, 2002, Cost effective propulsion system for small satellites using butane propellant, *Acta Astronautica*, Vol. 51, No 1-9, pp 145-152.

Hill P G and Peterson C R, 1992, *Mechanics and Thermodynamics of Propulsion*, Addison Wesley Publishing Company, USA.

Mills A F, 1999, *Heat Transfer*, Pretence Hall, Upper Saddle River, USA.

Potter M C and Scott E P, 2004, *Thermal Sciences*, Brooks/Cole – Thompson Learning, Belmont.

Rosenburg N, 2005, Design, manufacturing and testing of a liquified gas micro satellite propulsion system, *Final Year Bsc.Eng Project*, University of Stellenbosch.

Sidi M J, 1997, *Spacecraft Dynamics And Control: A Practical Engineering Approach*, Cambridge University Press, Cambridge.

Stephen J R, Rajanna K, Dhar V, Kumar K G K and Nagabushanam S, 2004, Thin-film strain gauge sensors for ion thrust measurement, *IEEE sensors journal*, Vol. 4, pp 373-377.

Sweeting M N, Lawrence T and Leduc J, 1999, Low-cost orbit manoeuvres for minisatellites using novel resistojet thrusters, Surrey Space Centre, University of Surrey, Guildford UK.

Weyer R B, Dobson R T and van der Westhuizen K, 2004, Development of a liquefied-gas micro-satellite propulsion system, Part I – Theoretical modelling, *R & D Journal*, Vol. 20, pp 8-13.

Weyer R B, Dobson R T and van der Westhuizen K, 2004, Development of a liquefied-gas micro-satellite propulsion system, Part II – Experimental evaluation, *R & D Journal*, Vol. 20, pp 14-20.

White F M, 1999, *Fluid Mechanics*, McGraw-hill, Singapore.

Xiong J, Zhou Z, Ye X, Wang X, Feng Y and Li Y, 2002, A colloid micro-thruster system, *Microelectronic Engineering*, Vol. 61–62, pp 1031–1037.

Ye X Y, Tang F, Ding H Q and Zhou Z Y, 2001, Study of a vaporizing water micro-thruster, *Sensors and Actuators*, Vol.89, pp 159-165.

Appendix A: Correlation for Saturation Properties of Butane

A two-phase model of the butane was developed to simulate the behaviour of the butane in the accumulator. Correlations for the saturation properties for both the vapour and liquid phase of the normal butane were required in the numerical modelling of the system. These correlations (simplified) for the butane were obtained using data from ASHRAE Handbook (2001). The following correlations were used:

Enthalpy of saturated vapour given temperature: $h_{g_sat@T}$

$$h_{g_sat@T} = a_0 + a_1T \quad (A.1)$$

T in K, $h_{g_sat@T}$ in kJ/kg, range: 173-393 K

Specific heat at constant pressure of saturated vapour given temperature: $C_{p_v_sat@T}$

$$C_{p_v_sat@T} = a_0 + a_1T + a_2T^2 + a_3T^3 + a_4T^4 + a_5T^5 + a_6T^6 \quad (A.2)$$

T in K, $C_{p_v_sat@T}$ in kJ/kg·K, range: 173-393 K

Saturated pressure given temperature: $p_{sat@T}$

$$p_{sat@T} = a_0 + a_1T + a_2T^2 + a_3T^3 \quad (A.3)$$

T in K, $p_{sat@T}$ in Pa, range: 287-299 K

Table A.1 Constants required for determining enthalpy in equation A.1

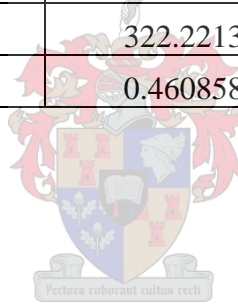
	$h_{g_sat@T}$ [kJ/kg]
a_0	212.22472
a_1	1.36767845

Table A.2 Constants required for determining specific heat in equation A.2

	$C_{p,v,sat@T}$ [kJ/kg·K]
a ₀	50.8875374
a ₁	-1.201312935
a ₂	0.019911076
a ₃	-6.215878596·10 ⁻⁵
a ₄	1.805204062·10 ⁻⁷
a ₅	-2.76595000·10 ⁻¹⁰
a ₆	1.74927500·10 ⁻¹³

Table A.3 Constants required for determining saturation pressure in equation A.3

	$P_{sat@T}$ [Pa]
a ₀	6238896.837
a ₁	76850.0045
a ₂	322.22132
a ₃	0.4608586



Appendix B: Validity of Thrust Modelling

One way of validating the results obtained from the analytical model was to compare the results to those in the literature. The only aspect that was compared in this way was the flow through the nozzle. The initial conditions given in the literature was then programmed into the model, and then the results were compared.

The first results that were compared were the results found in example 17.7 in Potter et al. (2004). A converging-diverging nozzle with a throat diameter of 5 cm and an exit diameter of 10cm is used. Air is used as the fluid, with the reservoir pressure maintained at 90 kPa absolute and the temperature at 20 °C. The receiver pressure needs to be determined in order for a normal shockwave to form across the exit plane of the nozzle. The mass flow through the nozzle also needs to be determined.

From the table below it can be seen that there is no difference between the results obtained from the analytical model and that in the literature.

Table B.1 Results from Example 17.7

	Analytical	Literature
Mass flow through nozzle [kg/s]	0.417	0.417
Pressure in front of normal shock [kPa]	2.68	2.68
Pressure just after of normal shock [kPa]	26.6	26.6

In Example 17.8 (Potter et al., 2004) the position of a normal shockwave needs to be determined. In the example the diameter where the shockwave occur is given. The exit pressure needs to be calculated in order to position a normal shockwave where the nozzle diameter is equal to 7.5 cm. Again the throat and exit diameters were given as 5 and 10 cm respectively.

The mathematical model was programmed such that it would calculate the diameter in the nozzle where a normal shockwave will occur, if the receiver pressure is given. However, in the example the diameter where the shockwave will occur in the nozzle is given, and the receiver pressure needs to be calculated. It was decided to specify the receiver pressure in the mathematical model, and then see whether the program is able

to calculate the diameter where the shockwave should occur correctly. The results obtained from the analytical model are compared to those given in the example in Table B.2.

Table B.2 Results from Example 17.8

	Analytical	Literature
Mach number before shockwave	2.33	2.33
Mach number after shockwave	0.531	0.531
Stagnation pressure after shockwave [kPa]	114	114
Exit Mach number	0.264	0.265
Exit Pressure [kPa]	109	109
Diameter where shockwave occurs [cm]	7.5	7.5

From the results given in Table B.1 it can be seen that the theoretical model of the flow through the nozzle is able to calculate the properties of the flow accurately, with a normal shockwave present at the exit plane of the nozzle. And from Table B.2 it can be seen that the theoretical model is able to predict the position of a normal shock inside of the divergent part of the nozzle.

These results show that the properties of a fluid at the exit of a nozzle can be determined using the theoretical model presented in section 6.1. These properties can be determined when a normal shockwave is present at the exit plane of the nozzle or even when the position of the shockwave inside of the divergent part of the nozzle needs to be calculated. With the flow properties of the fluid known at the exit of the nozzle the thrust can be calculated using equation 3.1.

Appendix C: Theoretical Thrust Calculation

When using a strain gauge bridge amplifier to measure the strain gauge it is necessary to set a calibration signal corresponding to a specified voltage change over the bridge. For the experimental measurements done for this project this calibration signal was always set to the maximum value of 10 V for a change of 1 mV/V over the bridge, the calibration equations were then used to convert the sampled voltages to engineering units in $\mu\text{m}/\text{m}$. The bridge amplifier used was a Hottinger Baldwin Messtechnik 5kHz TF-Messverstärker, type DIN 57411, serial number 92189. In this section the experimentally measured strain is compared to the theoretically calculated strain as shown in section 5.1.5.

Using the theory presented in section 5.1.5 it is shown that the strain can be calculated from equation 5.12. From equation 5.12 the expression for the ratio of output to input voltage in terms of the axial strain ε_x and the gauge factor K is

$$\frac{V_{out}}{V_{in}} = \frac{K}{2} \varepsilon_x \quad (\text{C.1})$$

For the bridge amplifier used the input V_{in} applied over the bridge is 1 V. Knowing the gauge factor, K , of the strain gauge the strain can be calculated from the voltage output given by the bridge amplifier using equation C.1. The specific gauge factor of the strain gauges used was 2.075.

The strain may also be calculated using equation 5.5. Assuming a thrust of F_T of 1 N is applied to the cantilever beam, the axial strain ε_x is calculated from equation 6.5:

$$\begin{aligned} \varepsilon_x &= -\frac{F(L-x)y}{I_{yy}E} = -\frac{(1)(0.2-0.027)(-0.001)}{(2.4 \times 10^{-11})(1.96 \times 10^{11})} \\ &= 3.667 \times 10^{-5} \quad [\text{m}/\text{m}] \\ &= 36.77 \quad [\mu\text{m}/\text{m}] \end{aligned} \quad (\text{C.2})$$

A force of 1 N was applied to the beam to measure V_{out} for the strain gauges. The table below shows the comparison between the values obtained experimentally by applying different forces to the beam and the analytical solutions.

Table C.1 Comparison between analytical and experimental strain

Force [N]	Voltage [V]	Strain – analytical [$\mu\text{m}/\text{m}$]	Strain – experimental [$\mu\text{m}/\text{m}$]
1	0.0765	36.77	39.68
0.5	0.038	18.39	19.71
0.1	0.00775	3.68	4.02

From the figure below it can be seen that there is a slight discrepancy between the theoretical strain and the measured strain. This can be due to a slight misalignment of the strain gauges – the gauges might not be perfectly aligned with the beam axis and might not be exactly opposite each other. Additional errors might be due to the accuracy and noise of the instrumentation. It can be seen however that the error is quite small. The final calibration was done experimentally, to take into account any errors.

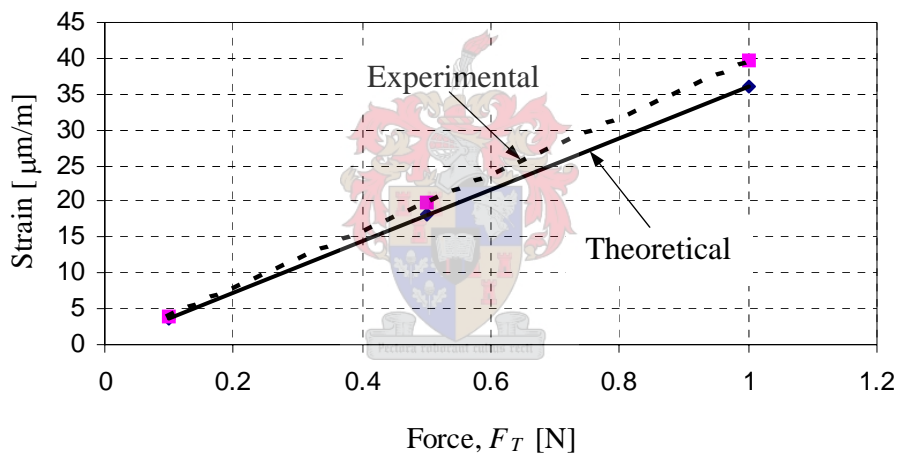


Figure C.1 Experimentally and theoretically determined strain as a function of force

Appendix D: Photographs of Experimental Set-up

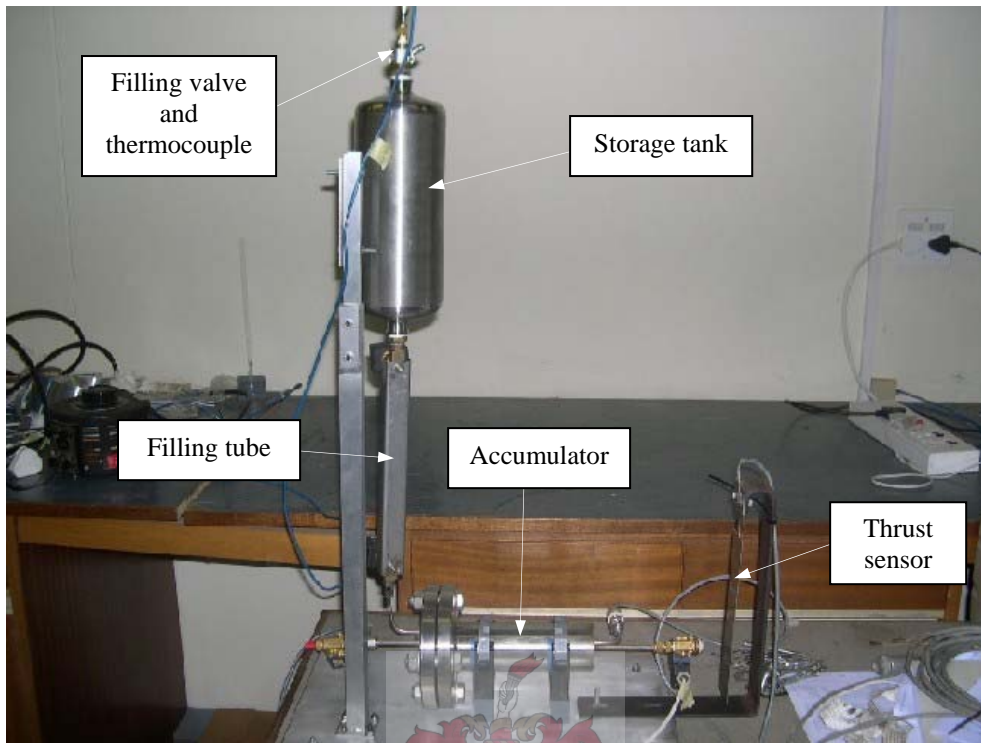


Figure D.1 Experimental set-up
(see also Figure 4.1)

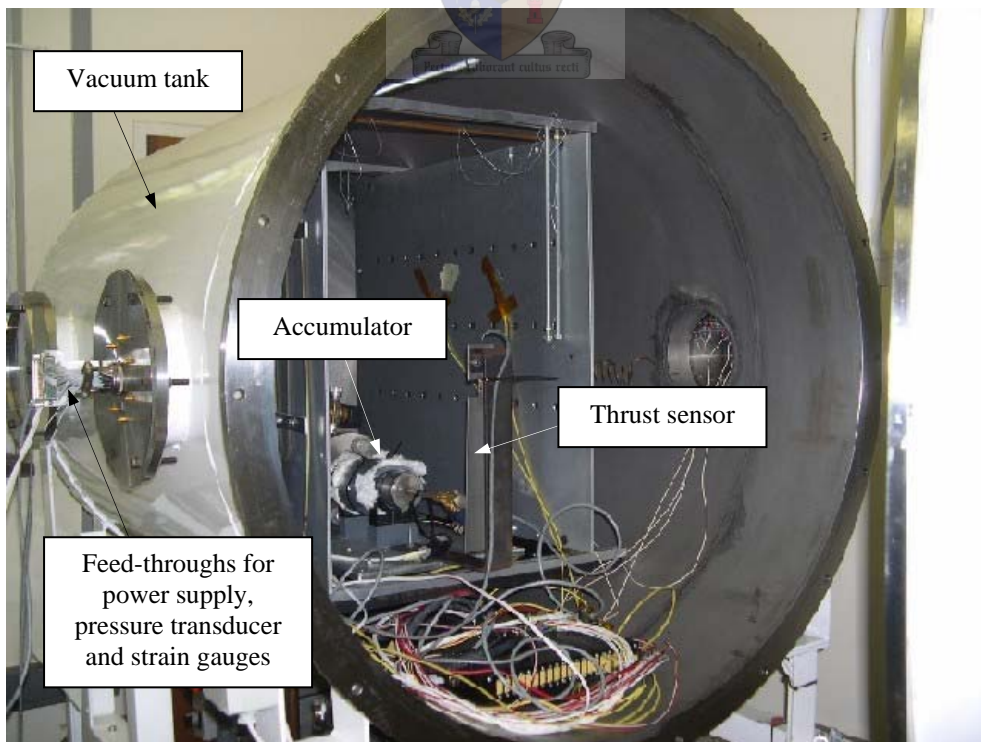


Figure D.2 Experimental set-up in vacuum chamber

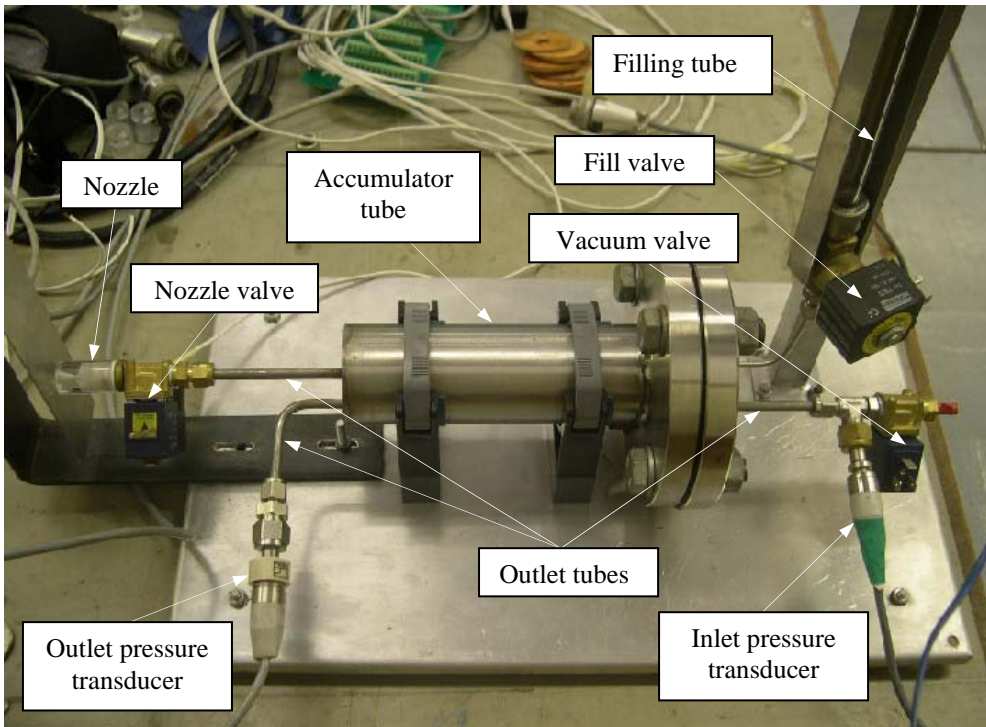


Figure D.3 Accumulator
(see also Figure 4.2)

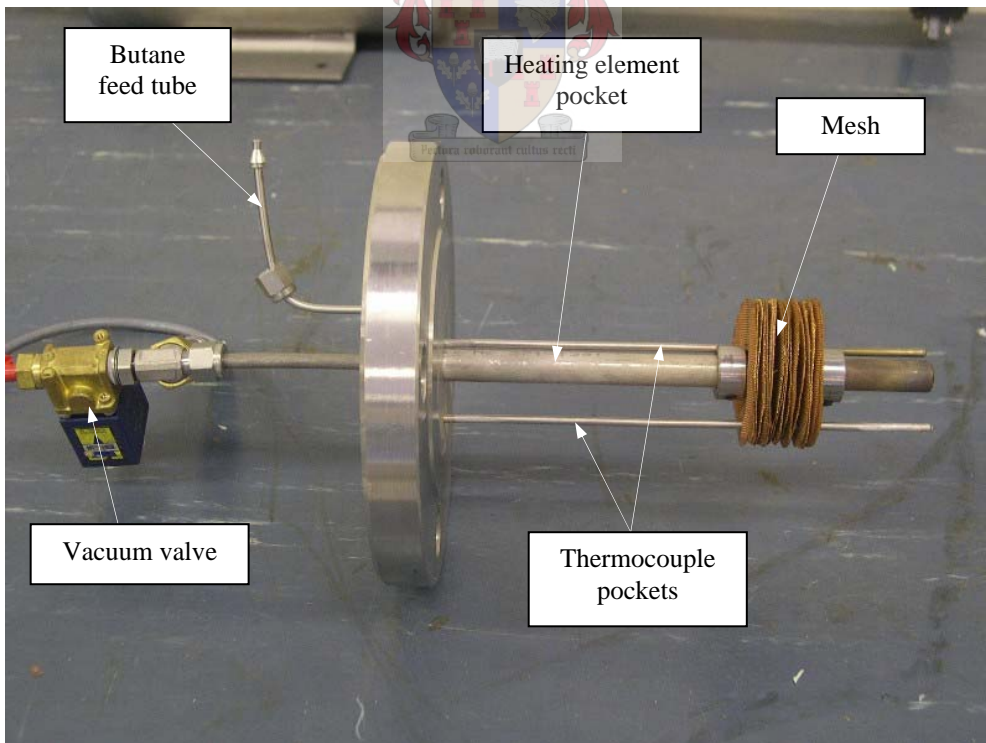


Figure D.4 Flange of accumulator